PEOPLE'S DEMOCRATIC REPUBLIC OF ALGERIA

Ministry of Higher Education and Scientific Research

University LARBI BEN M'HIDI Oum El Bouaghi-
Department of Mechanical Engineering

Thesis submitted in fulfillment of the requirements for the Degree of Doctorate

Submitted by

BENBOUAZIZ Oussama

Supervisor:

Prof. MAMERI Abdelbaki

Co-supervisor:

Dr. HADEF Amar

Entitled:

Numerical simulation of the turbulent combustion of low calorific value fuels applied to the combustion chambers of gas turbines

Committee members:

Prof. Bordja Lyes	University Oum El Bouaghi	President
Prof. Mameri Abdelbaki	University Oum El Bouaghi	Supervisor and rapporteur
Dr. Hadef Amar	University Oum El Bouaghi	Co-Supervisor
Prof. Aouachria Zeroual	University Batna 1	Examinator
Dr. Alliche Mounir	University Médéa	Examinator
Dr. Harnane Yamina	University Oum El Bouaghi	Examinator

Contents

List of figures

List of tables

Nomenclature

D_a: Damköhler Number [-]

D: Diameter [m]

D_{cf}: Diameter of Co flow

D_i : Inner Diameter

D_{jet}: Diamter of jet

D_o: Outer diameter

H: Distance between two jets

h_s: Total Enthalpy [J/kg]

k= Turbulent kinetic energy [m^2/s^2]

K_v: Recirculation rate [-]

l': length scale

L= Length of nozzle [m]

m_a: Mass flow rate of air oxidizer [kg/s]

m_e: Mass flow rate of recirculated flue gases [kg/s]

m_f: Mass flow rate of fuel [kg/s]

Q_{rad}: Radiative Heat Loss[kg/m^3s]

R: Radius [m]

Re: Reynolds Number [-]

s: stoichiometric ratio

T: Temperature [K]

t: Time [s]

u': velocity scale [m/s]

u_i'', u_j'': Favre velocity fluctuations [m/s]

x_i, x_j, x_k: Direction along axes i, j and k [m]

u_i, u_j: Mean velocity [m/s]

W_i: Molecular weight of species i [g/mol]

W: Mixture molecular weight [g/mol]

x_i: Mole fraction of species i [-]

y_i: Mass fraction of species i [-]

Z : Mixture Fraction [-]

Le: Lewis Number [-]

Greek letters

δ_{ij}: Kronecker delta

ε: Turbulent dissipation rate [m^2/s^3]

λ: Coefficient of thermal diffusivity [J/kg. k]

μ: Dynamic viscosity [kg/m s]

μ_t: Turbulent dynamic viscosity [kg/m s]

ρ: Density [kg/m^3]

ω_i: Reaction rate of species i [mol / m^3 s]

Acronyms

AJHC: Adelaide Jet Hot Coflow

CFD: Computational Fluid Dynamics

EBU: Eddy Break UP

EDC: Eddy Dissipation Concept model

EEC: Excess Enthalpy Combustion

HCCI: Homogeneous Charge Compression Ignition

HDDI: Hot Diluted Diffusion Ignition

HFFI: Homogeneous Flow Flowing Ignition

HiCOT: High-temperature air Combustion Technology

HiTAC: High-Temperature Air combustion

HPAC: Highly Preheated Air Combustion

JHC: Jet Hot Coflow

LES: Large Eddy Simulation

LHV: low heat value

MILD: Moderate intensive Low-Oxygen Dilution

PDF: Probability Density Function

RANS: Reynolds-Averaged Navier Stokes

RSM: Reynolds Stress Models

RZ: Recirculation Zone

SLFM: Steady Laminar Flamelet Model

TCF: Turbulence Counter-flow Flame

Acknowledgments

I would first like to express my sincere gratitude and appreciation to my supervisor ***Pr. Mameri Abdelbaki*** *for his continuous encouragement and guidance throughout this work, great support, and kind advice throughout my Ph.D. studies. It was a real privilege and an honor for me to share his exceptional scientific knowledge but also extraordinary human qualities. I also appreciate the freedom and trust that he has given me.*

I also would like to thank my co-supervisor ***Dr. Hadef Amar*** *for his constant support. Availability and constructive suggestions. Which were determinants for the accomplishment of the work presented in this thesis*

I would also like to thank my committee members, ***Pr. Bordja L., Pr. Aouachria Z., Dr. Alliche M.,*** *and* ***Dr. Harnane Y.*** *For accepting to evaluate my work and to be members of my committee even at hardship.*

I would like to thank my close colleagues and friend, ***Lounis Massouad****, for providing me with moral support and his workstation for our calculations from the beginning of my studies. I would also like to thank* ***Khelifi Roumaisa*** *for her support throughout these years.*

Last but not least. A special thanks to my family, I am truly thankful to my parents ***Benbouaziz Messouad*** *and* ***Gaziz Souad*** *for their tremendous encouragement during the period of this research work and for all of the sacrifices that you've made on my behalf. I am also grateful to my sister and brother* ***Roumaissa*** *and* ***Ayoub,*** *for their unconditional support, encouragement, and love, and without which I would not have come this far.*

Chapter I

Introduction

In the 19th century, and even more so in the 20th century, combustion had many industrial applications (transportation, heating, industrial production, electricity generation). However, it leads to a significant emission of various pollutants harmful to humans and nature, such as carbon monoxide, nitrogen oxides and carbon dioxide, which is a greenhouse gas. The increase in the world population has amplified these effects and led to an increase in fossil fuel consumption and a decrease in the global stock. Multiple regulations limiting pollutant emissions have been developed. Much scientific work has been carried out to improve the efficiency and quality of combustion processes.

The scientific community interest is focused on the identification of new technologies that would allow achieving more efficient energy production systems, in terms of pollutants reduction and energy production. One of the most popular technologies used to reduce emissions and improve combustion process is the Moderate Intensive Low-oxygen Dilution (MILD) combustion. The advantages of this technology are that the properties gradients across the flames are negligible and Nitric Oxide (NO) emissions are nearly zero. Indeed, this technology was already used in many industries. Another trend that attracted researchers is the use of biofuels to reduce emissions. The exploitation of these alternative sources contributes significantly in reducing harmful emissions and conserving fossil fuel stocks.

In our research, we studied MILD combustion of biofuels. For the latter, we used biogas-syngas (CH4/CO2/H2/CO) fuel, since it is a mixture of two alternative available fuels. It is well known that the combustion flame of biogas is unstable, because it contains a significant amount of carbon dioxide CO_2. To improve the stability of the flame, we add hydrogen-containing syngas that contributes to the stability of the flame and promotes the combustion of Low Calorific Value (LCV) fuels.

The objective of this study is to elucidate characteristics of the MILD turbulent combustion of biogas-syngas mixture in a JHC burner. Effects of the volume of methane in biogas, hydrogen in syngas, oxygen concentration, the temperature of oxidizer stream, and velocity of the fuel jet are all depicted.

State of art

During the last century, energy consumption has become very high with a great development that affected all fields. In the word, roughly 84% of the energy used comes from combustion sources [1]. The meaning of combustion in your daily life is seen by a simple glance around your local area. More than likely, the heat for your room or house comes directly from combustion (either a gas- or oil-fired furnace or boiler) or, indirectly, from electricity produced by the combustion of fossil fuel. It can be seen in Fig. 1.1 that the electricity produced from nuclear and renewable energy is estimated to be more than one-third (36.7%) of global electricity in the world. While the rest is produced by fossil fuels (63.3%). But they account for less than half that figure (15.7%) of the total energy, as the total energy includes all of the heating, transportation, and electricity. Both transportation and heating depend more on fossil fuels. Thus, the percentage is high in the case of the total energy than in electricity only. The latter is used to mislead regarding the reduction of emissions and the increasing use of nuclear energy and solar panels. But, all of this is only in the production of electricity, which is a component of the total energy. Renewable energy includes bioenergy, hydropower, wind, solar, geothermal, wave, and tidal which represent 11.4% and 4.3% came from nuclear (Fig. 1.1).

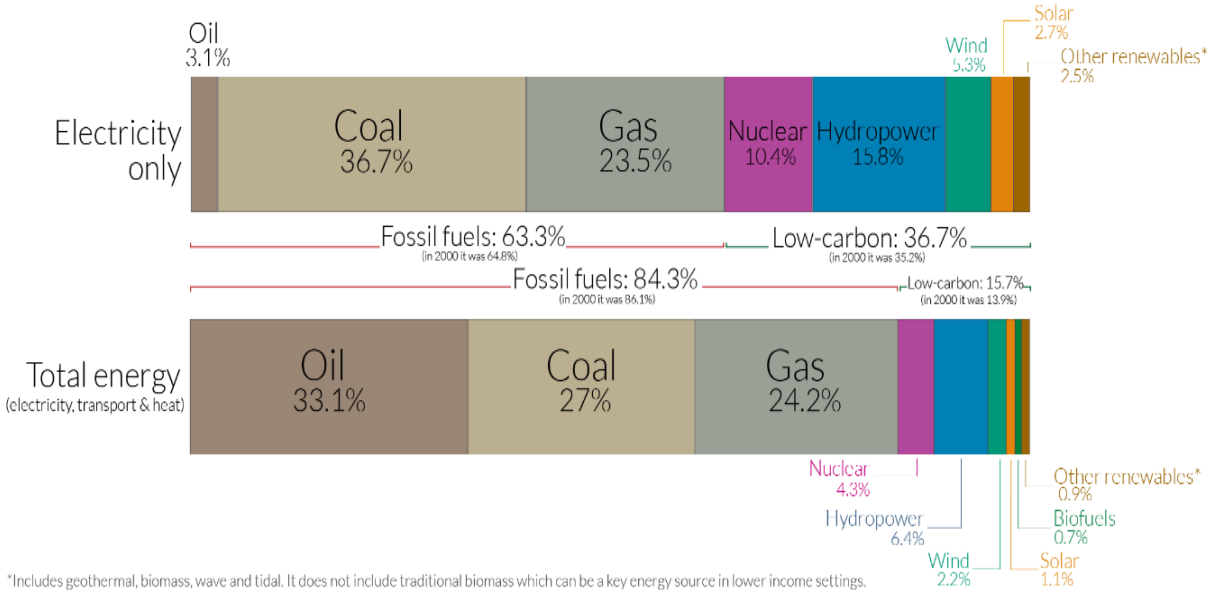

Figure 1. 1: The percentage of energy production from low-carbon sources in the world [2].

Despite the increase in the production of renewable energy, the consumption of fossil fuels remains dominant. During the past ten years, total energy production from fossil fuels increased from 116,214 to 136,761 TWh and consumption continues to increase in the future

(Fig. 1.2). It is also important to mention the reasons which have strongly favored the spread of fossil fuels. Fossil fuels are plentiful and present on nearly every continent on the planet, their abundance also allowed the containment of their costs, permitting competitive prices in the energy market. In the transport sector, in particular, fossil fuels give a much higher energy density than other technologies, such as electric vehicles.

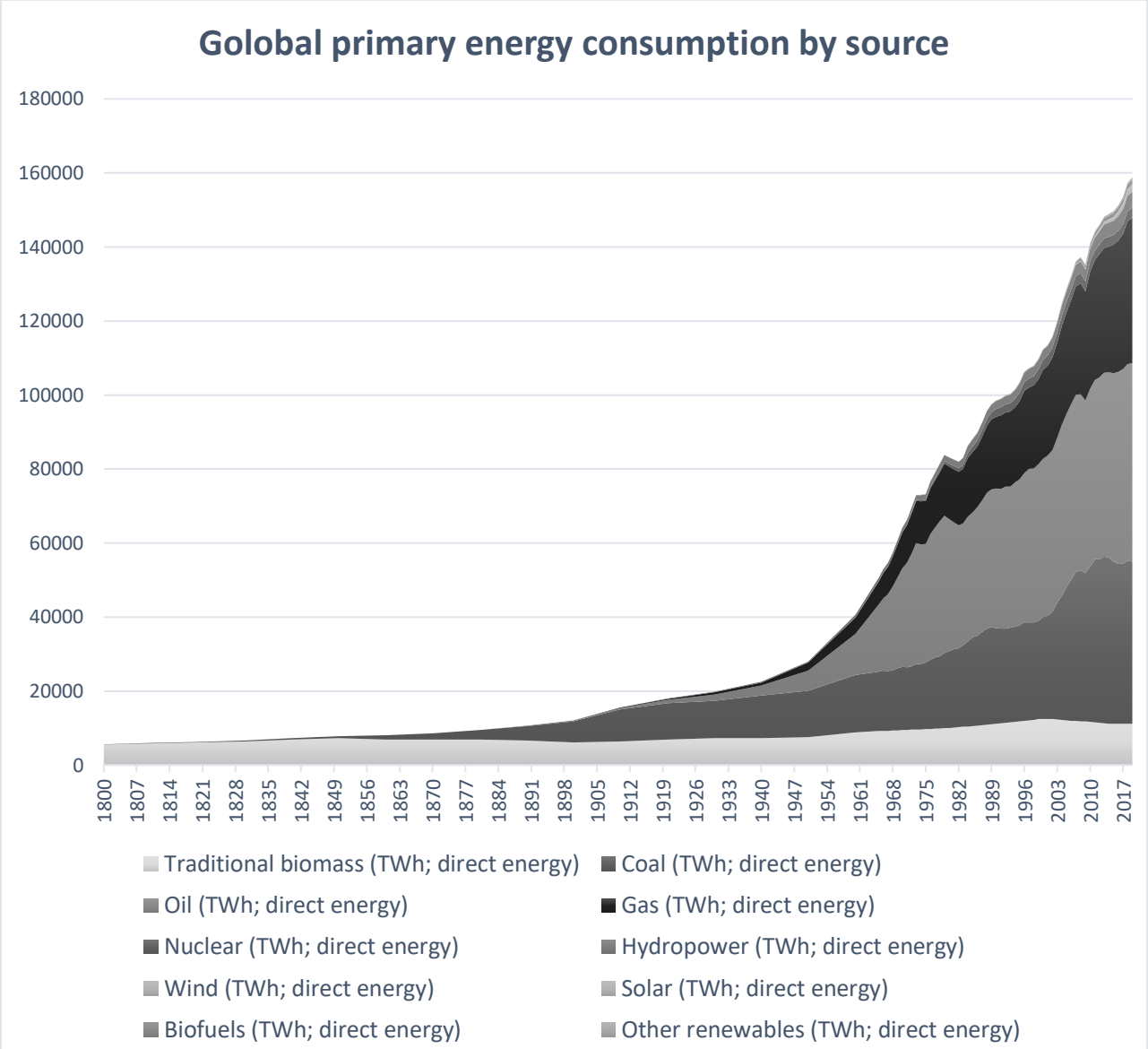

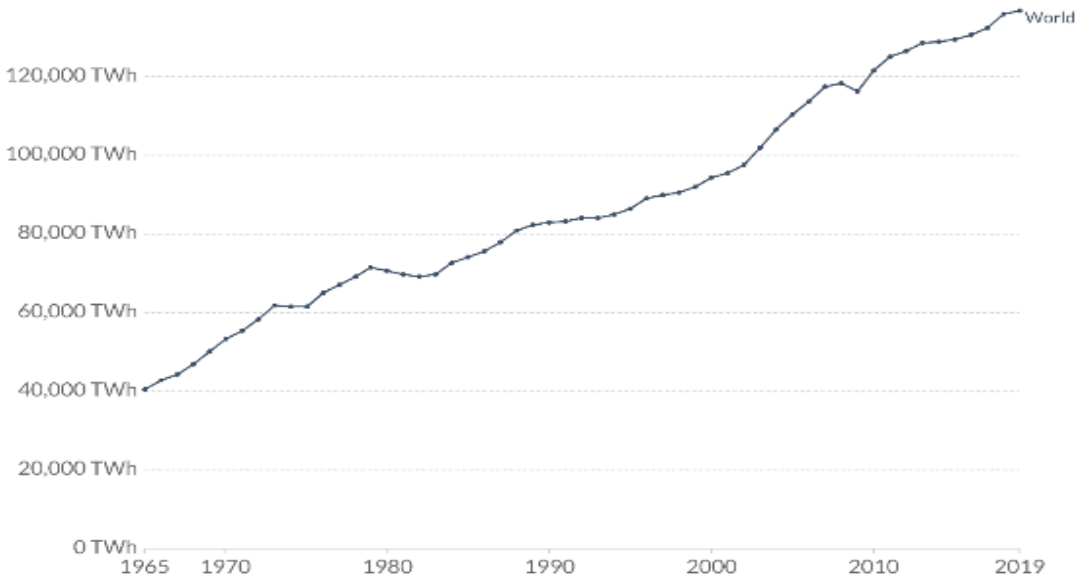

Figure 1. 2: top) Fossil fuel consumption by categories, bottom) Global fossil fuel consumption [3]

With population growth and technological progress, the energy demand is dramatically increasing, especially electric energy. The combustion process emits pollution species that are highly harmful to humans. Such as carbon monoxide (CO), which can produce severe poisoning, or nitrogen oxides (NOx), which include nitrous oxide (NO_2), a potent greenhouse gas, and nitrogen monoxide (NO), which is toxic at low doses (mucosal irritation) and can be associated with water to form nitric acid (HNO_3) responsible for acid rain. The CO_2 emissions distribution from the mid-eighteenth century up to this day is depicted in Fig. 1.3 (top). It can be seen that emissions were relatively low before the industrial revolution. Until the mid-twentieth century, emissions growth was relatively slow. In 1950, the world emitted more than 5 billion tons of carbon dioxide (CO_2). This had quadrupled to 22 billion tons by 1990. Emissions have continued to increase exponentially, with annual emissions now reaching 36 billion tons. Each year 629 billion tons of water are added to the world's oceans because of the melting of glaciers, which has contributed to an increase in the level of the oceans of about 1.5 millimeters per year, or 12 millimeters in 8 years. Finally, toxic organic micropollutants such as lead and heavy metals infiltrate the soil and disrupt the food chain of some animal species [2]. All of these emissions contribute to climate change. As shown in Fig. 1.3 (bottom), global temperatures have risen dramatically in recent decades, reaching around 0.7°C higher than our 1961-1990 baseline. On other hand, air pollution is responsible for 5 million deaths each year, approximately 9% of global deaths (Fig. 1.4). SO_2 sulfur dioxide is a factor in respiratory disorders through its deposits on the lung alveoli, volatile organic compounds (VOCs) irritate the respiratory tract and cause cancers. Carbon monoxide (CO) causes anoxia (blue disease or

oxygen deficiency), cardiovascular disorders, migraines, and dizziness. NOx nitrogen oxides easily penetrate bronchioles, affect respiration by inducing bronchial hyper-reactivity in asthmatics, and increase branch vulnerability to microbes at least in children[4].

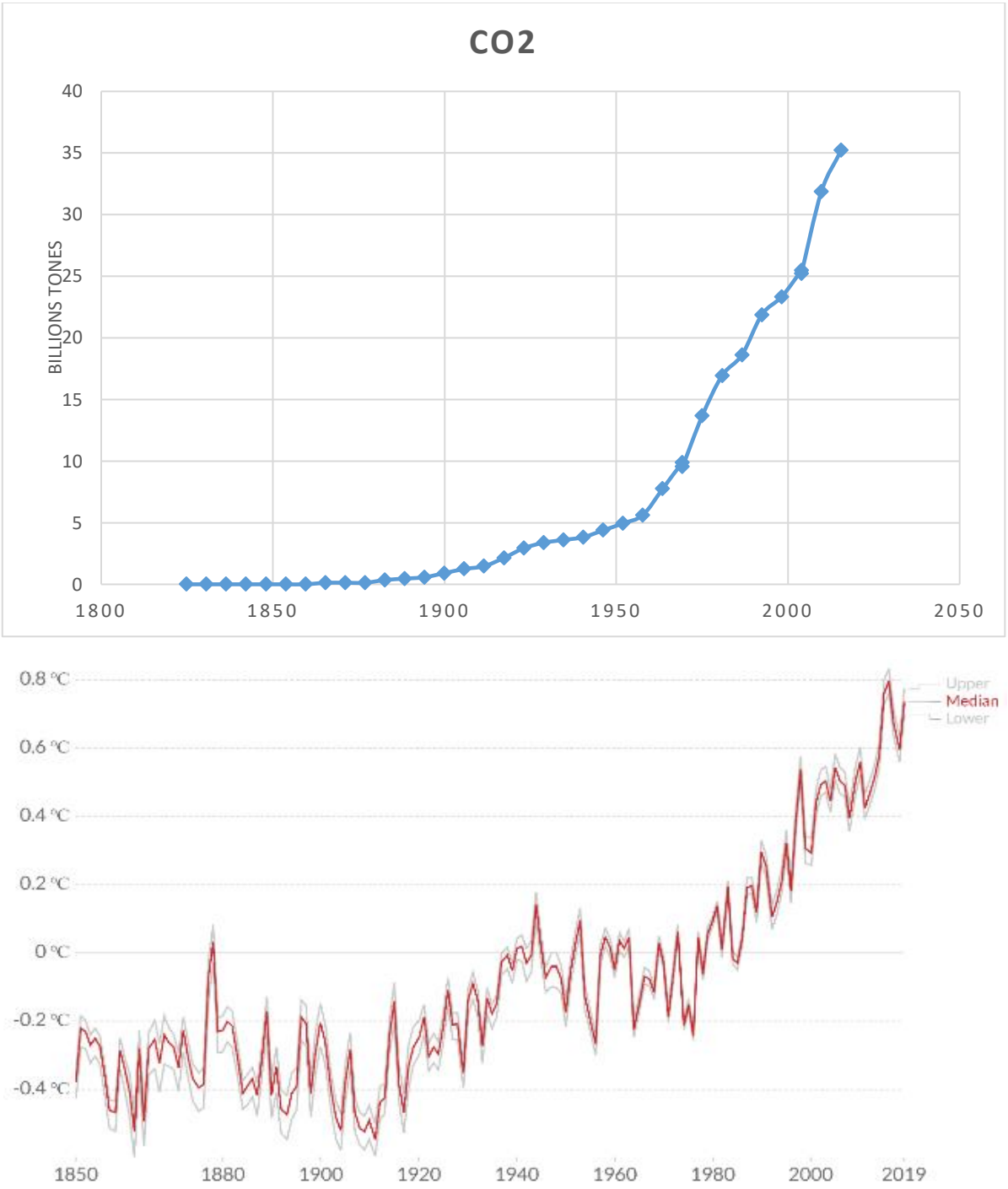

Figure 1. 3: top) Carbon dioxide (CO_2) from burning of the fossil fuels, bottom) Global average land-sea temperature anomaly relative to the 1961-1990 average temperature[2]

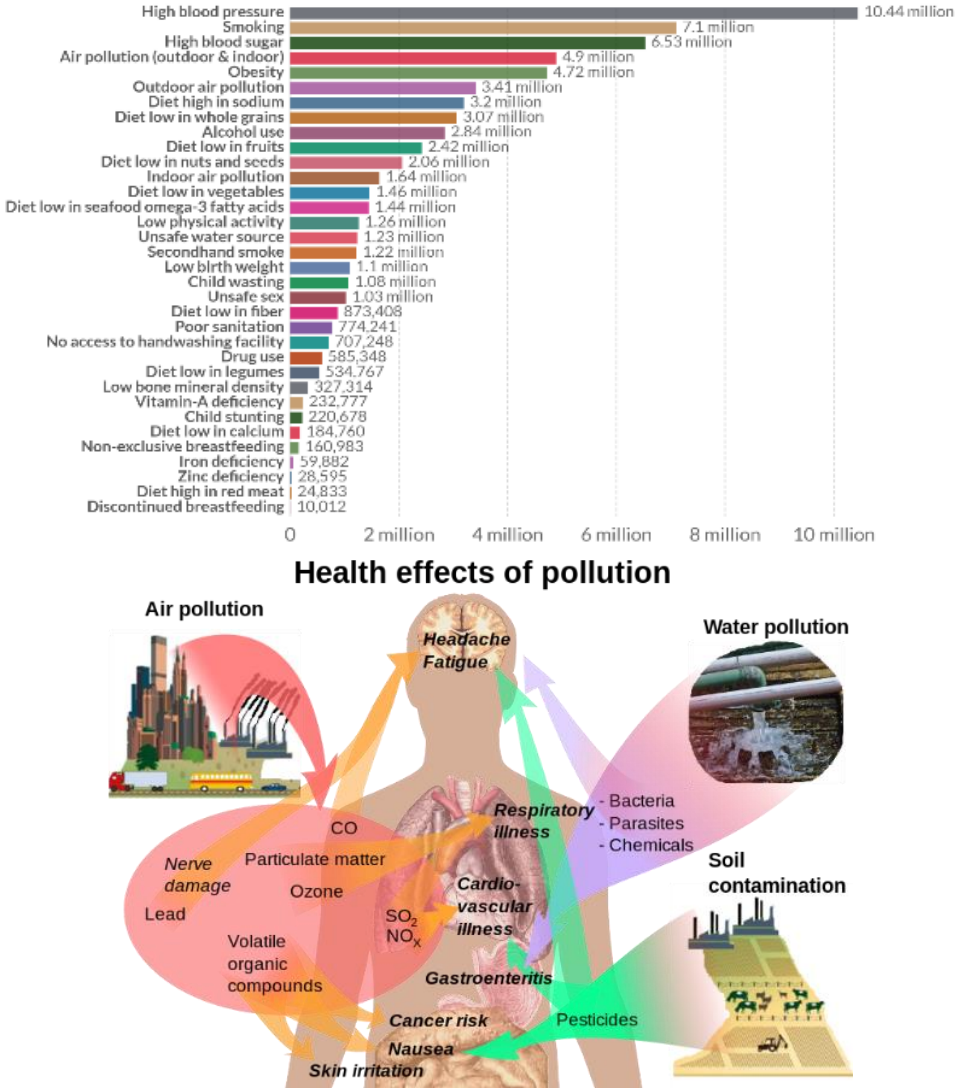

Figure 1. 4: top) Deaths by factor risk[5], word 2007, bottom) Pollution effect on health[6]

Despite all these negative aspects of fossil fuels, it is difficult to replace them with alternative energy sources or nuclear energy. Neither nuclear nor renewable energies are at present able to replace 80% of the energy provided by fossil fuels. Until newer technologies can replace combustion-based technology, fossil fuels will continue to sustain human societies and prosperity. Therefore, it is necessary to make fossil fuel technologies more efficient, less polluting, and save fossil fuels consumption. Nowadays, many new technologies contribute to the development and improvement of the combustion process, as well as reducing the level of emissions by using biofuels.

1.1. Biogas syngas mixtures

Pollution can be minimized by fuel selection; biofuels are an attractive choice in this context. Biogas and syngas have been proposed as clean and promising fuels [7], they have been introduced in many applications such as furnaces, gas turbines, and IC engines [8] and [9].

Biogas is produced by the breakdown of organic material (plant or animal material) by methanogen (microorganisms) in the absence of oxygen (anaerobically). Biogas mainly consists of methane (50% to 75% CH_4) and carbon dioxide (25% to 50% CO_2). It may contains small amounts of hydrogen sulfide (0.1%-0.5% H_2S), oxygen (O_2 0%-0.5%), hydrogen (0%-1% H_2) and nitrogen (0%-10% N_2) [10]. Carbon dioxide in biogas can have a thermal effect, as a diluent, or chemical effect if it decomposes and reacts at high temperatures; also it reduces heat value, Jeong et al. [11]**.** Biogas low caloric value problem can be recovered by hydrogen enrichment. Mameri et al. [12]examined the effect of several operating conditions, including hydrogen addition to biogas. The authors considered counter-flow configuration, laminar regime, and atmospheric pressure. Results showed that blending biogas with H_2 increases mixture heating value and makes the fuel more reactive. Leung et al. [13] investigated the stability of non-premixed flame of two compositions of biogas (60%CH_4+40%CO_2) and 50%CH_4+50%CO_2) in a simple fuel jet with a coflowing air stream. When adding a small amount of hydrogen into biogas, authors found that flame becomes more stable in a wide range of strain rates. Zen et al. [14] investigated experimentally the effect of hydrogen enrichment on the stability of biogas diffusions flame. The amount of hydrogen added was varied from 5% to 10%, it has been found that the stability of biogas flame increases significantly. Several studies reveal that hydrogen can be obtained from renewable sources such as syngas [15]-[16]. Syngas or synthesis gas is a combustible mixture produced by gasification [17] and consists of important reactive species, mainly hydrogen H_2 and carbon monoxide CO [18]. Few researches have been addressed this type of mixture of biogas and syngas or (CH_4/CO_2/H_2/CO). Mameri et al. [15] investigated numerically laminar counterflow diffusion flame under several operating conditions of strain rate and ambient pressure from 1 atm to 10 atm for seven mixtures of biogas syngas (by varying volumes of methane and hydrogen). They found that hydrogen increase in syngas leads to extending extinction limits interval. Whereas, ambient pressure increase extended strain rate operating interval, and increased extinction temperature, and NO emission. It has been also noticed that the most important path for NO production is the NO_2 route. A more recent paper by Zouagri et al [16] studied numerically flame structure and emission of the mixture biogas-syngas in a counterflow diffusion flame configuration in a laminar regime. Volumes of both methane and carbon dioxide in biogas; hydrogen and carbon monoxide in syngas were varied. The strain rate was kept at 200 s^{-1} and ambient pressure at 1 atm. The authors found that flame characteristics are highly influenced by composition of the mixture. Increasing volume of methane or hydrogen in the mixture showed an improvement in low heat value (LHV). Thickness of reaction zone and maximum flame temperature were wider and

production of H_2O and OH species become higher. They also reported that NO production was related to the volume of methane in the mixture.

1.2. Biogas-syngas mixture under the MILD regime

To obtain clean and efficient combustion, the interesting way of optimization was the use of MILD combustion of biofuels. Few studies investigated this topic, Mameri et al.[12] in a numerical simulation studied the laminar flame structure and emission of biogas in counter-flow diffusion flame configuration under MILD condition. The authors found that the chemical effect of CO_2 in the oxidizer stream leads to decrease flame temperature and species production such as NO and OH. Colorado et al. [19] carried out an experimental and numerical investigation of biogas in a cylindrical gas turbine combustion chamber under MILD combustion. It was found that the temperature in the chamber was uniform and pollutants emissions were very low than conventional combustion. The increase of oxygen concentration in the oxidizer stream led to an efficiency increase. Mahmoudi et al. [20]experimentally investigated combustion characteristics of biogas flame in a furnace under MILD combustion conditions. Results showed that NOx and CO emissions were very low with a large reaction zone and uniform temperature field along with the furnace. Shahin et al. [21] studied experimentally and numerically stabilization and flame lift-off height of turbulent non-premixed flame of biogas of jet in hot co-flow. Results showed that adding hydrogen to the mixture leads to a significant increase in the lift-off height. Huang et al. [22] conducted a numerical study regarding biogas flame under MILD combustion. The influence of many operating conditions such as oxygen concentration in the oxidizer stream and fuel composition has been undertaken. They revealed that when reducing oxygen concentration, NOx and CO levels are nearly zero. Also, they found that some biogas compositions are unaffected by the thermal field. Huang et al. [23] studied numerically the effect of fuel types (biogas and hydrogen) and pressure on MILD combustion. Their results indicated that an increase in pressure harms ignition delay of syngas mixture which is due to the decrease of OH mole fraction in the mixture when pressure increases**.** Mardani et al. [24] examined the importance of fuel jet velocity in the MILD combustion of syngas. The results revealed that an increase in fuel jet velocity leads to a good mixing between oxidizer and fuel; which also contributes to lowering the temperature, uniformizing thermal field, and reducing NOx emissions. The authors found that N_2O intermediate mechanism is the main contributor to NOx production in syngas MILD combustion. The effect of hydrogen addition to methane and syngas were investigated under MILD combustion condition by Chinnici et al. [25] . The authors found that

an increase in hydrogen leads to the growth of high-temperature regions for both fuels. Moreover, they noticed that syngas seems to be a better choice in achieving MILD combustion . Recently, an experimental and numerical study was conducted by Saha et al [26]. The authors studied combustion and stability characteristics of a syngas fuel under MILD combustion by varying fuel composition (H_2/CO ratio). The results indicated that there is no significant influence when changing fuel composition on emissions, thermal efficiency, and temperature field. They also found that pollutant emissions such as NOx and CO are almost non-existent.

1.3. Scope of the thesis

It is interesting to combine all these features mentioned above to improve the combustion process. This can be achieved by using the MILD combustion technique which is highly suitable for application with low calorific fuels [26], [27]. Moreover, hydrogen can be obtained from syngas, as it contains important amounts of hydrogen [15] and [16]. In this study, the turbulent MILD combustion of biogas-syngas mixture is elucidated. Several configurations were used to validate the numerical procedure, namely: the opposed jet flames, the bluff-body jet flames and the jet in hot co-flow flames. The first configuration is excessively used especially in one dimensional flames; moreover, experimental data are available which makes it a good candidate for validation with simple turbulent combustion models. The second configuration is essentially used to stabilize high velocity jets flames; also, it offers experimental data for validation with advanced combustion models. The last geometry represents the basic jets that are used in gas turbine chambers; furthermore, experimental data in MILD combustion are available for this configuration. After validation, effect of several parameters on the MILD combustion and emissions are achieved with the Jet in Hot Co-flow (JHC) burner. The tested parameters are: compositions of the biogas-syngas mixture, oxidizer temperature, oxygen concentration and fuel injection velocity.

Previous studies on the adopted configurations

1.3.1. Case of the opposed jets flames of biofuels

The turbulent counter-flow flame is one of the most used configurations in combustion study. It consists of two opposed jets impinging one on another which generates a simple axisymmetric flow field with a stagnation region and a flat thin flame, Fig 1.5 [28]. This configuration facilitates direct measures and simplifies phenomenon equations for the flow simulation. For many decades the counterflow flames make the subject of several studies, here some studies that dealt with biofuels in opposed jets configuration will be summarized. Diffusion flames in opposed jets of biogas were numerically studied by Mameri et al. [16]. [15].

Effects of composition, pressure and injection velocities were considered; detailed chemistry was adopted. It was found that CO_2 present in biogas can have thermal and chemical effects; when CO_2 increases, flame temperature, chain carrier radicals (OH and H), and NO emission are all reduced. However, pressure increases leads to an increase in the temperature and reduce the mass fraction of NO, especially at high pressures. The effect of dilution of biogas (CH_4+CO_2) by N_2 on the counterflow diffusion flame was studied by Saeed et al. [29]**.** It was found that augmentation of CO_2 reduces H, O, and OH radicals confirming the results of Mameri et al. Also, the NO profiles showed a significant decrease in peak value when CO_2 increase**.** Hadef et al. [30] studied the laminar counterflow flame of the biogas (75%CH_4+25%CO_2) blended by hydrogen (from 0 to 20%) and by water vapor with a volume of 10% to 50% while the oxidant was heated at 1200K. A constant strain rate of 120 s^{-1} was adopted and detailed chemistry was used. It was found that the addition of hydrogen increases the Lower Heating Value (LHV) and temperature, the intermediate species OH, and the production of C_2H_2. While dilution by H_2O reduced temperature and both pollutant species CO_2 and CO. The addition of H_2 leads to an increase in NO production, the reason is the increase in temperature; whereas, the addition of H_2O reduced them. Another study on dilution effect on syngas opposed jets flame was conducted by Giles et al.[31]. The syngas was simulated by two compositions (50%H2+50%CO) and (45%H_2+45%CO+10%CH_4) and diluents were CO_2, N_2, and H_2O. The results showed that the addition of methane to syngas (second composition) decreases the flame temperature peak but increases the formation of prompt NO. All three diluents (CO_2, N_2, and H_2O) are effective in decreasing NOx emission from syngas flames; moreover, both CO and H_2O diluents are more effective than N_2. Extinction characteristics of the flame of syngas (H_2+CO) diluted by CO_2 and H_2O were examined numerically by Suresh et al. [32]. The opposed jet laminar flame was considered in a 2D axisymmetric computation. The results showed that the dilution by CO_2 increased the stoichiometric mixture fraction and shifted the reaction zone towards the oxidizer side; moreover, the reactivity of the flame has been decreased. Safer et al. [33] reported numerically the flame structure and NO emission of a syngas (H_2+CO) opposed jet turbulent diffusion flame. The authors considered a wide range of hydrogen percentage (H_2/CO=0.4 to 2.0), operating pressure varying from 1 to 10 atm, and at a high strain rate of 150s^{-1}. The RANS (Reynolds-Averaged Navier Stokes) approach was used. The results showed that the maximum flame temperature decreases with H_2 enrichment while the peak values of OH and H radical increase. However, pressure increment reduces OH, O, and H radical peak values. The comparison between three routes of NO formation (thermal,

prompt, and N_2O) revealed that the thermal path is the most important for the considered operating conditions.

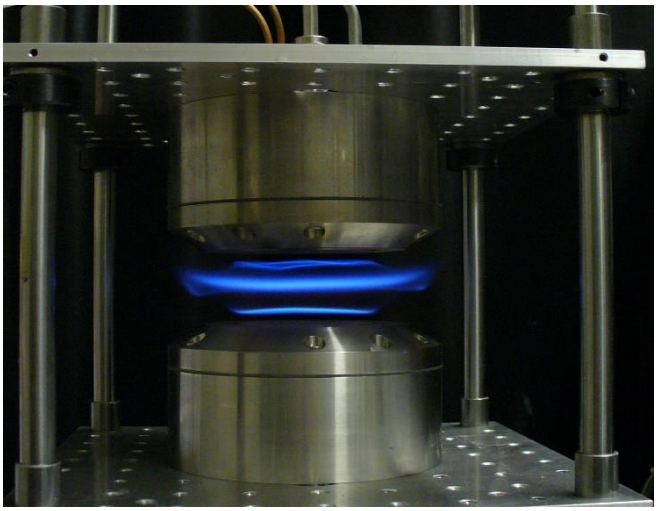

Figure 1.5: Triple flames in the opposed jet configuration [28].

1.3.2. Case of bluff-body flame stabilization

As it is known, all gas turbines operate at a very high airflow velocity which leads to the instability of the flame. Consequently, the flame is blown away resulting in incomplete combustion, which increases emissions and unburns. Moreover, the high flow velocity is also responsible for pressure drop [34]. To stabilize the flame, many techniques are used, among them: bluff-body flame holders and swirlers. The bluff-body flame holder is a commonly used practical way to stabilize the flame. The recirculation of hot gas behind a bluff body can help in the reigniting of gas mixtures and hence the flame stabilization [35]. The bluff body with a central jet is commonly employed to stabilize the diffusion flame. Whereas the bluff-body with a simple solid cone or solid plate is used to stabilize the premixed flame. The central injectors are designed to have the widest possible operating range while minimizing pollutant emissions and pressure fluctuations. Whereas, the stabilization of the flame in the flow is carried out with a flame holder behind which a recirculation zone arises. The low velocity behind the obstacle allows the flame to hold on. In addition, recirculation brings hot gases and radicals that sustain the combustion[36]. The bluff body is often used as a flame hang-on. It consists of a cylinder installed in the center of the injector. The length of the recirculation area is approximately the diameter of the bluff body. The swirled flow allows obtaining a much greater recirculation than the bluff body. The swirl creates a helical flow that produces a depression at the center of the flow. When the angle of the swirl blades is high, the depression in the center becomes large enough to reverse the direction of flow. The size and shape of internal recirculation depend

mainly on the non-dimensional number "S" (swirl number), which corresponds to the flow of quantity of tangential motion divided by the flow of quantity of axial motion.

Recirculation is also strongly dependent on the angle of the divergent at the entrance to the combustion chamber [37] [38] and other factors such as the presence or not of a bluff body, containment or combustion, Beltagui et al. [39]. Even small changes in these parameters can significantly alter flow Charles et al. [40]. Recirculation usually occurs for a swirl number of about 0.6 [41] , but this number may be lower depending on the experimental conditions (S=0.2 for example for Chen et al. [42].

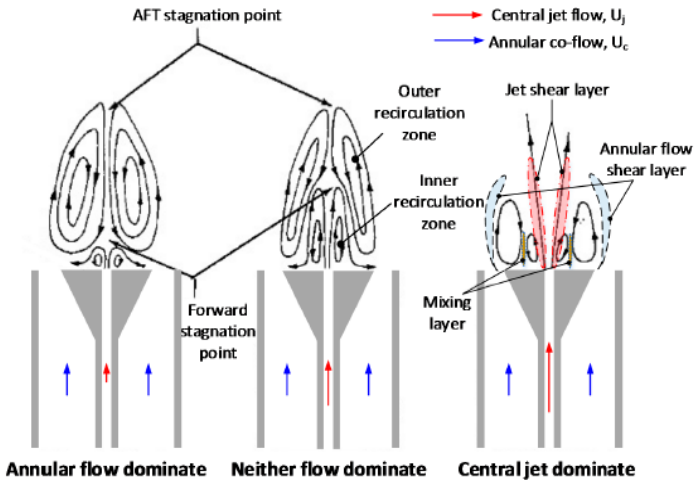

Figure 1. 6: a schematic of time-averaged flow fields downstream of a bluff body [43]

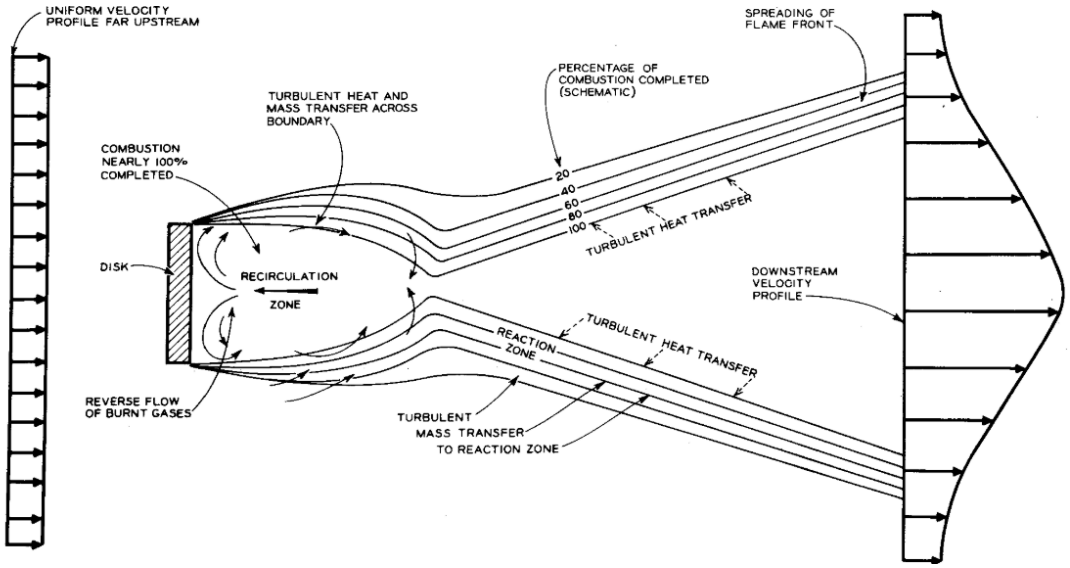

Figure 1. 7: Flow patterns in confined bluff body premixed swirl stabilized combustor Williams, F. [44]

The bluff-body flame studied here conducted by Dally et al. [45]and the experimental data has been made available from the University of Sydney website [46]. Dally et al. [47] investigated the performance of standard and modified k−ε and Reynolds stress models for

turbulence and flame sheet model with beta probability density function for combustion. They found that both the k−ε and Reynolds stress models in the standard form failed to predict the flow field sufficiently accurately. The value of turbulence model constant of $C_{\varepsilon 1}$ = 1.6 was proposed to improve the prediction of the flow field. Merci et al. [48] applied a new cubic non-linear eddy viscosity turbulence model with a constrained equilibrium model to investigate the prediction. They found that the improvements in flow field prediction using the new cubic model were acceptable. As a result, the prediction of temperature profiles at downstream locations was not satisfactory. Yilmaz et al. [49] compared the numerical results between Large-Eddy Simulations (LES) and the standard k–ε model using the Probability Density Function (PDF) approach with the flamelet model and found that the LES model gave better predictions. The effects of hydrogen composition and nonflammable diluent mixtures on the combustion and NO emission characteristics on bluff body configuration were examined by Chen et al. [50]. The results showed that increased hydrogen leads to a decrease in the radial velocity and strain rate, which was important for mixing and contributing to reduced NOx formation.

1.3.3. Case of the JHC burner

The Jet in Hot Burner (JHC) or Adelaide Jet in Hot Burner (AJHC) is a laboratory-scale burner (Figure 1.6) [51] used to emulate flameless and precisely MILD combustion. This burner permits a wide range of combustion parameters to be varied, such as injection temperature and reactants concentrations in both laminar and turbulent flames. Detailed characteristics of the MILD combustion regime in the JHC burner operated with three oxidizer oxygen concentration levels (3%, 6%, and 9%) were investigated by Dally et al. [51]. Results showed that increasing oxygen mass fraction from 3% to 9% in the hot oxidant stream leads to substantial changes in the flame structure; where the temperature peak rises by 400 K and a threefold rise for both NO and OH. Christo et al. [52] investigated the turbulent non-premixed methane-hydrogen flames (CH_4+H_2) issuing from the JHC burner. The performance of various turbulence models, namely: standard k-ε, realizable k-ε, and RNG k-ε were tested. It was found that the standard k–ε turbulence model with a modified constant $C_{\varepsilon 1}$ (from 1.4 to1.6) provided good agreement with experimental data. Also, differential diffusion was found to have a strong influence on the accuracy of predictions. The influence of turbulence kinetic energy at the inlet boundaries on the prediction of mean temperature and mass fraction was examined by Aminian et al. [53]. MILD combustion in the JHC burner is considered for three different oxygen levels in the hot co-flow steam. Results showed that turbulent kinetic energy has a significant influence on the prediction of temperature and species mass fraction at both upstream and downstream of the

burner. In turbulent non-premixed MILD combustion of CH_4+H_2, a numerical study was conducted by Mardani et al. [54] to illustrate the effects of hydrogen content in fuel on the flame structure. Two co-flow oxygen levels (3% and 9%) and three fuel mixtures (5%H_2+95%CH_4, 10%H_2+90CH_4, and 20%H_2+80CH_4) were considered. The results showed that hydrogen addition to methane leads to a decay in the reaction zone, an increase in mixture fraction and strain rate, and turbulent kinetic energy. They also found that hydrogen addition to methane leads to higher levels of OH, CH_2O, and HCO which contributes to higher reaction intensities, mixture ignitability, and heat release rate.

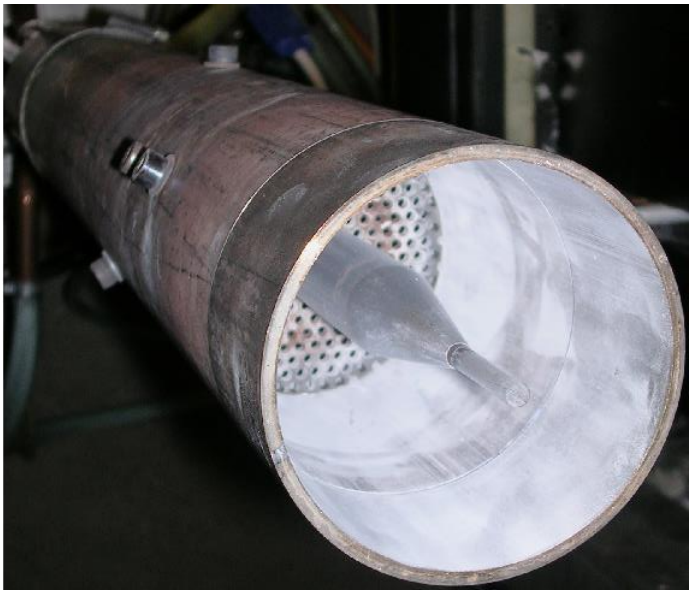

Figure 1. 8: The Jet in Hot Coflow burner [55].

Chapter II

Biofuels and flameless combustion regime

2.1. Biofuels

In the context of fuel supply security, the quest for improved efficiency and lower emissions targets seems straightforward. Increasing energy conversion efficiency or switching to more carbon-neutral fuels are two simple ways to reduce CO_2 emissions. Many industries are now moving towards using biofuels. The most drawback of biofuels is their low calorific value which causes many issues during combustion. According to their nature and composition, fuels can be classified into gaseous and liquid and then further divided by their calorific value within the gaseous fuels, an example of the classification is shown in Table 2.1.

Table 2. 1: Classification of fuels [56]

	Typical composition	**Lower heat value kJ/Nm^3**	**Typical specific fuels**
Ultra/ low LHV fuels	H_2<10% CH_4<10% N_2+CO>40%	<11,	Blast furnace gas (BGF) Airblown Biomass gasification
High hydrogen gaseous fuels	H_2>50% C_xH_y=0-40%	5 -11	Refinery gas Petrochemical gas Hydrogen power
Medium LHV gaseous fuels	CH_4 < 60% N_2+CO_2 = 30-50% H_2 = 10-50%	11-30	Weak natural gas Landfill gas Coke oven gas Corex gas
Natural gas	CH_4 = 90% C_xH_y = 5% Inerts = 5%	30-45	Natural gas Liquefied natural gas (LNG)
High LHV gaseous fuels	CH_4 and higher hydrocarbons C_xH_y > 10%		Liquid petroleum gas (butane, propane) Refinery off-gas
Liquid fuels	C_xH_y, with x > 6	32-45	Diesel oil Naphtha Crude oils Residual oils Bio-liquids

Figure 2.1: Fuel used in high-efficiency gas turbines [56]

2.2. Biogas definition

This work focuses on the use of biofuels, namely: biogas and syngas. The former is a gas produced by anaerobic fermentation of different forms of organic matter and composed mainly of methane (CH_4) and carbon dioxide (CO_2). Typical feedstocks for biogas production are manure and wastewater, residues from agricultural production, the organic fraction of household and industrial waste, and energy crops such as maize and grass silage [57]. Biogas has a Low Heat Value (LHV) of 5 to 7 kj/Nm^3. This renewable energy can be used in different forms: combustion for the production of electricity and heat, production of fuel, or injection into the natural gas network after purification [58]. To produce biogas, organic matter ferments with the help of bacterial communities. Four fermentation stages move the organic materials from their initial composition to their biogas state (Fig. 2.2):

- The first step in the digestion process is the hydrolysis stage where insoluble organic polymers (such as carbohydrates) are broken down, making them accessible to the next stage of bacteria called acidogenic bacteria [57].
- Acidogenic bacteria convert sugars and amino acids into carbon dioxide, hydrogen, ammonia, and organic acids.
- In the third step, the acidogenic bacteria transform the organic acids into acetic acid, hydrogen, ammonia, and carbon dioxide, thus allowing the final stage, the methanogens

- Methanogens convert these final components into methane and carbon dioxide, which can then be used as flammable green energy.

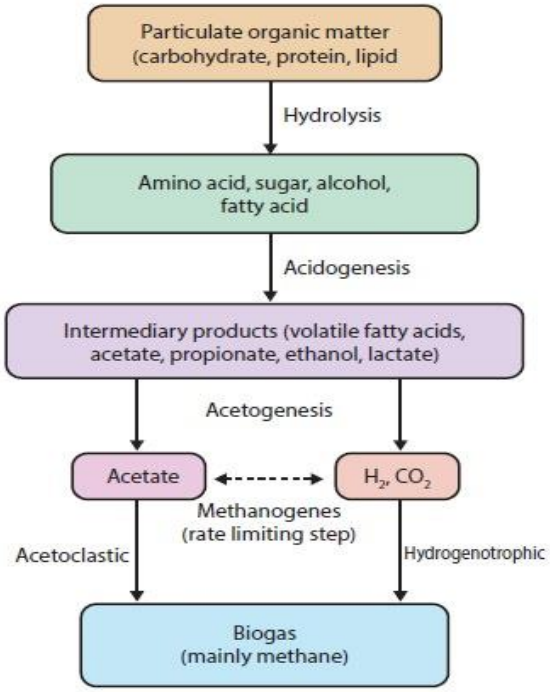

Figure 2.2: The subsequent stages of the anaerobic digestion

Biogas mainly consists of methane and carbon dioxide with several amounts of impurities. The composition of biogas varies depending on the substrate. Biogas with more than 45% of the methane content is flammable [59]. Methane is the main component of organic gas or biogas. It is an odorless and colorless gas, characterized by a high-energy value (802 kJ/mol). While carbon dioxide (CO_2) is a colorless, odorless, and non-flammable gas it is not toxic but the main cause of suffocation. Hydrogen sulfide (H_2S) is a gas formed by the demolition of amino acids. It is a toxic and flammable gas, characterized by a rotten egg odor, detectable for a molar fraction of 0.7 to 150 ppm. H_2S affects the nervous system and causes death. Finally, water vapor (H_2O) is also present in biogas. Generally, at saturation in raw biogas, it can damage biogas-upgrading elements such as solenoid valves, regulators, burners, etc.

Table 2. 2: Components of biogas

Components	Percentage (%)
Methane (CH_4)	50-75
Carbon dioxide (CO_2)	25-50
Nitrogen (N_2)	0-10
Hydrogen (H_2)	0-1
Hydrogen sulfide (H_2S)	0-3
Oxygen (O_2)	0-2

2.2.1. Biogas utilization

- Biogas provides an alternative fuel for vehicles. However, the quality of biogas should be improved and make it equivalent to that of natural gas. Removal of particulates, carbon dioxide, hydrogen sulfide, and moisture can be done to increase the methane percentage up to 95%. The presence of carbon dioxide reduces the fuel value and hydrogen sulfide with water increasing corrosion. Biogas after purification can be blended with natural gas and used as a fuel for vehicles [60].
- Biogas is a source of energy to produce heat and electricity. Traditionally biogas is used as fuel for boilers and provides heat to the anaerobic process. Digester plants produce a large amount of biogas than is needed, these excesses of biogas can be used as energy for the other processes.
- Biogas can be used in combustion engine generators and in turbines to produce heat and electricity for plants operation. In the biogas plants, the generator uses biogas to produce electricity, and waste heat produced by the generator is transferred to heat the digester.
- Biogas is used for cooking and lighting in many developing nations. Biogas produced from the anaerobic digester of waste material is connected directly to the low-pressure stove and used for cooking purposes[61].
- In Biogas technology all the waste material is dumped into the anaerobic container, this, in turn, reduces the spread of pathogens present in the waste to the environment and avoids bad odor. In this way, it helps to improve the hygienic condition.
- The digested organic material after biogas production is a rich source of nitrogen and other nutrients. It can be used by the farmer as a fertilizer for their crop fields. Through this, it saves the economy to the farmers in buying the chemical fertilizer.
- By the usage of waste, it avoids environmental pollution such as land, water, and air pollution.
- Biogas provides job opportunities to the local people. Finally, it improves the economic standard of people.

2.2.2. The advantages and drawbacks of biogas

Biogas is like any gas has advantages and disadvantages and we will now recall the main advantages and disadvantages [62] :

- Renewable energy source: biogas is a sustainable energy source and its existence is linked to the existence of waste since the main source of gas production is waste.

- Biogas is an environmentally friendly gas, it is not polluted, its production does not require oxygen, and reduces deforestation.
- Reduces landfills as they are the main source of biogas production.
- Can be used as a source of power generation used in various applications such as electricity, heating, and vehicle fuel.
- Biogas production results from the use of gases produced by landfills, which reduces the impact of global warming and the recycling of biodegradable organic waste.

2.2.4. The drawbacks of biogas

- Very few technological advancements have been made or introduced to streamline and make the process cost-effective and hence the systems currently in use are not efficient enough. Most investors are unwilling to invest in biogas production, although such investments may be a possible solution to the problems encountered.
- After refining and compression, the biogas still contains impurities. If the generated biofuel was used to power cars, it could corrode the metal parts of the engine. This corrosion would lead to an increase in maintenance costs. The gas mixture is much more suitable for stoves, water boilers, and lamps.
- Like other renewable energy sources (solar, wind, for example), biogas production is also affected by weather conditions. The optimum temperature bacteria need to digest waste is around 37°C. In cold climates, digesters need heat to maintain a constant supply of biogas
- Another disadvantage of biogas is that industrial biogas plants only make sense when raw materials are abundant (food waste, manure). For this reason, biogas production is much more suitable for rural and suburban areas.

2.3. Syngas definition

The Synthesis gas (Syngas) is defined as a gas with hydrogen H_2 and carbon monoxide CO as the main components of fuel. Synthesis gas can be produced from many sources, including natural gas, coal, biomass, or virtually any hydrocarbon feedstock, by reaction with steam or oxygen. Synthesis gas is an essential intermediate resource for the production of hydrogen, ammonia, methanol, and synthetic hydrocarbons [63]. In principle, synthesis gas can be produced from any hydrocarbon, resulting in the wide variety of raw materials used in large-scale synthesis gas production, including natural gas, liquid hydrocarbons, biomass, and coal. There are three main reaction pathways commonly used in industry for the production of

synthesis gas: steam reforming, partial oxidation, and oxidative steam reforming or auto-thermal reforming [63].

2.3.1. Steam reforming

Steam reforming is the conversion of gaseous hydrocarbons to a mixture of CO and H_2 by the addition of steam and heat. Steam reforming most often works at temperatures between 700 and 1000 ° C uses natural gas (methane) as the raw material and proceeds as shown in the following reaction: $CH_4 + H_2O \leftrightarrow CO + 3H_2$ with $(\Delta H°)_{298K} = 253,7$ kJ/mol

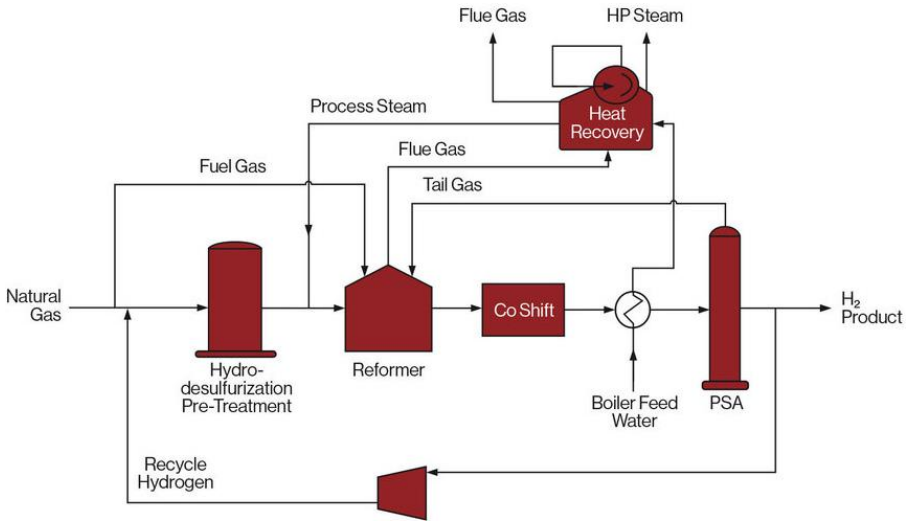

Figure 2. 3: Steam Methane Reforming (SMR) - Syngas Production [64]

2.3.2. Partial oxidation

Partial oxidation is the conversion of hydrocarbons to syngas under an oxygen (O_2) deficient atmosphere, as in the following reaction which is slightly exothermic and can proceed at high temperatures (> 1200 ° C) without a catalyst or at lower temperatures (800 to 1000 ° C) with a catalyst:

$$C_xH_y + 0.5x\ O_2 \rightarrow xCO + 2H_2 \qquad (1.1)$$

The process requires O_2 rather than steam and this can be supplied either by air or by pure O_2. Downstream processing requirements can be hampered by nitrogen (N_2), so the use of air as a source of oxygen is not always recommended. However, both raw materials are used in industry. Synthesis gas produced by the partial oxidation process has a lower H_2 / CO ratio (<2) than steam reforming and is more suitable for the production of methanol.

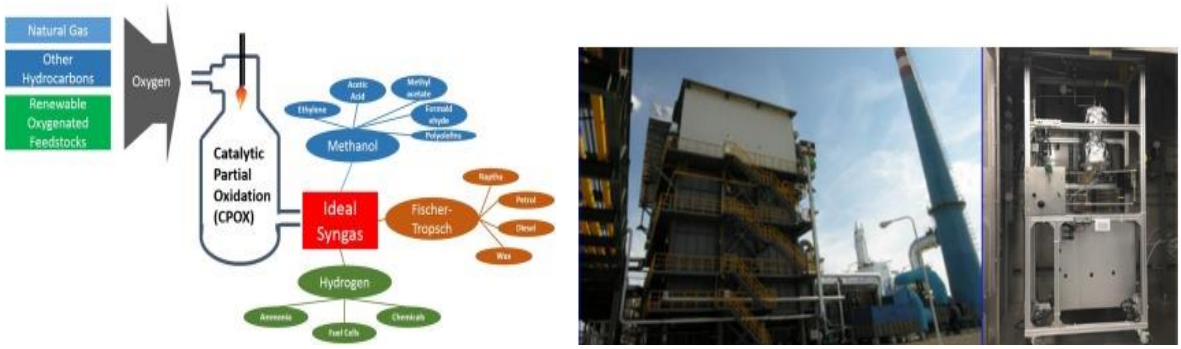

Figure 2. 4: Catalytic Partial Oxidation (CPOX) reactor for syngas production [65].

2.3.3. Oxidative Steam Reforming

It is the production of syngas via the combination of steam reforming and partial oxidation in a single reaction chamber. In theory, the O_2 feed is balanced so that the energy produced by the partial oxidation reaction is equivalent to the energy required in the steam reforming reaction, making the process self-sufficient. An example of the reaction of methane is given in the following equation:

$$CH_4+O_2+2H_2O \rightarrow 4CO+10H_2 \qquad (1.2)$$

The process operates between 950 and 1100 ° C and can be adjusted to achieve an H_2 / CO ratio between 1 and 2.5 and is, therefore, able to provide all downstream applications with the appropriate quality syngas. As with partial oxidation, air and pure O_2 can be used as the raw material, although air presents more difficulties for downstream processing. Despite the flexibility of the synthesis gas production methods, partial oxidation and oxidative steam reforming, are not suitable for large-scale production facilities. The cost of a large oxygen production facility is excessively high.

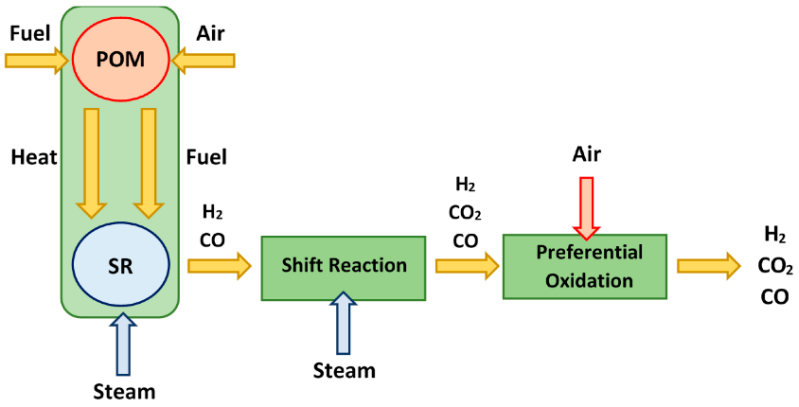

Figure 2.5: The auto-thermal reforming scheme [66].

Syngas is a combustible gas mixture and its average composition is given by the following table:

Table 2.3: Syngas components [67].

Component	Volume %
Hydrogen	45-50
Carbon monoxide	20 - 25
Carbon dioxide	15 - 16
Methane	10 - 14
Light hydrocarbons	2 - 4

2.3.4. Syngas utilization

- Syngas is used to produce a wide range of synthetic products, namely solvents, clothing, and fuels.
- It is used in the production of methanol, which is the source of hundreds of products, including glue.
- Hydrogen obtained from acetic acid and formaldehyde is used as fuel for spacecraft rockets because H_2 provides high energy content per unit weight.
- Fertilizers also have their origin in syngas.
- The H_2 obtained from synthesis gas is used in the production of NH_3 and the hydrogen itself is used in the refinery to extract gasoline and more diesel from crude oil.
- Hydrogen made from synthesis gas is being promoted as the energy vector of the future. Today it is used as a fuel for launch rockets for spacecraft in which a high energy content per unit weight is valuable and a fuel cost is minor.

2.3.5. The advantages and disadvantages of syngas

- Independent power supply for installations using syngas.
- Reduced energy costs, increased predictability and stability
- Efficient and economical combined heat and power supply.
- High electrical efficiency compared to other power generation technologies (steam or gas turbines).
- Ideal for an electric power range from a few hundred kW to 20-30 MW.
- Substitutes for conventional fuels.
- Benefits for the environment by reducing greenhouse gases.

In addition to the disadvantages of syngas, namely low calorific value, and corrosivity, this gas is salty, acidic, and dangerous.

At this point, it can be deduced that biogas and syngas can be selected to minimize cost and emissions despite their drawbacks. The other way of optimization can be operated on combustion mode. Here we adopt the oxy-fuel combustion mode, based on reactants preheat and dilution, which will be elucidated in the following sections.

2.4. Introduction to flameless combustion: interests and applications

2.4.1. Preheating reactants technique: means and consequences

With the energy crises that the world has known for several decades, many studies have been launched to find better, more efficient solutions that consume less energy. while producing fewer pollutants. Especially in terms of NO_x, CO_2, CO, and soot. Preheating the oxidizer (or even the fuel), by recovering the heat lost in the fumes has been proven to be a major solution for reducing energy costs, and reducing energy expenditure. Also, it is suitable for the LHV gas by this heat input (Fig. 2.6). In fact, with conventional technologies, large heat flux is lost in the form of sensitive heat in the flue gas, at a fairly high temperature. The principle is to recover this loss by heating the oxidizer (or the fuel) at the injection. This increases the energy input without necessarily increasing the amount of fuel used (Fig.2.7). Several methods are possible to do this, but they are not all capable of offering the same efficiency.

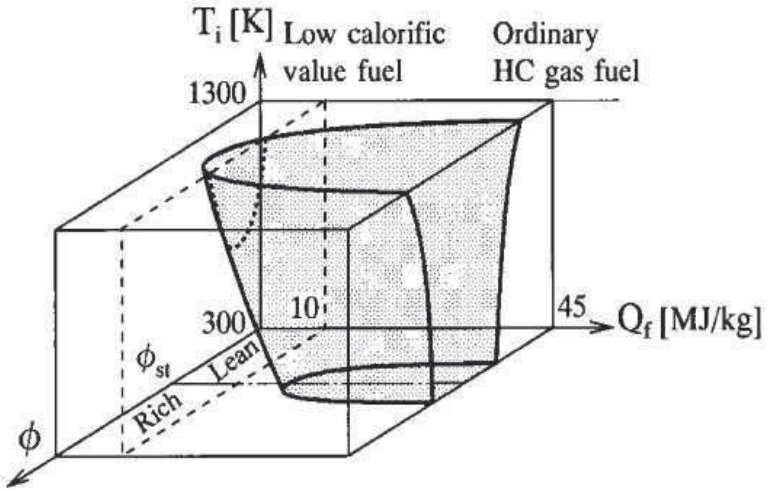

Figure 2.6: Flammable domain as a function of calorific value of fuel, Q_f, the initial temperature of the mixture, T_i, and mixture equivalence ratio[68].

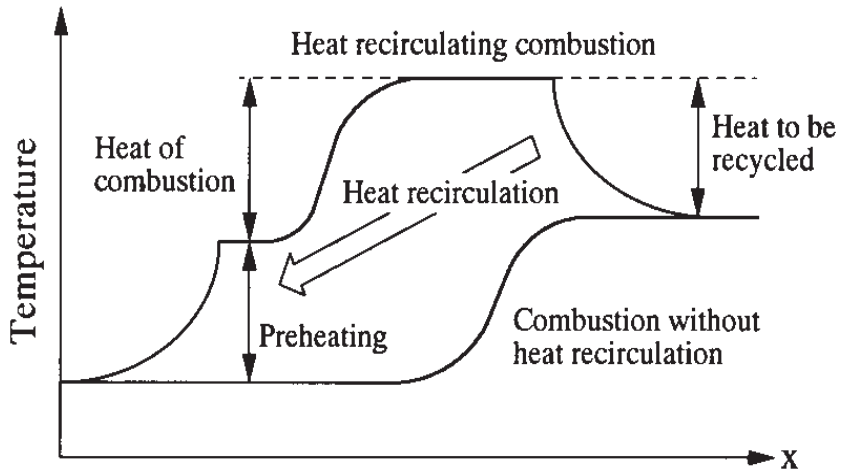

Figure 2.7: Temperature history of heat-recirculating combustion of premixed reactants in a one-dimensional adiabatic system[68].

Milani et al. [69] defined the combustion efficiency with combustion air preheating by regenerator as :

$$\Psi = \frac{H_{1.C}+H_{AIR}-H_{FLUE\ GAS\ INLET}}{H_{1.C}} \quad (2.3)$$

and the relative rate of air preheating as:

$$\varepsilon = \frac{T_{AIR\ OUTLET}-T_{AIR\ INLET}}{T_{FLUE\ GAS\ INLET}-T_{AIR\ INLET}} \quad (2.4)$$

With :

- $H_{1.C}$: the lower calorific value of gaseous fuel (MJ / m^3)
- H_{AIR}: enthalpy of preheated combustion air (MJ / m^3)
- $H_{FLUE\ GAS\ INLET}$: enthalpy of the fumes at the inlet of the heat recovery unit (MJ / m^3)
- $T_{AIR\ OUTLET}$: air temperature at the heat recovery outlet (° C)
- $T_{AIR\ INLET}$: air temperature at the inlet of the heat recovery unit (° C)
- $T_{FLUE\ GAS\ INLET}$: flue gas temperature at the heat recovery inlet (° C)

Figure. 2.8 shows the variation in combustion efficiency as a function of the temperature of the flue gases at the inlet of the air heat recovery means for different relative air preheating rates. It shows the importance of the efficiency of the heat exchanger on the thermal efficiency of the installation, especially for high flue gas temperatures. This depends on the geometry of the exchanger, the materials used, and the system itself with recuperative metal burners. The maximum temperature reached is of the order of 873K; the preheating efficiency of the oxidizer then approaches 60%. Regenerators consist of storing heat in compact beds formed of ceramic balls or refractory honeycombs operating in alternating burnt gas/oxidizer flows as shown in

Fig. 2.9. With these exchangers, inlet temperatures greater than 1273K can be reached, then bringing the temperature of the burnt gases closer together, and inducing a preheating efficiency, which can reach 80% and more. This, therefore, has the effect of increasing the thermal efficiency of the process.

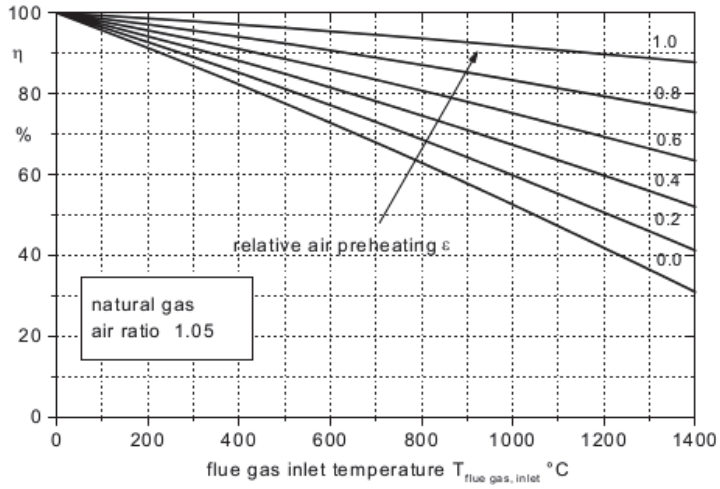

Figure 2.8: Variation of combustion efficiency as a function of the temperature of the flue gases at the inlet of the heat recovery unit for different relative air preheating rates [70].

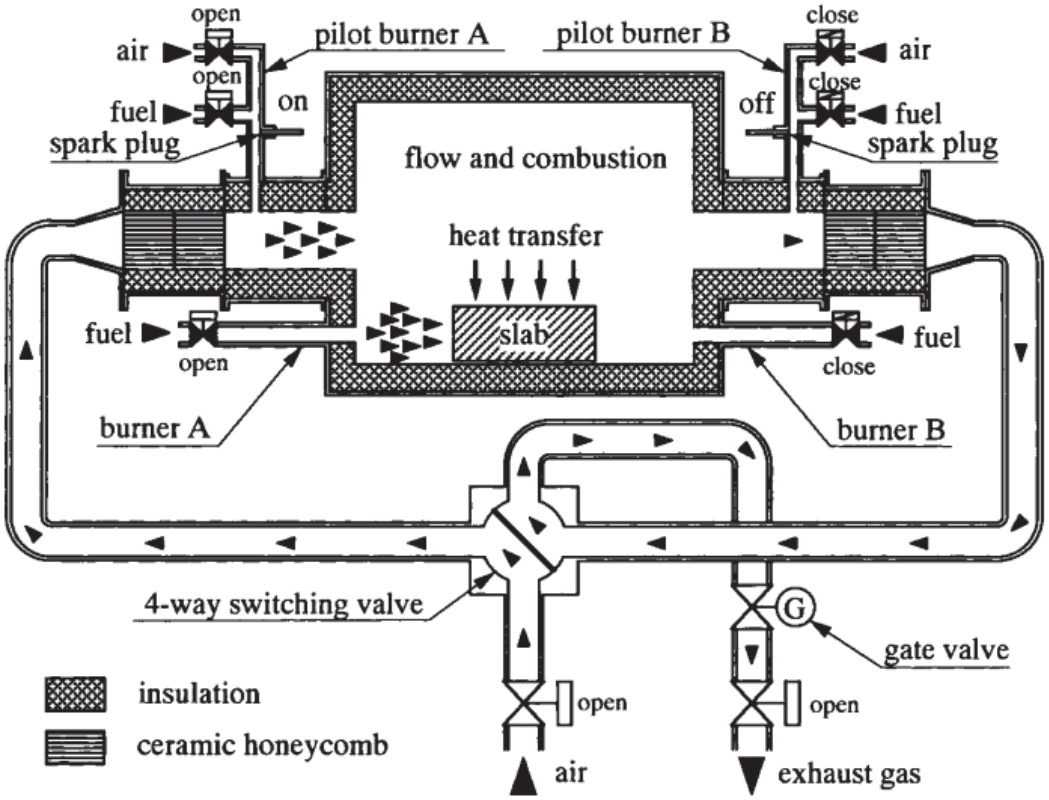

Figure 2.9: Diagram of a recirculating heat furnace operating with high-frequency regenerators alternating flows [68].

Research and developments aimed at optimizing these staging techniques on regenerative burners have led to a new ultra-low-NOx combustion process, known as ‘flameless

combustion, due to the absence of visible flame in the furnace. This mode of operation is a new combustion regime for industrial furnaces. It allows the recovery of heat from the flue gases, while controlling temperature peaks, and consequently the formation of NOx, and thermal stresses, even at high air preheating temperatures.

2.4.2. The flameless combustion regime

Regenerative flameless combustion burners

Associated with air preheating of regenerative burners, flameless combustion is an innovative technology in furnaces that combines very good energy efficiency with very low pollutant emissions by separating fuel and air injections. The use of burners operating continuously in flameless combustion in industrial furnaces has also shown its effectiveness in terms of product quality and lower costs.

Depending on the country, different flameless combustion burners have been developed based on this extreme separation of reactants. The regenerative burners REGEMAT 350 FLOX [71] in Fig. 2.10 from the German manufacturer WS have a central fuel jet, surrounded by several air jets. It is a regenerative burner with a nominal power of 200 kW, which can operate in two combustion modes. The first is the flame mode dedicated to heating the oven. Combustion is carried out by mixing air and gas at the burner nozzle and the flame is detected by ionization. When the oven temperature exceeds the auto-ignition temperature, the burner switches to flameless oxidation mode and self-regenerating mode. The burner includes six regeneration blocks: three to preheat the combustion air and the others to extract the exhaust gases from the furnace. A series of reversing valves mounted on the burner allow the switching at the operation level of the regeneration blocks.

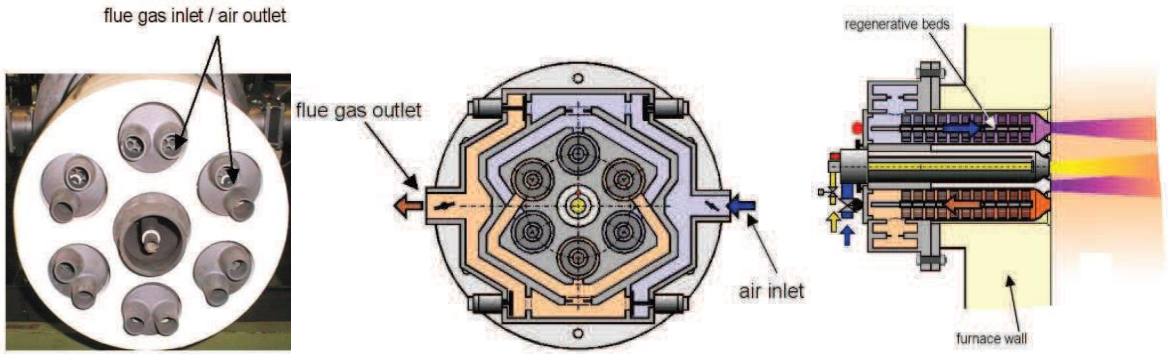

Figure 2.10: The burner WS REGEMAT FLOX [71].

In Japan, flameless combustion burners exist in many industrial applications (ceramic and steel industries) and are produced by the companies NFK and NKK. The NFK HRS - DL

burner (Fig. 2.11) is a compact regenerative burner, with ceramic honeycombs, ensuring a very efficient recovery of the energy lost by the fumes. Its geometry, consisting of two separate jets of gas on either side of a central air jet, permits operation in flameless combustion regime. This makes it possible to considerably reduce NOx emissions, and to obtain a homogeneous temperature distribution. As illustrated through these two examples, regenerative flameless combustion burners are based on the same characteristics regardless of their geometries: a strong air preheating provided by the regenerative system operating in alternating mode and injections separated and far removed from the fuel and oxidizer.

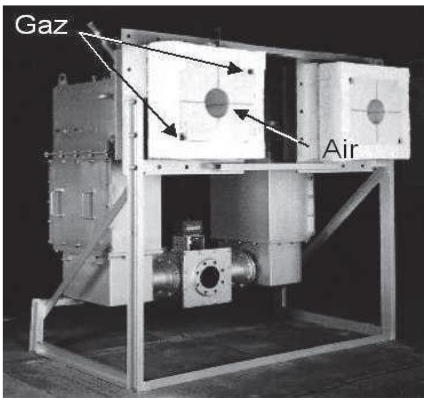

Figure 2.11: A pair of NFK HRS - DL burners [72].

2.4.3. Definitions of the flameless combustion mode

The diagrams of Fig. 2.12 compare the flameless combustion mode to the conventional one in a burner. In conventional combustion, air and fuel are introduced into the combustion chamber in such a way as to rapidly promote their mixing and thus produce a stable flame attached to the burner. In the flameless combustion mode, the air and fuel jets are separated and strongly pulsed. They will then entrain and mix with a large amount of flue gas present in the furnace before meeting and reacting. Combustion, therefore, takes place in a dilute environment with low oxygen concentration and at a temperature close to the temperature of the flue gas and higher than the auto-ignition temperature. It occupies a larger volume; the temperatures are lower and more homogeneous, without noticeable peaks, and no visible flame [27].

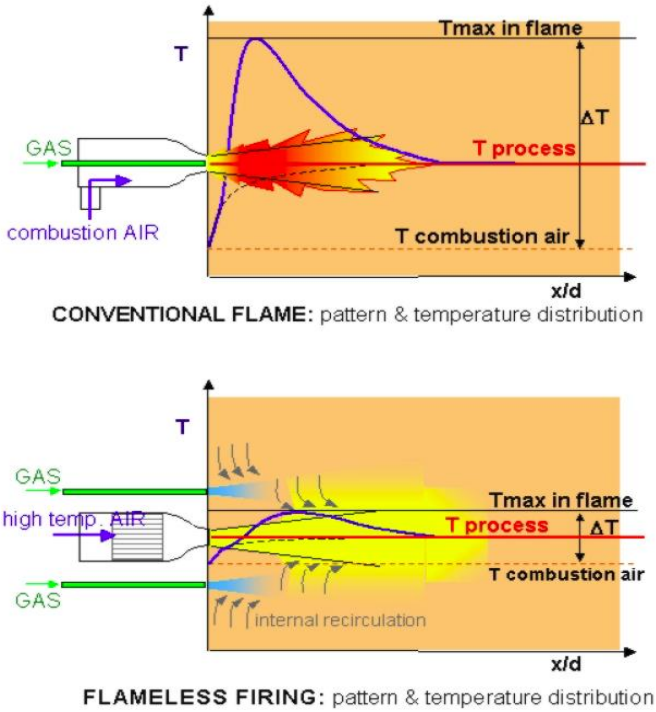

Figure 2.12: Comparison of the two combustion modes: conventional and flameless [73].

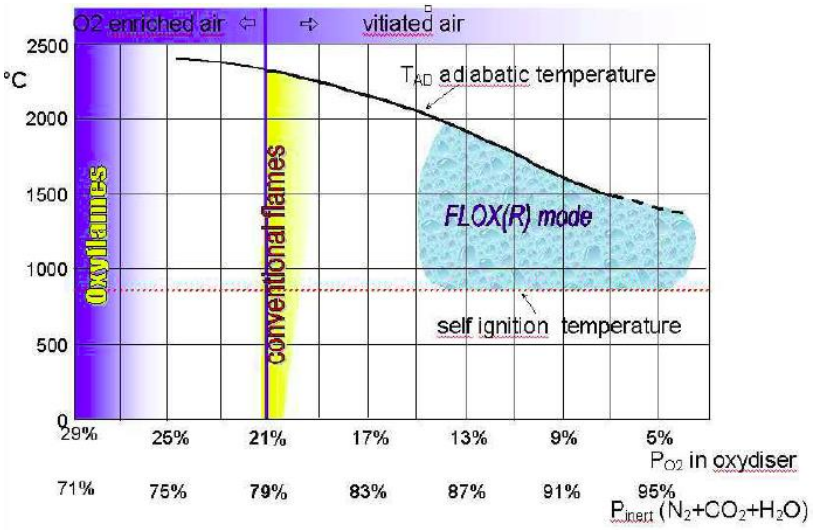

Figure 2.13: Definition of flameless combustion as a function of the preheating temperature of the air and the rate of oxygen [70].

Historically, this combustion regime has been discovered in Japan by Tokyo Gas [74], and almost simultaneously also in many other countries in Europe and the United States. The preheating temperature of the air has been considered as an essential element to achieve this regime, it must exceed 1000°C, even 1300°C (Fig. 2.13) for certain applications[75]. Depending on the country and the authors, this combustion mode has been named and defined differently depending on the approach considered.

Originally, this regime, which appeared with the need to recover energy from the fumes by preheating the air, was associated with the Excess Enthalpy Combustion (EEC) concept developed by Weinberg [76]. More specifically, the increased performance of regenerative systems has led to the names HiTAC (for High-Temperature Air combustion), HPAC (for Highly Preheated Air Combustion), or HiCOT (for High-temperature air Combustion Technology) to define this combustion regime [77]. This definition is based on the characteristics of the combustion air, the criteria of which are a temperature above the autoignition temperature by the regenerative system and a low concentration of oxygen by mixing the air jet and its environment consisting of burnt gases (Fig. 2.14).

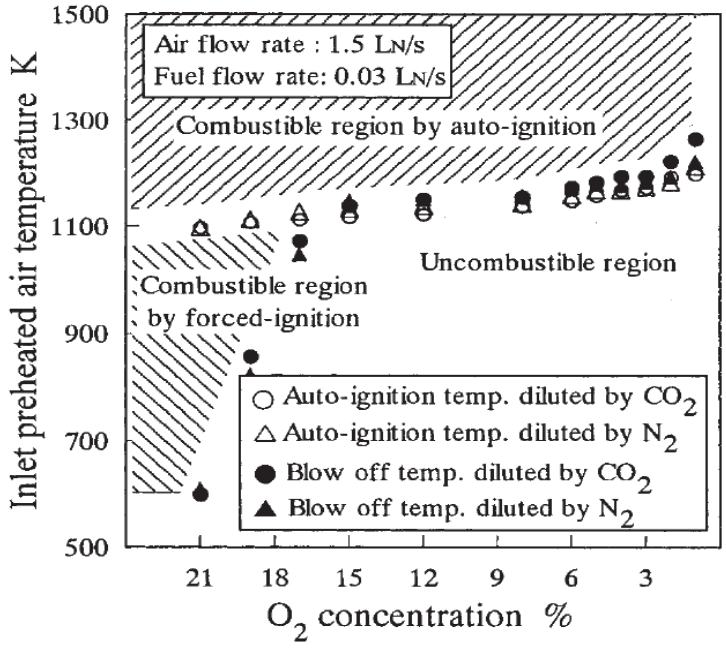

Figure 2.14: Diagram of the existence of the HPAC regime for natural gas in air preheated and diluted with CO_2 or N_2 [78].

Another definition of the flameless combustion regime is based on the need for a high-intensity recirculation zone around the reactive jets in the furnace chamber. Thus, Wünning [35] defines a diagram of the existence of this regime according to the temperature of the furnace and the recirculation rate *Kv* defined as the ratio of mass flows:

$$Kv = \frac{\dot{m}_e}{\dot{m}_f + \dot{m}_a} \qquad (2.5)$$

Where $\dot{m}_e$ Refers to the maximum mass flow rate of recirculated flue gases, $\dot{m}_f$ the mass flow rate of the fuel, and $\dot{m}_a$ that of oxidizing air.

Figure 2.15 shows the stability limits of flameless combustion as a function of recirculation rate and furnace temperature. For low recirculation rates, the flame is stable

regardless of the oven temperature (A), When the recirculation rate increases, the flame may be extinguished if the temperature of the walls is lower than the self-ignition temperature, and it is lifted and unstable above that temperature (B). For very high recirculation rates (higher at 3) and very high temperatures, a very stable dilute combustion regime is reached without a visible flame (C), called 'flameless oxidation' by Wünning [73]. Then retained by them as the trade name FLOX (for "Flameless Oxidation") for their regenerative burners.

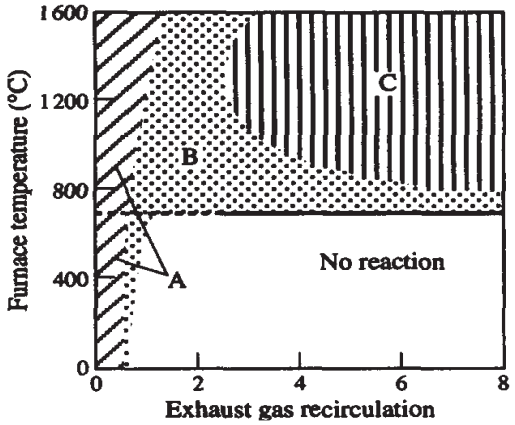

Figure 2.15: Diagram of the existence of flame combustion as a function of the recirculation rate and the temperature of the furnace [79].

Other definitions and denominations of this flameless combustion regime have been proposed by Cavaliere & De Joannon, assimilating it, due to its homogeneous and uniform appearance, to a perfectly stirred reactor made up of fuel, oxidizer, and hot combustion products [80]. The flameless combustion regime is then characterized by a high initial temperature (greater than the auto-ignition temperature) and a final combustion temperature, which remains moderate due to the presence of inert combustion products; the temperature gradient then remains below the auto-ignition temperature (Fig. 2.16).

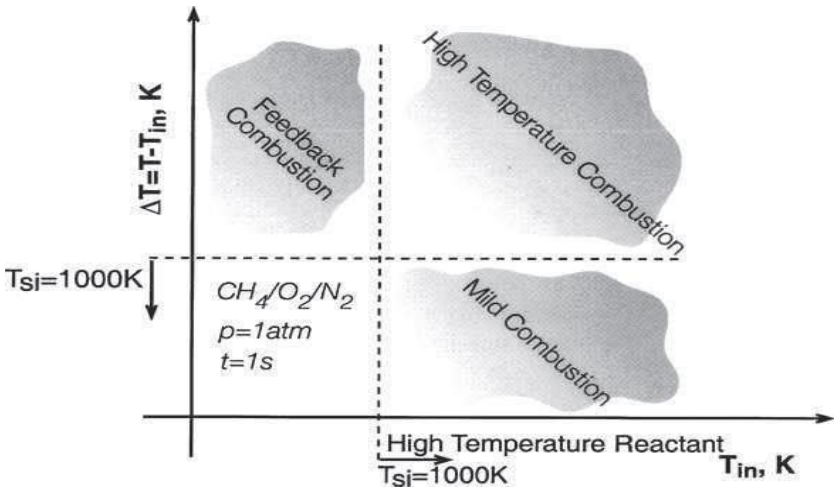

Figure 2.16: Definition of flameless combustion as a function of the inlet temperature of the reactants and the temperature gradient [80].

The name 'MILD combustion' proposed by Cavaliere & De Joannon [80] corresponds both to the acronym 'Moderate or Intense Low-oxygen Dilution' and to the low thermal gradient induced under these conditions and retained as the criterion of this combustion regime by these authors. From a conceptual point of view, De Joannon & Cavaliere also propose other configurations for which the "mild combustion" regime can also be reached [81]. This is the case for example with HCCI engines (for Homogeneous Charge Compression Ignition) where the charge is homogeneous and lean. The high initial temperature is reached by compression in the cylinder then causing the self-ignition of the homogeneous mixture diluted by the EGR and the strong excess of air. These same conditions are also obtained in a reactor supplied by a permanent flow consisting of a fuel - oxidizer - combustion products premix at a temperature above the auto-ignition temperature. In this configuration, called HFFI (for 'Homogeneous Flow Flowing Ignition') by De Joannon & Cavaliere, combustion occurs in the reactor after the auto-ignition delay. Finally, these same criteria for the mild combustion regime can also be achieved in fundamental configurations not initially premixed, such as between a flow of fuel and a flow of counter-current oxidizer. In this case, called HDDI (for 'Hot Diluted Diffusion Ignition'), preheating and dilution can be considered together or separately for each of the two reactants leading then to four basic fundamental configurations. Whatever the configuration, it is possible to find the same criteria for achieving the 'mild combustion' regime: an initial high temperature, in these cases for one of the two reagents, and a maximum temperature gradient that remains moderate. However, the values of these criteria vary depending on the configuration used for dilution and pre-heating of reagents [38].

These different definitions of the same massively diluted combustion regime at a high temperature called here 'flameless' and 'MILD' combustion, are complementary because they correspond to different approaches. They are based on different characteristics of this particular combustion regime that can be obtained with a regenerative burner in a high-temperature fireplace.

Chapter III

Mathematical approaches for turbulent reacting flows

In this chapter, the theoretical foundations on which this work is based will be set out. The equations governing fluid mechanics and turbulence will be presented first, while the combustion model chosen for this work will be presented second. As a theoretical review of the fundamental concepts of fluid mechanics would be outside the objectives of this work, the conservation equations will be presented here directly. For more details, the reader can consult [82]. The emphasis here will be on the description of the turbulence phenomenon and its interaction with combustion.

3.1. Phenomenon equations

3.1.1. Mass conservation

$$\frac{\partial \rho}{\partial t} + \frac{\partial (\rho u_i)}{\partial x_i} = 0 \tag{3.1}$$

3.1.2. Momentum equation

$$\frac{\partial (\rho u_j)}{\partial t} + \frac{\partial (\rho u_i u_j)}{\partial x_i} + \frac{\partial p}{\partial x_j} = \rho g_j + \frac{\partial \tau_{ij}}{\partial x_i} \tag{3.2}$$

3.1.3 Species conservation equations

$$\frac{\partial (\rho Y_k)}{\partial t} + \frac{\partial (\rho u_i Y_k)}{\partial x_i} = \frac{\partial (V_{k,i} Y_k)}{\partial x_i} + \dot{\omega}_k \tag{3.3}$$

3.1.4. Energy conservation equation

$$\frac{\partial (\rho h_s)}{\partial t} + \frac{\partial (\rho u_i h_s)}{\partial x_i} = \left(\frac{\partial \rho}{\partial t} + u_i \frac{\partial \rho}{\partial x_i}\right) + \frac{\partial}{\partial t}\left(\lambda \frac{\partial T}{\partial x_i}\right) - \frac{\partial}{\partial x_i}\left(\rho \sum_{k=1}^{N} V_{k,i} Y_k h_{s,k}\right) + \tau_{ij} \frac{\partial u_i}{\partial x_j} + \dot{\omega}_T + \dot{Q}_{rad} \tag{3.4}$$

With:

$$\tau_{ij} = \left[\mu\left(\frac{\partial u_j}{\partial x_i} + \frac{\partial u_i}{\partial x_j}\right) - \frac{2}{3}\mu\left(\frac{\partial u_k}{\partial x_k}\right)\delta_{ij}\right] \tag{3.5}$$

Where:

- ρ: density
- t: time
- u_j ,u_i ,u_k : flow velocity component in direction i, j, and k
- x_i, x_j, x_k: direction of flow along axes i, j and k
- i,j,k: individual components of the flow which may vary from 1 to 3, representing the X, Y, and Z axes respectively

- p: pressure
- g: gravity
- μ: dynamic viscosity
- Y_k: mass fraction of species k
- $\dot{\omega}_k$: Reaction rate of species k
- $V_{k,i}Y_k$: Diffusive laminar flux of the species Y_k
- h_s: total enthalpy
- $\dot{\omega}_T$: Heat source term due to combustion
- λ : Coefficient of thermal diffusivity
- $V_{k,i}Y_k, h_{s,k}$: Diffusive laminar flow of total enthalpy of the species Y_k
- δ_{ij}: Kronecker Delta
- $\dot{Q}_{rad}$: Radiative heat loss

3.2. Turbulence modeling

Turbulence was defined as: "*Turbulent fluid motion is an irregular condition of flow in which the various quantities show a random variation with time and space coordinates so that statistically distinct average values can be discerned* "[83].

Figure 3.1 shows how turbulence can be interpreted based on average velocity plus some variation [84], This velocity decomposition ($u = \bar{u} + u'$) is also called Reynolds decomposition and allows the use of statistical tools to describe flow. Using this concept and based on the definition of an average value (ϕ being any variable and $\bar{\phi}$ its average value) is defined as follows:

$$\bar{\phi} = \frac{1}{\Delta t}\int_{\Delta t} \phi dt \tag{3.6}$$

Where Δt represents a time interval.

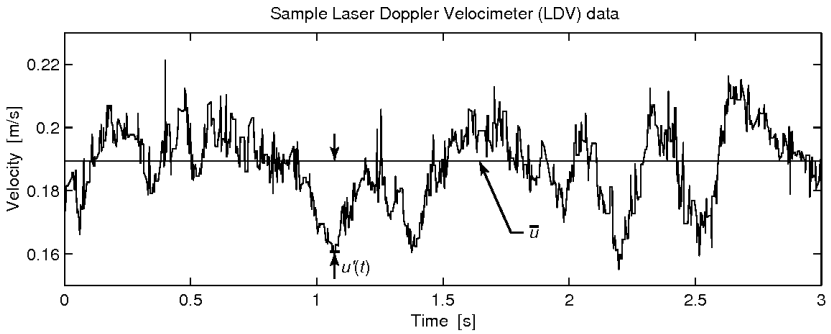

Figure 3.1: Schematic measurement of the turbulent fluctuating velocity at a point showing the average velocity, u, and the fluctuating component [84].

For density variable or compressible flows, the concept of the density-weighted average was introduced [85]. According to a variable, to eliminate the density fluctuations in conservation equations (3.1) to (3.4), the weighted general variable ϕ is obtained from:

$$\phi = \frac{1}{\bar{\rho}} \lim_{t\to\infty} \int_0^t \rho(x,t)\phi(x,t)dt \tag{3.7}$$

Where $\bar{\rho}$ is the density average.

The Favre decomposition is now defined as:

$$\phi = \tilde{\phi} + \phi^{"} \tag{3.8}$$

Where $\tilde{\phi}$ is the density-weighted average of any variable ϕ, $\phi^{"}$ is the fluctuation of this same variable.

Using the Favre averaging presented in (3.7), the conservation equations become [82]:

Mass conservation equation

$$\frac{\partial \bar{\rho}}{\partial t} + \frac{\partial(\bar{\rho}\tilde{u}_i)}{\partial x_i} = 0 \tag{3.9}$$

Momentum equation

$$\frac{\partial(\bar{\rho}\tilde{u}_j)}{\partial t} + \frac{\partial(\bar{\rho}\tilde{u}_i\tilde{u}_j)}{\partial x_i} + \frac{\partial \bar{p}}{\partial x_i} = \frac{\partial}{\partial x_i}\left(\tilde{\tau}_{ij} - \bar{\rho}\widetilde{u_i^{"}u_j^{"}}\right) \tag{3.10}$$

The chemical species conservation equation

$$\frac{\partial(\bar{\rho}\widetilde{Y_k})}{\partial t} + \frac{\partial(\bar{\rho}\widetilde{u_i}\widetilde{Y_k})}{\partial x_i} = \frac{\partial}{\partial x_i}\left(\overline{V_{k,i}Y_k} + \bar{\rho}\widetilde{u_i^{"}Y_k^{"}}\right) + \overline{\dot{\omega}_k} \tag{3.11}$$

Energy conservation equation

$$\frac{\partial(\bar{\rho}h_s)}{\partial t} + \frac{\partial(\bar{\rho}u_i h_s)}{\partial x_i} = \left(\frac{\partial \bar{p}}{\partial t} + u_i\frac{\partial \bar{p}}{\partial x_i} + \overline{u_i^{"}\frac{\partial p}{\partial x_i}}\right) + \frac{\partial}{\partial t}\left(\overline{\lambda\frac{\partial T}{\partial x_i}} - \overline{\rho u_i^{"}h_s^{"}}\right) - \frac{\partial}{\partial x_i}\left(\overline{\rho\sum_{k=1}^{N} V_{k,i}Y_k h_{s,k}}\right) + \overline{\tau_{ij}\frac{\partial u_i}{\partial x_j}} + \overline{\dot{\omega}_T} + \bar{\dot{Q}}_{rad} \tag{3.12}$$

3.3. Modelling of new terms in transport and conservation equations

In the Favre averaging procedure of the equations, new terms appear. These terms are unknown (equations are unclosed), they all should be modeled to resolve phenomenon equations. One of the objectives of the turbulent combustion simulation is to find mathematical closure models and numerical methods to solve equations (3.9) to (3.12).

The main terms to model are:

1. Reynolds stress tensor, $\widetilde{u_i^{"}u_j^{"}}$: This tensor will be closed using the turbulence models which will be presented later,
2. The turbulent flux of species and enthalpy: $\widetilde{u_i^{"}h_s^{"}}$ and $\widetilde{u_i^{"}Y_k^{"}}$: These turbulent fluxes are often solved using a gradient assumption such as:

$$\widetilde{u_i^{"}Y_k^{"}} = -\frac{\mu_t}{Sc_{kt}}\frac{\partial \tilde{Y}_k}{\partial x_i} \quad (3.13)$$

Where Sc_{kt} is the turbulent Schmidt number of species k

3. Diffusion flux of species $\overline{V_{k,i}Y_k}$:

$$\overline{V_{k,i}Y_k} = -\bar{\rho}\overline{D_k}\frac{\partial \tilde{Y}_k}{\partial x_i} \quad (3.14)$$

Where: $\overline{D_k}$, is an average molecular diffusion coefficient of species *k*

4. The pressure-velocity correlation $\overline{u_i^{"}\frac{\partial p}{\partial x_i}}$: In most RANS codes, this term is neglected [82]
5. Production rate of chemical species$\overline{\dot{\omega}_k}$. This term represents one of the fundamental objectives of combustion modeling. In the context of this work, it will be modeled using a suitable turbulent combustion model.
6. The term of heat production from combustion $\overline{\dot{\omega}_T}$ is generally linked to the consumption rate of the fuel or oxidizer which has to be approximated by an adequate turbulent combustion model.
7. The radiation term $\bar{\dot{Q}}_{rad}$ is to be modeled.

3.4. Turbulent kinetic viscosity models for the Reynolds stress tensor

The concept of turbulent dynamic viscosity, μ_t was introduced from the notion of isotopy of the flow [86]. For a Newtonian fluid in laminar regime, the tensor τ_{ij} is defined as [82]:

$$\tau_{ij} = \mu\left(\frac{\partial u_i}{\partial x_j} + \frac{\partial u_j}{\partial x_i}\right) - \frac{2}{3}\mu\left(\frac{\partial u_k}{\partial x_k}\right)\delta_{ij} \quad (3.15)$$

By analogy with (3.15), the Reynolds stress tensor can be modeled by:

$$-\rho\overline{u_i^{"}u_j^{"}} = \mu_t\left(\frac{\partial \overline{u_i}}{\partial x_j} + \frac{\partial \overline{u_j}}{\partial x_i}\right) - \frac{2}{3}\mu_t\left(\frac{\partial \overline{u_k}}{\partial x_k}\right)\delta_{ij} - \frac{2}{3}\rho k\delta_{ij} \quad (3.16)$$

With the turbulent kinetic energy *k* defined as

$$k = \frac{1}{2}\left(\overline{u_i'^2} + \overline{u_j'^2} + \overline{u_k'^2}\right) \quad (3.17)$$

3.4.1. The *k-ε* (standard) turbulence model.

The *k-ε* model assumes that the Reynolds stress tensor is proportional to the mean velocity gradient, using turbulent viscosity (μ_t) as the proportionality constant (equation 3.16). This assumption is known as the Boussinesq hypothesis. To be able to calculate the Reynolds

stress tensor, an additional equation must be provided for μ_t. Using the k-ε model, μ_t is defined according to [87] by:

$$\mu_t = \rho C_\mu \frac{k^2}{\varepsilon} \tag{3.18}$$

Where C_μ = 0.09 is an empirical constant of proportionality and ε = dissipation of kinetic turbulence energy.

The values of k and ε in eq. (3.18) are obtained from the transport equations for k and ε. In index notation, these equations are [88] turbulence energy equation :

$$\rho \frac{\partial k}{\partial t} + \rho \frac{\partial}{\partial x_j}(\overline{u_j} k) = \frac{\partial}{\partial x_j}\left(\left(\mu + \frac{\mu_t}{\sigma_\kappa}\right)\frac{\partial k}{\partial x_j}\right) + P_k - \rho\varepsilon \tag{3.19}$$

Where: P_k is the production of kinetic energy given by:

$$P_k = \mu_t \left(\frac{\partial \overline{u_i}}{\partial x_j} + \frac{\partial \overline{u_j}}{\partial x_i}\right)\frac{\partial \overline{u_i}}{\partial x_j} \tag{3.20}$$

The turbulence energy dissipation equation writes:

$$\rho \frac{\partial \varepsilon}{\partial t} + \rho \frac{\partial}{\partial x_j}(\overline{u_j}\varepsilon) = \frac{\partial}{\partial x_j}\left(\left(\mu + \frac{\mu_t}{\sigma_\varepsilon}\right)\frac{\partial \varepsilon}{\partial x_j}\right) + \frac{\varepsilon}{k}(C_{\varepsilon 1} P_k - C_{\varepsilon 2}\rho\varepsilon) \tag{3.21}$$

Where $C_{\varepsilon 1}$, $C_{\varepsilon 2}$ are empirical constants, σ_k and σ_ε = empirical constants physically representing the Prandtl numbers governing the turbulent diffusion of k and ε.

3.4.2. The realizable k-ε model

The realizable model [89] satisfies certain mathematical constraints on the Reynolds stresses, consistent with the physics of turbulent flows, namely $\frac{k}{\varepsilon}\frac{\partial u}{\partial x} > \frac{1}{3C_\mu} \approx 3.7$. It is different from the standard model in two significant ways:

- It has an alternative formulation for the turbulent viscosity.
- The dissipation rate, ε, transport equation has been derived from an exact equation for the transport of the mean-square vorticity fluctuation.

  Equations of this model are given by:

$$\rho \frac{\partial k}{\partial t} + \rho \frac{\partial}{\partial x_j}(\overline{u_j} k) = \frac{\partial}{\partial x_j}\left(\left(\mu + \frac{\mu_t}{\sigma_\kappa}\right)\frac{\partial k}{\partial x_j}\right) + P_k - \rho\varepsilon \tag{3.22}$$

$$\rho \frac{\partial \varepsilon}{\partial t} + \rho \frac{\partial}{\partial x_j}(\overline{u_j}\varepsilon) = \frac{\partial}{\partial x_j}\left(\left(\mu + \frac{\mu_t}{\sigma_\varepsilon}\right)\frac{\partial \varepsilon}{\partial x_j}\right) + \rho C_{1\varepsilon} S\varepsilon - \rho C_2 \frac{\varepsilon^2}{k + \sqrt{\nu\varepsilon}} \tag{3.23}$$

Where $C_1 = \max\left[0.43, \frac{\eta}{\eta+5}\right]$, $\eta = S\frac{k}{\varepsilon}$, $S = \sqrt{2S_{ij}S_{ij}}$, and $S_{ij} = \frac{1}{2}\left(\frac{\partial \overline{u_i}}{\partial x_j} + \frac{\partial \overline{u_j}}{\partial x_i}\right)$.

The limitation of the realizable model is that it produces non-physical turbulent viscosities in situations when the computational domain contains both rotating and stationary fluid zones (for example, multiple reference frames, rotating sliding meshes).

$$C_{1\varepsilon} = 1.44, C_2 = 1.9, \sigma_\kappa = 1.0, \text{and } \sigma_\varepsilon = 1.2.$$

3.4.3. The RNG k-ε model

This model is a refined version of the standard model, it was developed by the hint of the statistical technique called renormalization group theory. The RNG k-ε model has many enhancements namely: more accurate in rapidly strained flows includes swirl effect on turbulence which enables computation of swirling flows, provides an analytical formula for turbulent Prandtl numbers, and provides a differential formula for effective viscosity that accounts for low-Reynolds number effects. More details on the RNG theory and its application to turbulence can be found in [90].

3.4.3.1. Transport Equations for the RNG k-ε Model

Equations form for this model is similar to the standard k-ε Model, the equations are given by:

$$\rho\frac{\partial k}{\partial t} + \rho\frac{\partial}{\partial x_j}\left(\overline{u_j}k\right) = \frac{\partial}{\partial x_j}\left(\alpha_k \mu_{eff}\frac{\partial k}{\partial x_j}\right) + P_k - \rho\varepsilon \tag{3.24}$$

$$\rho\frac{\partial \varepsilon}{\partial t} + \rho\frac{\partial}{\partial x_j}\left(\overline{u_j}\varepsilon\right) = \frac{\partial}{\partial x_j}\left(\alpha_\varepsilon \mu_{eff}\frac{\partial \varepsilon}{\partial x_j}\right) + \frac{\varepsilon}{k}\left(C_{\varepsilon 1}P_k - C^*_{\varepsilon 2}\rho\varepsilon\right) \tag{3.25}$$

The quantities α_k and α_ε are the inverse effective Prandtl numbers for k and ε, respectively. In this model the effective turbulent viscosity is computed from the differential equation:

$$d\left(\frac{\rho^2 k}{\sqrt{\varepsilon\mu}}\right) = 1.72\frac{\left(\frac{\mu_{eff}}{\mu}\right)}{\sqrt{\left(\frac{\mu_{eff}}{\mu}\right)^3 - 1 + C_v}}\, d\left(\frac{\mu_{eff}}{\mu}\right) \tag{3.26}$$

C_v is a constant equal to 100.

The equation (3.24) is integrated to give μ_{eff} allowing the model to give a better approximation for low Reynolds numbers and near walls. For high Reynolds number limit, the equation (3.24) gives $\mu_t = \rho C_\mu \frac{k^2}{\varepsilon}$ with $C_\mu = 0.0845$ derived using RNG theory which is very close to the empirically derived $C_\mu = 0.09$ in the standard $k - \varepsilon$ model.

In the case of the swirling of the mean flow, the turbulent viscosity in the RNG model is modified to include the swirling effect. The modification is operated by:

$$\mu_t = \mu_{t0} f\left(\alpha_s, \Omega, \frac{k}{\varepsilon}\right) \tag{3.27}$$

where μ_{t0} is the value of turbulent viscosity without the swirl modification, Ω is a characteristic swirl number and α_s is a swirl constant that took different values dependent on swirl strength.

In the RNG model, the inverse effective Prandtl numbers for *k* and *ε,* α_k and α_ε are calculated by:

$$\left|\frac{\alpha-1.3929}{\alpha_0-1.3929}\right|^{0.6321}\left|\frac{\alpha+2.3929}{\alpha_0+2.3929}\right|^{0.3679} = \frac{\mu_{mol}}{\mu_{eff}} \tag{3.28}$$

Where: $\alpha_0 = 1$. In the high-Reynolds number limit ($\frac{\mu_{mol}}{\mu_{eff}} \ll 1$), $\alpha_k = \alpha_\varepsilon \approx 1.393$.

In eq. (3.23), $C_{\varepsilon 2}^*$ is different from that of *k-ε* model, it is given by:

$$C_{\varepsilon 2}^* = C_{\varepsilon 2} + \frac{C_\mu \eta^3 \left(1-\frac{\eta}{\eta_0}\right)}{1+\beta\eta^3} \tag{3.29}$$

Where: $= \frac{k}{\varepsilon}$, $\eta_0 = 4.38$, $\beta = 0.012$, $S = \sqrt{2S_{ij}S_{ij}}$, and $S_{ij} = \frac{1}{2}\left(\frac{\partial \overline{u_i}}{\partial x_j} + \frac{\partial \overline{u_j}}{\partial x_i}\right)$

The model constants are derived analytically and have the values $C_{\varepsilon 1} = 1.42$ and $C_{\varepsilon 2}^* = 2.0$.

3.4.4. The k-ω Model

Very similar to the *k-ε* model, the *k-ω* model was developed [87] to improve viscosity treatment near the wall [91]. Omega (*ω*) can be defined as the specific dissipation rate, or more simply, *ε/k*. With the *k-ω* model the turbulent viscosity is now defined:

$$\mu_t = \alpha^* \frac{\rho k}{\omega} \tag{3.30}$$

Where:

$$\alpha^* = \alpha_\infty^* \left(\frac{\alpha_0^* + Re_t/R_k}{1+Re_t/R_k}\right) \tag{3.31}$$

With:

$$Re_t = \frac{\rho k}{\mu \omega} \tag{3.32}$$

With: $R_k = 6$, $\alpha_0^* = 0.024$, $\alpha_\infty^* = 1$

Similarly to the *k*-*ε* model, *k*-*ω* has two transport equations for *k* and *ω* which write [88]:

$$\rho \frac{\partial k}{\partial t} + \rho \frac{\partial}{\partial x_j}\left(\overline{u_j} k\right) = P_k + \left(\mu + \frac{\mu_t}{\sigma_k}\right) \frac{\partial^2 k}{\partial {x_j}^2} - \beta' \rho k \omega \tag{3.33}$$

$$\rho \frac{\partial \omega}{\partial t} + \rho \frac{\partial}{\partial x_j}\left(\overline{u_j} \omega\right) = P_k + \left(\mu + \frac{\mu_t}{\sigma_\omega}\right) \frac{\partial^2 k}{\partial {x_j}^2} + \alpha \frac{\omega}{k} P_k - \beta' \rho \omega^2 \tag{3.34}$$

With : β' = 0.09, α = 5/9 and $\sigma_\omega = \sigma_k$= 2.

3.4.5. The SST *k*-*ω* Model

The SST (Shear-Stress Transport) *k*-*ω* model [92] presents a hybrid model between *k*-*ε* and *k*-*ω*. Indeed, this model is more versatile, as it takes the formulation of *k*-*ω* to near the walls (where *k*-*ω*) is most accurate) and uses *k*-*ε* in the free-flow regions. It then combines the advantage of good predictions near walls, while maintaining the performance of the *k*-*ε* model in terms of the good representation of inverse pressure gradients. Using this model, the turbulent transport is obtained by a term limiting the turbulent viscosity [88].

$$\mu_t = \rho \left(\frac{\alpha k}{max(\alpha \omega, SF_2)}\right) \tag{3.35}$$

$$F_2 = tanh\left[\left(max\left(\frac{2\sqrt{k}}{\beta' \omega y}, \frac{500\mu}{y^2 \omega}\right)\right)\right] \tag{3.36}$$

Where S is the local strain rate and *y* is the distance from the nearest wall.

3.4.6. Reynolds Stress tensor transport Model (RSM)

The turbulence models presented so far assume that the local state of turbulence can be characterized by time and length scales. In addition, the components of the Reynolds stress tensor can be proportional with these same scales. To develop models allowing a better representation of the various turbulence scales present in a complex flow, transport equations have been developed to describe the components of the Reynolds stress tensor individually. The advantage of models calculating turbulent transport is that they can be used in non-isotropic turbulence since they didn't use the Boussinesq hypothesis directly. Using Favre's mean, as presented in section 3.1, the Reynolds stress transport equation for a variable density flow then writes as follows [93],[94], [95]:

$$\bar{\rho}\frac{D\widetilde{u_i^{"}u_j^{"}}}{Dt} = \underbrace{-\bar{\rho}\widetilde{u_i^{"}u_k^{"}}\frac{\partial\tilde{U}_j}{\partial x_k} - \bar{\rho}\widetilde{u_j^{"}u_k^{"}}\frac{\partial\tilde{U}_i}{\partial x_k}}_{(\boldsymbol{I})\ Reynolds\ stress\ production}$$

$$\underbrace{-\left[u_i^{"}\overline{\frac{\partial p}{\partial x_j}} + u_i^{"}\overline{\frac{\partial p}{\partial x_j}} - \frac{2}{3}\delta_{ij}u_k^{"}\overline{\frac{\partial p}{\partial x_j}}\right]}_{(\boldsymbol{II})\ Pressure\ deformation\ correlation}$$

$$\underbrace{-2\mu\overline{\frac{\partial u_i'}{\partial x_k}\frac{\partial u_j'}{\partial x_k}}}_{(\boldsymbol{III})\ Viscous\ dissipation} \tag{3.37}$$

$$\underbrace{-\frac{\partial}{\partial x_k}\left[\bar{\rho}\widetilde{u_i^{"}u_j^{"}u_k^{"}} + \frac{2}{3}\delta_{ij}\overline{u_k^{"}p}\right]}_{(\boldsymbol{IV})\ Turbulent\ diffusion\ flux}$$

$$\underbrace{-\overline{u_i^{"}\frac{\partial p}{\partial x_j}} - \overline{u_j^{"}\frac{\partial p}{\partial x_i}}}_{(\boldsymbol{V})\ Mean\ pressure\ gradient}$$

$$+ \underbrace{\frac{2}{3}\delta_{ij}p\overline{\frac{\partial u_k^{"}}{\partial x_k}}}_{(\boldsymbol{VI})\ Strain\ tensor\ fluctuation}$$

The terms (II) to (IV) in eq. (3.37) have to be modeled, the viscous dissipation, the term (III) of (3.37) is modeled according to the Kolmogorov hypothesis which assumes local isotropy of the smallest turbulence scales, where the viscous dissipation is the most significant. The dissipation model is then defined as:

$$\varepsilon_{ij} = \frac{2}{3}\varepsilon\delta_{ij} \tag{3.38}$$

Where the calculation of energy dissipation rate ε is calculated according to the following transport equation [96]:

$$\bar{\rho}\frac{D\varepsilon}{Dt} = C_\varepsilon\frac{\partial}{\partial x_k}\left[\bar{\rho}\frac{k}{\varepsilon}\widetilde{u_k^{"}u_i^{"}}\frac{\partial\varepsilon}{\partial x_i}\right] + C_{\varepsilon 1}\bar{\rho}\frac{\varepsilon}{\kappa}P_k - C_{\varepsilon 2}\bar{\rho}\frac{\varepsilon^2}{k} \tag{3.39}$$

With the production of turbulent kinetic energy defined as:

$$P_k = -u_i^{"}u_j^{"}\frac{\partial\widetilde{u_i}}{\partial x_j} \tag{3.40}$$

The turbulent diffusive flux, term (IV) of (3.37), is described using an approximation of the transport gradient from Dally and Harlow (1970):

$$\widetilde{u_i^{"}u_j^{"}u_k^{"}} = -C_s\frac{2}{3}\widetilde{u_k^{"}u_l^{"}}\frac{\partial\widetilde{u_i^{"}u_j^{"}}}{\partial x} \tag{3.41}$$

Where Cs is an empirical constant equal to 0.22.

Pressure-deformation correlation in eq. (3.37) is the key term for which most modeling work has been done up to this date [97]. During its modeling, the correlation is generally represented in two parts (a slow and a fast), more details on the modeling of this term can be found in [96], [98], [91], [99], and [97].

3.5. Turbulent non-premixed combustion

In many industrial applications (industrial furnace, aeronautical/industrial gas turbine, diesel engine, etc.), fuel and oxidant enter the combustion chamber separately. To facilitate control or safety, fuel and oxidizer mix (diffuse) into each other before igniting. This process is called non-premixed combustion (NPC). NPC is characterized by the diffusion of fuel and oxidant, as it is this phenomenon that controls the rate of reaction.

When time scales are compared, the physical time of the diffusive mixing process is much greater than that of the chemical reaction time. It is therefore realistic to say that this combustion is characterized by infinitely fast chemistry. This hypothesis simplifies the chemical process by eliminating the parameters associated with conventional reaction mechanisms. However, in some situations, turbulence (mixing) and chemical reaction time scales may become similar locally. In these cases, the hypothesis of infinitely fast chemistry no longer holds and instability effects (local quenching and extinctions) must be taken into account [100].

3.5.1. RANS modeling of turbulent non-premixed combustion

This section of the literature review presents the approach that is used to model non-premixed reactive flow by the RANS averaged equations. First, some used fundamental concepts relative to combustion are introduced.

3.5.1.1. Stoichiometry and species conservation equations

Stoichiometry, noted by a subscript (*st*) represents an ideal state of chemical transformation in which all fuel is transformed into a combustion product. Equation (3.51) is the generic chemical equation for the combustion of a hydrocarbon in pure oxygen.

$$\nu'_f C_m H_n + \nu'_{O_2} O_2 \rightarrow \nu''_{CO_2} CO_2 + \nu''_{H_2O} H_2O \tag{3.42}$$

$\nu'_f, \nu'_{O_2}, \nu''_{CO_2}, \nu''_{H_2O}$: are the stoichiometric coefficients of the balanced chemical equation.

The stoichiometric coefficient of combustion in pure oxygen can now be defined as:

$$S_{O_2} = \frac{\nu'_{O_2} w_{O2}}{\nu'_F w_f} \tag{3.43}$$

Where: w_x = molecular weight of each species.

As in most practical applications combustion is not carried out in pure oxygen but rather in the air, S_{O2} must be modified taking into account the other non-reactive components of the air. Thus, as the air is only composed of 23.2% mass fraction of O_2, the remainder being nitrogen not entering into reaction, S in the air becomes:

$$S_{air} = \frac{S_{O_2}}{0.232} \tag{3.44}$$

The eq. (3.11) can be written for each species *k (k stands for C_mH_n, O_2,...)* is eq. (3.51), the general species equation writes:

$$\frac{\partial(\rho Y_k)}{\partial t} + \frac{\partial(\rho u_i Y_k)}{\partial x_i} = \frac{\partial}{\partial x_i}(\rho\, D_K \frac{\partial Y_k}{\partial x_i}) + \dot{\omega}_k \tag{3.45}$$

Where D_k is the molecular diffusion coefficient of species *k* determined according to Fick's law, and $\dot{\omega}_k$ is the production rate of species *k*.

3.5.1.2. Passive scalar

Burke and Schumann [101] were pioneers of non-premixed combustion. They introduced at that time a scalar called the *Z* mixture fraction, independent of the combustion process. The passive scalar *Z* can be defined as [82]:

$$Z = \frac{sY_f - Y_O + Y_O^0}{sY_f^0 + Y_O^0} \tag{3.46}$$

With: Y_f and Y_O : mass fraction of fuel and oxidant.

Y_x^0 : Mass fraction of fuel and oxidant in their respective jet, if they are not pure.

Y_O^0: 0.232 (mass fraction of oxygen in the air).

This scalar combines algebraically conservation equations of different species to obtain a source-free equation for the scalar *Z* (eq. 3.54). Thus, *Z* is qualified as passive since it does not intervene in chemical reactions. Its value varies only due to the diffusion and convection phenomena present in the flow. Moreover, *Z* can be normalized by its values at the oxidizer and fuel to have *1* at the fuel side and *0* at the oxidizer one.

The assumptions in defining such a conserved scalar are [82]:

- Molecular diffusion (D_k) follows Fick's law and is equal for each species.
- The specific heat (C_p) of each species is equal and constant.
- The Lewis number (thermal diffusion/molecular diffusion) is unity.

- The fuel and the oxidant are introduced separately into the field and with their respective temperature and concentration.

3.5.2. Flamelet turbulent combustion model

3.5.2.1. Steady laminar flamelet concept

This concept is related to laminar counterflow diffusion (Figure) flame where equations can be transformed from physical space (with *x* as the independent variable) to mixture fraction space (with *Z* as the independent variable) [102]. To better understand this change of variable proposed by [103] . Figure 3.2 shows a diffusion flame element, the change of variable consists in changing the system of physical coordinates (x_1, x_2, x_3) to that of Z = f (y_2, y_3). As the gradients of *Z* in the y_2 and y_3 directions are negligible compared to the normal plane [82], the structure of the flame element then becomes one-dimensional in *Z* direction. The directions y_2 and y_3 could here be interpreted physically like the deformation (or curvature) of the flame element along with two perpendicular directions of the same plane.

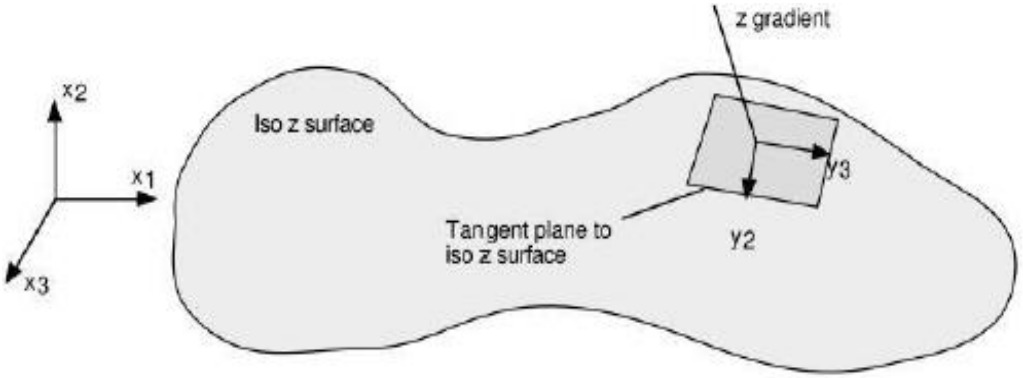

Figure 3.2: Variable change for diffusion flame sheets [82].

Since real combustion applications are multidimensional and turbulent reactive fields, certain assumptions must be respected to be able to use this flame element (flamelet) in a turbulent field. Indeed, in terms of comparative dimensional analysis, this element must be considered as much lower than the scales of turbulence and deformation present in the flow. As illustrated in Figure 3.3, when these criteria are met, the turbulent flames can then be modeled as a set of small laminar flames (flamelet), stamping in the turbulent field. T_F, and Y_O, correspond respectively to the temperatures and mass fractions of fuel and oxidant before they mix.

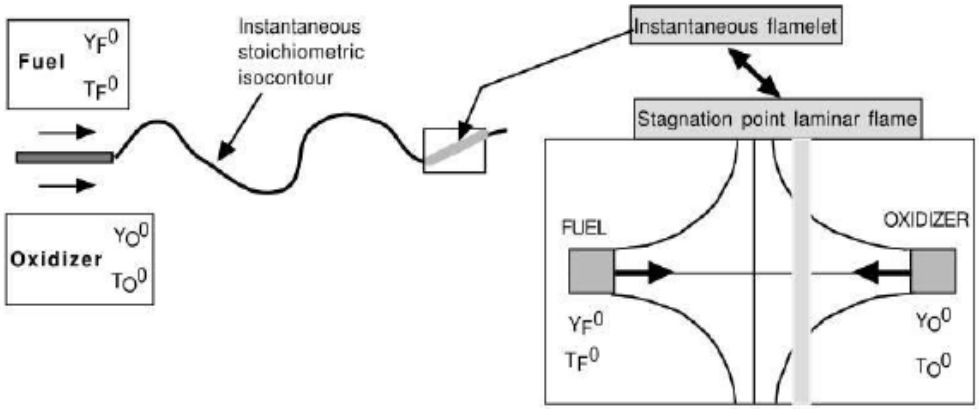

Figure 3.3: Flamelet concept for turbulent non-premixed flames [82].

With this change of variable from physical space to the space of Z, it is now possible to describe the temperatures and the mass fraction according to:

$$T = f(Z) \tag{3.47}$$

$$Y_k = f(Z) \tag{3.48}$$

By applying the change in the variable of Z to equations (3.3), and (3.4), and neglecting the convection terms, because all considered scalars are transported with the same velocity in the physical dimension consequently there is then no relative convection velocity between Z and the other scalars such as temperature and mass fractions of species, the species conservation equation then becomes:

$$\dot{\omega}_k = -\rho D \left(\frac{\partial Z}{\partial x_i}\frac{\partial Z}{\partial x_i}\right)\frac{\partial^2 Y_k}{\partial z^2} = -\frac{1}{2}\rho\chi\frac{\partial^2 Y_k}{\partial z^2} \tag{3.49}$$

The energy equation, in terms of temperature, gives:

$$\dot{\omega}_T = -\frac{1}{2}\rho\chi\frac{\partial^2 T}{\partial z^2} \tag{3.50}$$

Where $\chi = 2D\left(\frac{\partial Z}{\partial x_j}\right)^2$ is named the dissipation scalar, It often provides the connection between the mixing field and the combustion modeling.

Equations (3.49) and (3.50) are said flamelet equations. If χ is known, the laminar production rate, species, and temperature distribution can be easily found in the function of Z since the problem is one-dimensional. To solve for turbulent quantities, the probability density functions (PDF) are used in conjunction with the laminar variable through the relations [82]:

$$\overline{\dot{\omega}_k} = \int_0^\infty \int_0^1 \dot{\omega}_k\,(Z,\chi_{st})p(Z,\chi_{st})dZd\chi_{st} \tag{3.51}$$

$$\bar{\rho}\widetilde{Y_k} = \int_0^\infty \int_0^1 \rho Y_k\,(Z,\chi_{st})p(Z,\chi_{st})dZd\chi_{st} \tag{3.52}$$

$$\bar{\rho}\tilde{T} = \int_0^{\infty} \int_0^1 \rho T\ (Z, \chi_{st}) p(Z, \chi_{st}) dZ d\chi_{st} \tag{3.53}$$

Where $p(Z, \chi_{st})$ are the joint probability of both variables.

By assuming the statistical independence of the two variables and by using the weighted average of Favre, it is then possible to separate this function according to:

$$\rho p(Z, \chi_{st}) = \bar{\rho}\tilde{p}(Z) p(\chi_{st}) \tag{3.54}$$

The probability density functions (PDF) are then used to evaluate the statistical probabilities of the two variables. The PDF of Z is most of the time calculated according to a presumed β function [82].

$$\tilde{p}(Z) = \big(\beta(a,b)\big)^{-1} (1 - Z)^{b-1} \tag{3.55}$$

With:

$$\beta(a,b) = \int_0^1 z^{a-1} (1 - Z)^{b-1} \tag{3.56}$$

Where:

$$a = \tilde{Z}\left[\frac{\tilde{Z}\,(1-\tilde{Z})}{z^{"}} - 1\right] \tag{3.57}$$

$$b = \frac{a}{\tilde{z}} - a \tag{3.58}$$

For the PDF of the dissipation rate of the stoichiometric passive scalar χ_{st} [104] proposed a log-normal distribution:

$$p(\tilde{\chi}_{st}) = \frac{1}{\chi_{st}\sigma\sqrt{2\pi}} exp\left(\frac{ln\tilde{\chi}_{st} - \nu}{2\sigma^2}\right) \tag{3.59}$$

Where ν is related to the mean value of $\tilde{\chi}_{st}$, according to:

$$\tilde{\chi}_{st} = exp\left(\nu + \frac{\sigma^2}{2}\right) \tag{3.60}$$

In turn, $\tilde{\chi}$ is linked to $\tilde{\chi}_{st}$, according to the theory of deformed laminar flames of constant density:

$$\tilde{\chi} = \tilde{\chi}_{st} \int_0^1 \frac{F(Z)}{F(Zst)} \tilde{p}(Z) dZ \tag{3.61}$$

Where:

$$F(Z) = exp(-2[erf^{-1}(2Z - 1)]^2) \tag{3.62}$$

With: erf : error function generated during the integration of the normal distribution [82].

The computation of the β function, used in the integration to determine turbulent species and temperature, needs the calculation of the mean mixture fraction $\tilde{z}$ and its variance $\widetilde{z''^2}$ through the equations:

Conservation equation of the mean mixture fraction $\tilde{z}$:

$$\frac{\partial(\bar{\rho}\tilde{z})}{\partial t} + \frac{\partial(\bar{\rho}\widetilde{u_\iota}\widetilde{z})}{\partial x_i} = \frac{\partial}{\partial x_i}(\bar{\rho}\,\overline{D\frac{\partial z}{\partial x_\iota}} - \bar{\rho}\,\widetilde{u_\iota'' z''}) \tag{3.63}$$

Conservation equation of the variance $\widetilde{z''^2}$ of z :

$$\frac{\partial(\bar{\rho}\widetilde{z''^2})}{\partial t} + \frac{\partial(\bar{\rho}\widetilde{u_\iota}\widetilde{z''^2})}{\partial x_i} = \frac{\partial}{\partial x_i}\left(\bar{\rho}\,\frac{\lambda}{C_p}\frac{d\widetilde{z''^2}}{\partial x_i}\right) + 2\bar{\rho}\frac{\lambda}{C_p}\left(\frac{\partial\tilde{z}}{\partial x}\right)^2 - \bar{\rho}\tilde{\chi} \tag{3.64}$$

With z fraction of mixture, and $\widetilde{z''^2}$ the variance of z according to Favre's averaging.

2.5.2.2. Flamelet library construction

In simulations, equations (3.60) and (3.61) are solved separately from the rest of the fluid mechanic's code. PDF functions are mostly solved externally and species concentrations, as well as temperatures, are tabulated in an external flamelet library. The turbulent distribution of species, the temperature in function of scalar dissipation rate is stored in a lookup table used by the CFD code to solve the problem. The equations, which govern the construction of this flame library, were presented previously, but they are detailed more explicitly here according to [105]:

$$\rho\frac{\partial T}{\partial t} - \frac{1}{c_p}\frac{\partial p}{\partial t} - \rho\frac{\chi}{2}\frac{\partial^2 T}{\partial Z^2} - \rho\frac{\chi}{2c_p}\frac{\partial T}{\partial Z}\frac{\partial c_p}{\partial Z} - \sum_i^N \rho\frac{\chi}{2Le_i}\frac{c_{pi}}{c_p}\frac{\partial Y_i}{\partial Z}\frac{\partial T}{\partial Z} + \frac{1}{c_p}\sum_i^N \dot{m}_\iota\,\dot{h}_\iota - \frac{\dot{q}R}{c_p} = \frac{\dot{h}_{chem}}{c_p} \tag{3.65}$$

$$\rho\frac{\partial Y_i}{\partial t} - \rho\frac{\chi}{Le_i}\frac{\partial^2 Y_i}{\partial Z^2} = \dot{m}_\iota \tag{3.66}$$

- Where *N* is the number of chemical species
- $\dot{m}_\iota$: Chemical production rate of species *i*
- $\dot{h}_\iota$: Specific enthalpy of species *i*
- *q*: heat loss by radiation
- Le_i : Lewis number of species *i* defined here as:

$$Le_i = \frac{\lambda}{\rho C_p D_i} \tag{3.67}$$

According to [105], the convection terms of (3.71) and (3.72) can be neglected because all considered scalars are transported with the same velocity in the physical dimension. There is then no relative convection velocity between *Z* and the other scalars such as temperature and mass fractions of species. More details on the composition of the flame library will be exposed in the next section.

2.5.2.3. RANS resolution of reactive turbulent flow using flamelet model

The classic approach used by several codes to simulate turbulent reactive flow using the flamelet combustion model is summarized in Figure 3.4. Firstly, the numerical code solves (3.46) to (3.48). The only variables which couple fluid mechanics with combustion are *k* and *ε* used in the modeling χ. When using the flamelet model to simulate reactive flow, the conservation equations (3.47) (3.48) are solved to establish the mixing fractions as well as their respective variations. The species conservation equation (3.46) is not directly solved. And concentrations are established decoupled using the flame library. When using the flame model with CFD, the temperature is resolved according to [88].

$$\rho \frac{\partial T}{\partial t} - \frac{\chi_{st}}{2} \frac{\partial^2 T}{\partial Z^2} = \frac{1}{\rho C_p} \sum_{i=1}^{n} \dot{h}_i \dot{m}_i + \frac{\dot{q}_r}{C_p} + \frac{1}{C_p} \frac{\partial p}{\partial t} \tag{3.68}$$

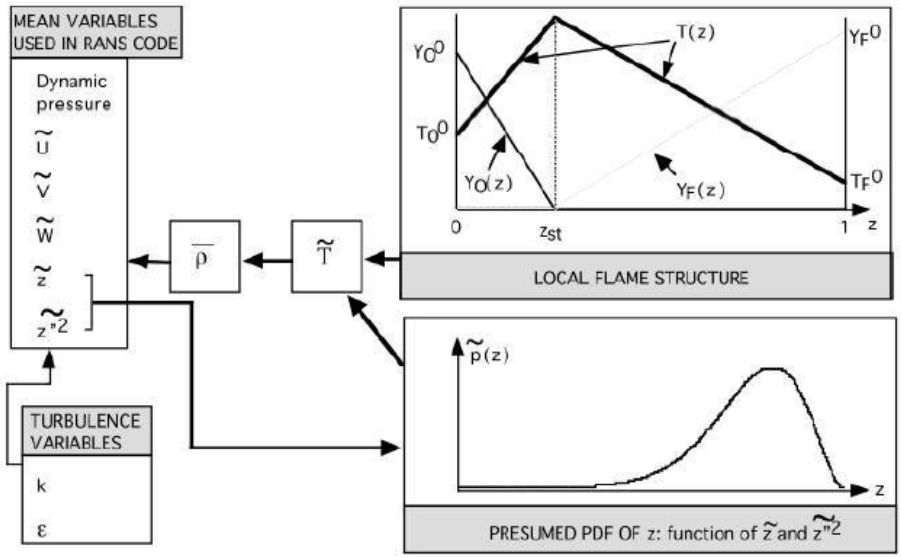

Figure 3.4: Presumed PDF method for infinitely fast irreversible chemistry [82].

3.5.3. The Eddy Break Up (EBU) model

The eddy break-up model [106] is based on the phenomenological analysis of turbulent combustion assuming high Reynolds (*Re>>1*) and Damkohler (*Da>>1*) numbers. The rate of consumption of fuel is specified as a function of local flow properties. The mixing-controlled rate of reaction is expressed in terms of the turbulence time scale *k*/ε, where *k* is the turbulent

kinetic energy and ε is the rate of dissipation of *k*. The reaction rate is the function of the turbulent time scale one ($\tau_{EDM,k} \approx \frac{k}{\varepsilon}$), which, for fuel, oxygen, and products, may be expressed as follows:

$$\widetilde{\dot{\omega}_{fu}} = -C_R \bar{\rho} \tilde{Y}_{fu} \frac{\varepsilon}{k} \tag{3.69}$$

$$\widetilde{\dot{\omega}_{ox}} = -C_R \bar{\rho} \frac{\widetilde{Y_{ox}}}{s} \frac{\varepsilon}{k} \tag{3.70}$$

$$\widetilde{\dot{\omega}_{pr}} = -C_R{}' \bar{\rho} \frac{\tilde{Y}_{pr}}{(1+s)} \frac{\varepsilon}{k} \tag{3.71}$$

The eddy break-up model solves one transport equation for the mass fraction of fuel Y_{fu}. The individual dissipation rates (3.75)–(3.77) of fuel, oxygen, and products are considered, and the model takes the actual reaction rate of fuel to be equal to the slowest of these dissipation rates:

$$\widetilde{\dot{\omega}_{fu}} = \bar{\rho} \frac{\varepsilon}{\kappa} \min \left[C_R \tilde{Y}_{fu}, C_R \frac{\widetilde{Y_{ox}}}{s}, C_R{}' \frac{\tilde{Y}_{pr}}{(1+s)} \right] \tag{3.72}$$

Where C_R and C'_R are model constants

This formulation of the average reaction rate provides good predictions in many practical cases where the infinitely fast chemistry hypothesis is justified. However, EDM fails in flame prediction, where reactions in the area near the burner are kinetically controlled. Therefore, the inclusion of chemical kinetics in the formulation of the average reaction rate becomes necessary. Among the different options, the serial process approach, proposed by Azevedo, was considered in this study. It is based on the assumption that this total reaction time can be represented by the sum of the characteristic time for the turbulent mixing, $\tau_{EDM,k}$, and the characteristic time for the chemical reaction $\tau_{cin,k}$:

$$\tau_{total} = \tau_{EDM,k} + \tau_{cin,k}$$

3.5.4. The Eddy Dissipation Concept (EDC) model

3.5.4.1. Energy cascade model

Figure 3.5 illustrates the mechanical energy transfer model of the mean flow, through turbulence energy, to heat [107]. In Figure 3.5, w 'is the mechanical energy input (work) of the mean flow to the turbulence. For steady-state turbulence, this is the production of kinetic energy from turbulence. The sum of q '+ q "+ ... + qn + ... + q * is the rate of dissipation of the kinetic energy of turbulence (heat), ε. When the amounts of turbulence, such as the energy of turbulence are found from the transport equations, w 'represents the total input of kinetic energy of turbulence.

The first level of the turbulence structure is made up of large, energy-rich eddies. It is characterized by a scale of velocity u '(which is taken equal to $\left(\frac{2}{3}k\right)^{\frac{1}{2}}$, where k is the energy of turbulence) and a scale of length L'. A frequency or rate of stretching can be defined by:

$$\omega' = \frac{u'}{L'} \tag{3.73}$$

These quantities vary in space and time and are determined by the turbulence model, e.g. a k-ε model. This level represents the whole spectrum because it also contains the effect of smaller scales. The next level represents the part of the spectrum where the characteristic frequency is $\omega'' = 2\omega'$, the speed u "and the length L". Similar to the first, this level was supposed to contain the effect of all subsequent levels. Likewise, the nth level was characterized by $\omega_n = 2\omega_{n-1}$, u_n and L_n. In the smallest vortices, ω *, u * and L* are of the same order of magnitude as the Kolmogorov scales.

When transferring from the first to the second level, w", is equal to the sum of the dissipation of all subsequent levels, so the dissipation is ε = q '+ w". The output, which provides mechanical energy at the first level, is the product of turbulence stress and an average strain rate. The second level power supply was modeled by:

$$w'' = C_{D1}\frac{3}{2}u''^2\omega'' = C_{D1}\frac{3}{2}u''^2 2\omega' \tag{3.74}$$

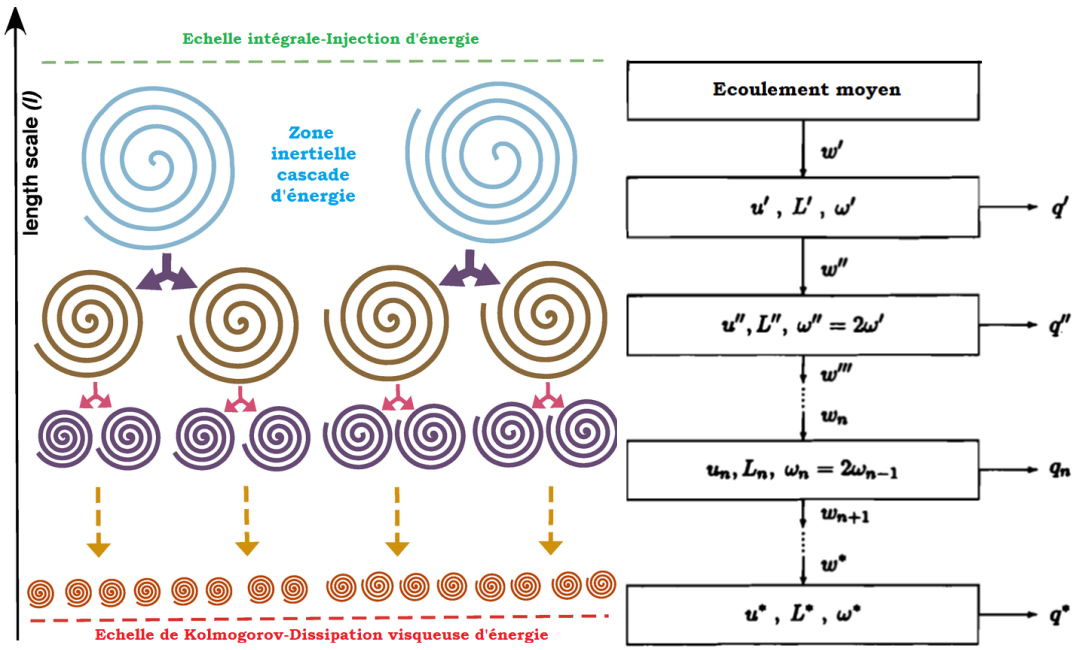

Figure 3.5: Cascade of turbulence energy.

The transfer from the first level to the second is proportional to the square of a characteristic fluctuation at the second level multiplied by the characteristic frequency or by the stretch rate at the first level. This is an analogy with the previous level where the output is proportional to the square of a characteristic fluctuation at the first level, and also proportional to the stretch rate at the mean flow level. In this expression, $2\omega'$can be replaced by ω''. The transfer of mechanical energy to the thermal energy of the first level has been modeled as:

$$q' = C_{D2}\nu\omega'^2 \tag{3.75}$$

It is the direct heat dissipation of the first level. This model is an analogy to the term dissipation in the mechanical energy equation, which is proportional to the viscosity and the square of the stretch rate. Likewise, expressions can be expanded for w "and q", and so on down the waterfall. It was assumed that the transfer from one level to another follows the same pattern for all levels. This gave a set of equations for each level.

For the nth level:

$$w_n = \frac{3}{2}C_{D1}\omega_n u_n^2, \quad q_n = C_{D2}\nu\omega_n^2 \quad \text{et} \quad w_n = q_n + w_{n+1} \tag{3.76}$$

The last step (n = *) are the fine structures, where

$$w^* = \frac{3}{2}C_{D1}\omega^* u^{*2}, \quad q^* = C_{D2}\nu\omega^{*2} \quad \text{et} \quad w^* = q^* \tag{3.77}$$

For simplicity, it was assumed that the numerical coefficients C_{D1} and C_{D2} in the above expressions were the same, and are constant. For high and moderate Reynolds numbers, the dissipation is low at the upper levels of the cascade. In other words, for a small *n*, $q_n$is negligible compared to w_n which is approximately equal to w_{n+1}. So, for n = *2*, u'''^2 is close to $\frac{1}{2}u''^2$. If, in the same way, we assume that $u''^2 \cong \frac{1}{2}u'^2$, then $w'' = C_{D1}\omega'\frac{3}{2}u'^2$. In addition, the turbulence energy,$k = \frac{3}{2}u'^2$, can be introduced. The transfer of mechanical energy from the first level of turbulence can be estimated by $w'' = C_{D1}\omega' k$. In the turbulent combustion model (Magnussen, 1981a, 1989), the cascade model was used with C_{D1}= 0,135 and C_{D2} = 0,5. Since a model is only an approximation, the numerical values of the constants should be the best fit for several types of flows. In a turbulence model, all the constants are more or less related to each other. Thus, the constants of the dissipation model depend on the constants of other parts of the complete model.

The value of C_{D1}= 0,135 was chosen using the approximation $\varepsilon \cong w'' = \frac{3}{2} C_{D1} \frac{u'^3}{L'}$. The turbulence viscosity $\nu_t = u'L'$ can be expressed by $\nu_t = \frac{3}{2} C_{D1} \frac{u'^4}{\varepsilon} = \frac{2}{3} C_{D1} \frac{k^2}{\varepsilon}$. Then, C_{D1} corresponds to the constant C_μ(= 0,09) in the widely used k-ε model [108].

3.5.4.2. Energy cascade and fine structures

The turbulence model expresses phenomena related to the first level of the energy cascade. The chemical reactions take place where the reactants are mixed molecularly, that is, mainly in the fine structures, which are the small vortices. The energy cascade model described above gives a relationship between large and small scales.

The production of the kinetic energy of turbulence, or transfer of energy from the mean flow to the turbulence, is a function of characteristic quantities of the mean flow and the turbulence. Likewise, the transfer from the first to the second level must be a function of quantities related to the two levels. In the combustion model, the energy cascade was used to find a set of relationships that control the rate of reaction, see e.g. Magnussen [109] and [110]. Here, the expressions will be redeveloped without introducing values into the constants.

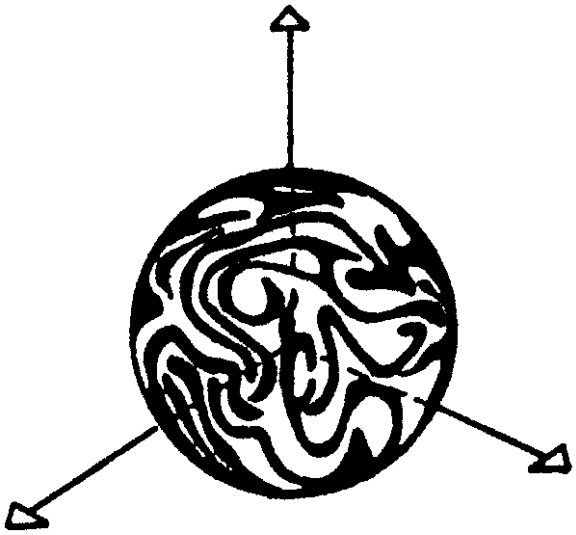

Figure 3.6: Fine structures [111]

At high Reynolds numbers, the transfer from the first to the second level, w'', is much greater than the direct dissipation of the first level, q'. In other words, the dissipation ε is approximately equal to the energy transfer w''. Also, it has been shown that ¾ of the dissipation is done at fine scales, and thus we obtain:

$$\varepsilon = \frac{3}{2} C_{D1} \frac{u'^3}{L'}, \text{ et } \varepsilon = \frac{4}{3} q^* \text{ alors } \varepsilon = \frac{4}{3} C_{D2} \nu \frac{u^{*3}}{L^{*2}} \quad (3.78)$$

With the assumption of equilibrium at the last level we obtain:

$$\varepsilon = \frac{4}{3} w^* = 2C_{D2} \frac{u^{*3}}{L^*} \tag{3.79}$$

The last two equations give the characteristic scales of fine structures:

$$L^* = \frac{3}{2}\left(\frac{3C_{D2}^3}{C_{D1}^2}\right)\left(\frac{\nu^3}{\varepsilon}\right)^{1/4} \tag{3.80}$$

$$u^* = \left(\frac{C_{D2}}{3C_{D1}^2}\right)^{1/2} (\nu\varepsilon)^{1/4} \tag{3.81}$$

These scales are of the same order of magnitude as the Kolmogorov scales. The ratio of fine-grained mass to total mass has been expressed (Magnussen et al., 1978; Magnussen, 1981a) as:

$$\gamma^* = \left(\frac{u^*}{u'}\right)^3 = \left(\frac{3C_{D2}}{4C_{D1}^2}\right)^{3/4} \left(\frac{\nu\varepsilon}{k^2}\right)^{3/4} = \frac{L^*}{L'} \tag{3.82}$$

It is also the intermittency factor of fine structures. It was believed that the fine structures are mainly located in the regions between larger energy-rich vortices. Mass transfer between fine structures and the environment, divided by finely structured mass, was modeled by Magnussen [109][111]:

$$\dot{m}^* = \frac{1}{\tau^*} = 2\frac{u^*}{L^*} = \left(\frac{3}{C_{D2}}\right)^{1/2} \left(\frac{\varepsilon}{\nu}\right)^{1/2} \tag{3.83}$$

The inverse of this quantity $\tau^* = \frac{1}{\dot{m}^*}$ is considered to be the characteristic time scale of fine structures. This is the time scale of fluid dynamics for chemical reactions.

Inputs and outputs of the energy cascade model

The data needed for the waterfall model presented here are the turbulence energy (*k* or *u'*) and a turbulence timescale or length scale (*L'*). These can be found from modeled transport or equilibrium equations (i.e. a statistical model of turbulence). The result of the waterfall model is the average mixing rate in the turbulent flow which linearly relates to the average reaction rate $\widetilde{\omega}_i$.

3.5.5. EDC model

The EDC model divides the reactive fluid into a reaction zone (fine structures, denoted by *) and a non-reaction zone (environment, denoted by °). The fine structures are vortex-leaf or tube-like in shape and are on the order of the Kolmogorov scale in two dimensions but a

larger scale in the third dimension [109].Reactions occur in these spatially isolated regions, occupying only small fractions of the flow, where gas-phase species mix at the molecular level. This is done by turbulent mixing in Kolmogorov structures where the movement of the fluid is dissipated into thermal energy due to viscous forces. The EDC model gives an empirical expression for the average reaction rate based on the assumption that the chemical reaction occurs in regions where the dissipation of turbulence energy takes place.

The EDC model is an extension of the EDM model [110] and allows the inclusion of detailed chemistry in turbulent flows through reaction mechanisms. The source term in the average conservation equation for species *i* is modeled as:

$$\widetilde{\omega}_i = \frac{\rho\gamma^{*2}}{\tau^*[1-\gamma^{*3}]}(Y_i^* - \bar{Y}_i) \tag{3.84}$$

With γ^* the volume fraction of the fine-scale (eq. (3.82)), Y_i^* is the mass fraction of the fine-scale after reaction along time τ^* (eq. (3.83)).

In ANSYS Fluent, combustion in fine structures is assumed to occur in a PFR (Plug Flow Reactor) at constant pressure, with the initial conditions taken equal to those of the species and temperature in the cell.

3.6. Radiation modeling

In flameless or MILD combustion, radiation plays an important role, particularly for traditional large-scale furnaces. In the latter, radiation was demonstrated to be the dominant heat transfer mechanism especially between the reactive mixture and walls Sorrentino et al [108]. The cases studied in this work are all lab-scale facilities, moreover, heat transfer to the walls was not considered. This allows the adaptation of a simplified model to handle radiation. Here, the P-1 model was considered to compute the radiation heat loss $\dot{\bar{Q}}_{rad}$ in equation (3.12).

3.6.1. The P-1 radiation model

The P-1 radiation model is the simplest case of the more general P-N model developed by Cheng [112]. This model is founded on the expansion of the radiation intensity *I* into an orthogonal series of spherical harmonics. If only four terms in the series are used, the radiative heat flux writes:

$$\dot{\bar{Q}}_{rad} = -\Gamma\nabla\mathrm{G} \tag{3.85}$$

Where the parameter Γ equals:

$$\Gamma = \frac{1}{(3(a+\sigma_s)-C\sigma_s)} \tag{3.86}$$

With *a* the absorption coefficient, σ_s is the scattering coefficient, and C is the linear-anisotropic phase function coefficient.

In the equation (2.85), G is the incident radiation given by the transport equation:

$$\nabla.(\Gamma\nabla G) - aG + 4an^2\sigma T^4 = 0 \tag{3.87}$$

Here, n is the refractive index of the medium, and σ is the Stefan-Boltzmann constant. A combination of equations (2.85) and (2.87) yields the expression of the radiative flux:

$$\nabla.\bar{\dot{Q}}_{rad} = aGS_G - 4an^2\sigma T^4 \tag{3.88}$$

3.6.2. Mechanisms of NO production

Four routes of nitric oxide NO are considered in this study, namely: thermal or Zeldovich mechanism [113], prompt or Fenimore [113] path, N_2O intermediate mechanism, and NNH mechanism [113][114]. In the thermal mechanism, NO is formed by breaking the triple bond of N_2 at high temperature (>1700K) by O atoms to obtain N atom, which is oxidized to NO, by the following reactions:

$$O+N_2 \rightleftarrows NO+N \tag{3.89}$$

$$N+O_2 \rightleftarrows NO+O \tag{3.90}$$

$$N+OH \rightleftarrows NO+H \tag{3.91}$$

The reaction given by (3.89) requires high activation energy to occur; therefore, it has a very strong temperature dependence [113]. Prompt mechanism occurs when hydrocarbon radicals CH_X (e.g. CH, CH_2, CH_3…. Etc.) react with nitrogen N_2 to form HCN. Then, the latter is converted into NO through various intermediates. The N_2O intermediate mechanism converts N_2 to N_2O by following three steps mechanism:

$$O+N_2+M \rightleftarrows N_2O+M \tag{3.92}$$

$$H+N_2O \rightleftarrows NO+NH \tag{3.93}$$

$$O+N_2O \rightleftarrows NO+NO \tag{3.94}$$

This mechanism becomes important in case of fuel lean and low temperature condition. The NNH mechanism forms NO by transformation of N_2 through intermediate reactions:

$$N_2+H \rightleftarrows NNH \tag{3.95}$$

$$NNH+O \rightleftarrows NH+NO \tag{3.96}$$

Detailed reactions for each NO mechanism can be found in[115] and [114].

To calculate NO production from a specific path, its main initiation reactions are disactivated. For example, the thermal route is suppressed by disactivating the reaction N+NO<=>N_2+O while the prompt one by disabling reactions CH+N_2<=>NCN+H and CN+N<=>C+N_2. Then the difference between the full mechanism and the concerned one, in which the path is disabled, is computed, [116]. This procedure is necessary as many NO production reactions are shared by different routes.

3.6.3. Emission Index for NO EINO

To quantify the NO species emission, the EINO index is introduced [117] by the amount of NO produced by kg of fuel used:

$$EINO = \frac{\int_0^l W_{NO}\dot{\omega}_{NO}dx}{-\int_0^l W_{Fuel}\dot{\omega}_{Fuel}dx} \quad (3.97)$$

Where W_i is the moleculae weight of species *i* and $\dot{\omega}_i$ is the rate of production of species *i* by chemical reaction.

CHAPTER IV

Numerical computations and results interpretations

In this chapter, computations of several configurations are performed to validate the numerical procedure. Beginning with the well-known opposed jets flames in turbulent regime, then the bluff-body jet flames, and finally the Jet in Hot Coflow (JHC) burner. Since the last geometry is usually used in gas turbine chambers, main computations are achieved by adopting the JHC burner. Effects of the biogas-syngas mixture, hot co-flow temperature, fuel jet Reynolds number, and finally the effect of oxygen volume in the hot co-flow on MILD combustion structure and emissions were elucidated. Several turbulence models, turbulent combustion models, and chemical kinetics mechanisms were tested, Table 4.1.

Table 4. 1.Summary of geometries and models used in computations

Geometry	**Used for**	**Turbulence models**	**Turbulent combustion model**
Opposed jets	Validation	RSM, k-ε, k-*ω*, SST k-*ω*.	SLFM/Conventional
Bluff-body	Validation	RSM, k-ε, Modified k-ε Realizable k-ε, SST k-ω	EDC/Conventional
Jet in Hot Co-flow	Validation/ computations	k-ε, Modified k-ε Realizable k-ε, SST k-ω	EDC/MILD

4.1. Numerical procedure validation

4.1.1 Computation of turbulent counterflow flames

Turbulent Counter-Flow Flame (TCF) is one of the most combustion devices used to study this type of biofuels combustion. This device is composed of two simple jets impinging each other. This makes a simple axisymmetric flow field formed by a stagnation region in which the flame takes place. This configuration provides several advantages such as facilitating the measure of extinction and ignition limits. Furthermore, the simple velocity field in this geometry offers simplification to the theoretical treatment. It also makes it easier to validate with numerical simulations.

4.1.1.1 Geometry and numerical procedure

The configuration considered here is the counter-flow diffusion flame of Mastorakos et al.[118][119]. The geometry is composed of two opposed jets streaming fuel mixture from the left side, and air and N_2 co-flow from the right one. The diameter of jet fuel is Di=25.4mm and the co-flow Do=51.8mm. The distance between the jets is H=25.4mm. The stagnation plane of the jets is adjusted by a balance of fuel and oxidizers jets momentum flow rates: $(\rho U_1 \cdot U_1)_{oxidizer} = (\rho U_2 \cdot U_2)_{fuel}$. The position of the stagnation points lays in the mi distance between two jets. Figure 4.1 presents a sketch of this setup; the parameters of the configuration are shown in Table 4.2.

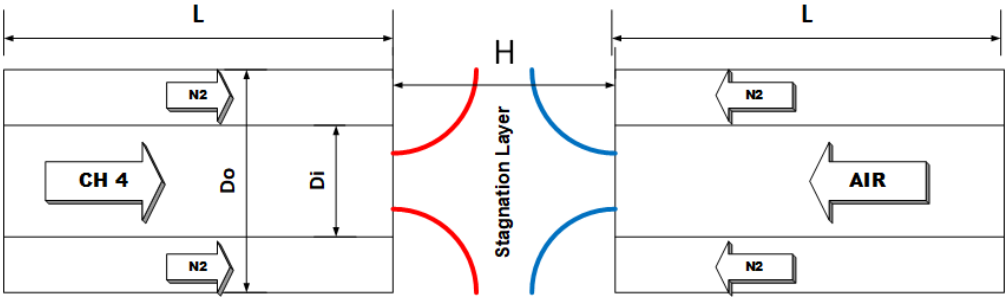

Figure 4.1: Counterflow opposed jets configuration

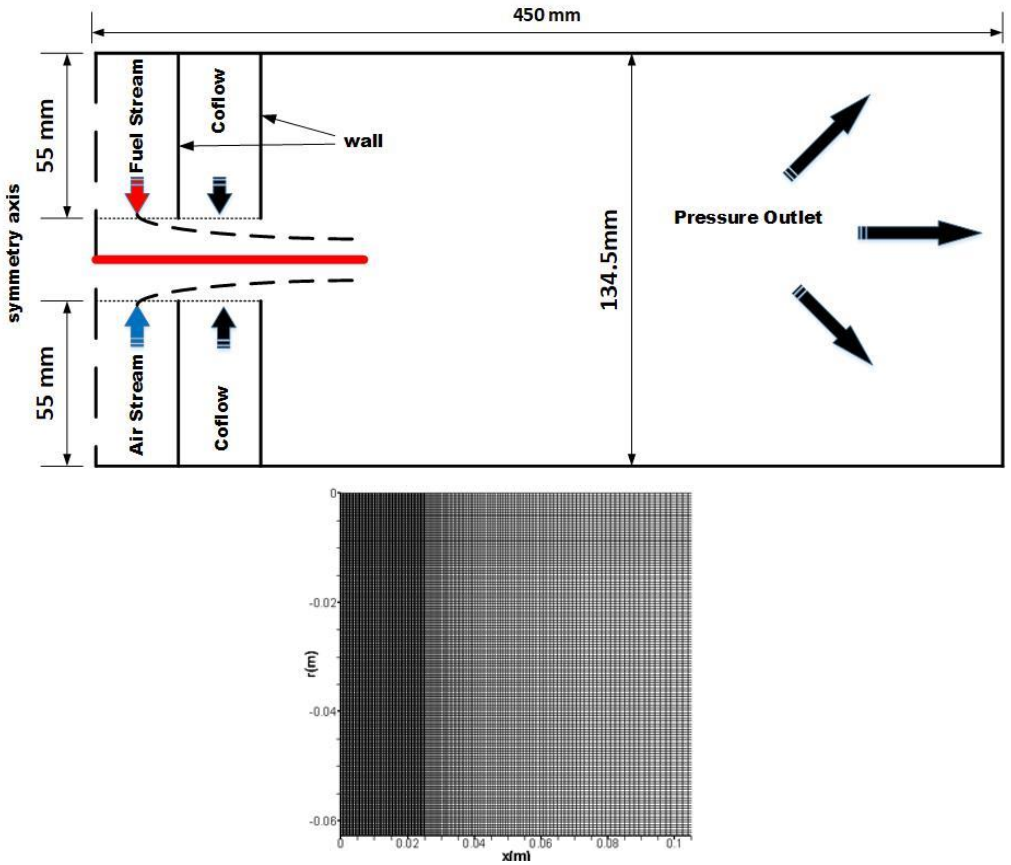

Figure 4.2: Computational domain of the counterflow burner of Mastorakos et al. [118]

Table 4. 2: Dimensions of the counterflow jets, Mastorakos et al. [118]

Jet	D (mm)	L (mm)	H (mm)
Air/fuel	Di=25.4	55	25.4
Co flow	Do=51.8	55	25.4

The computational fluid domain and mesh zoom are shown in Figure 4.2, the opposed jet burners are designed to produce a plane axisymmetric flame in the center of the flow field. Thus, facilitating experimental investigation and calculations. The boundary conditions for the computations are inlet flow velocity and turbulent intensity from experimental data, pressure outlet for the flow outlet, wall conditions for duct walls, and axis condition for the axisymmetric axis. In experience the co-flow is fed by nitrogen (N_2), this was not possible to include in computations since we used the Steady Flame let Model (SFLM) which handles only one mixture fraction. This configuration produced a flame at the exit of co-flow on the fuel side and could affect downstream profiles. However, our main interest is along the center line and this flame does not affect the flow there. The temperature of both fuel and oxidizer streams are taken 300 K. The boundary conditions are shown in Table 4.3:

Table 4. 3: The boundary conditions

Velocity	U_{air} =1.48 m/s	$U_{fuel} = \sqrt{\frac{\rho_{air}}{\rho_{fuel}}}\, U_{air}$	U_{coflow}=0.5 m/s
Species	CH_4	O_2	N_2
Fuel stream	100%	0%	0%
Air stream	0%	21%	79%

4.1.1.2 Solution-mesh independency:

A solution-grid independency check was conducted for three meshes (coarse (50 000 cells), medium (60 000 cells), and fine (90 000 cells). The computations were performed using the SST k-ω model for turbulence and the SLFM [120] for turbulent combustion. A comparison of mean temperature profiles and methane mass fraction Y_{CH4} in the centerline of the opposed jet is presented in Fig. 4.3. The profiles of the fine and the medium grids are similar for both

mean temperature and methane mass fraction, thus to reduce the computational efforts, we use the medium mesh in our computations, Fig. 4.2.

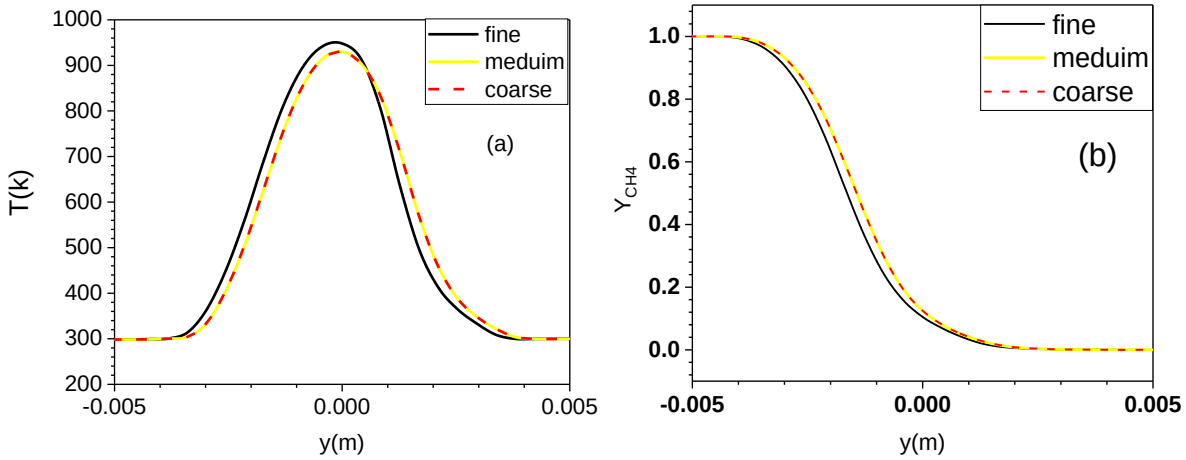

Figure 4. 3: (a) Mean temperature and (b) Mass fraction of CH_4 at the centerline

4.1.1.3 Model validation and comparison between turbulence models

Due to the lack of experimental data for biogas-syngas non-premixed counter-flow flames in the turbulent regime. The experimental non-premixed turbulent counterflow flames for methane-air [119] are used for the validation of the adopted model. Numerical calculations are compared to experimental data of Mostorakos et al. [117]. Figure 4.4 shows a comparison between the mass fraction of reactants species (CH_4, N_2, and O_2), product ones (H_2O), and mean axial velocity in the centerline. The results show a good agreement between experimental data and numerical calculation for the mass fraction of species. While the mean axial velocity in the exit of the nozzle is poorly predicted, as shown in Fig. 4.5.

Figure 4.6 presents a comparison between three turbulence models (RSM [121][122], k-ε model [87] and SST k- ω[123]) with and without radiation (P1-model) [112] against the experimental data [12.13]. Except for the k-ω model, the results reveal that all turbulence models give acceptable results, where it noticed that all predictions are close to each other. Moreover, the SST k-*ω* model provides a more accurate prediction compared to other turbulence models. It also requires less computational effort compared to other models.

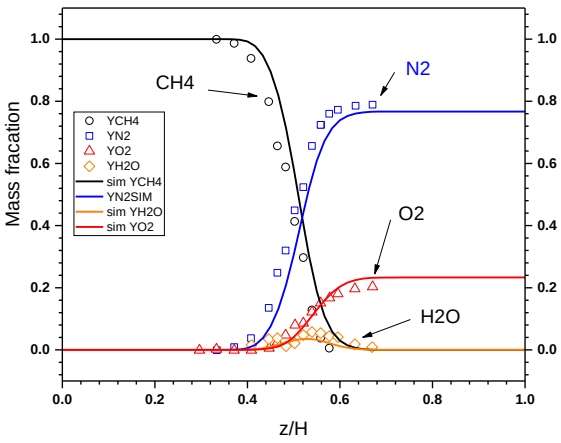

Figure 4.4: Mean mass fractions along the center line for Mastorakos [117] (U_{ox}=1.48m/s) against our computational (SST k-ω model).

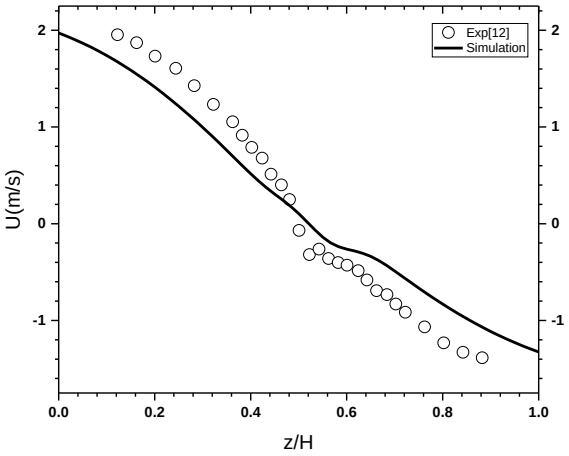

Figure 4.5: Mean velocity axial along the centerline for Mastorakos [117] (Uox=1.48m/s) against our computational (SST k-ω model).

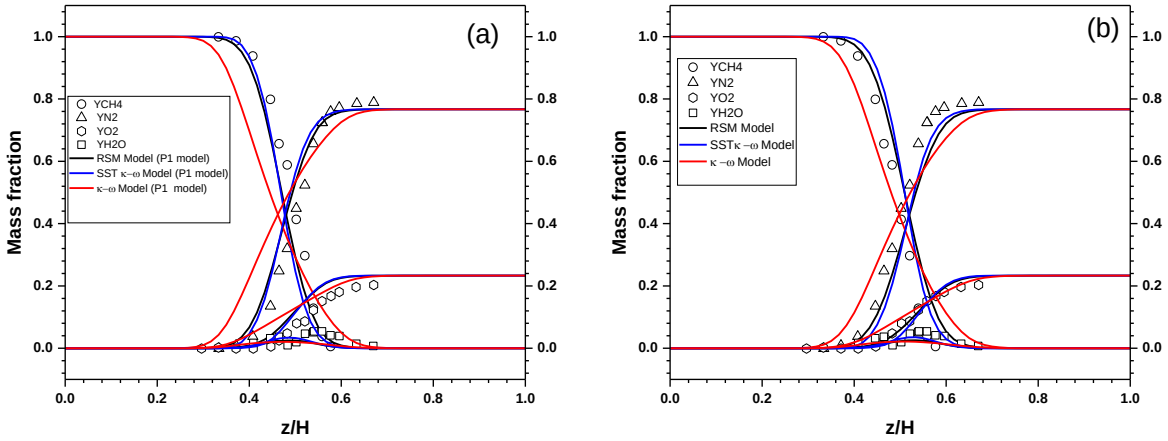

Figure 4.6: Comparison between mean mass fractions experimental data [] and computational results with (a) and without (b) radiation model along the centerline.

4.1.2 Computation of turbulent bluff-body jet flames

This part aims to compare different turbulence models performance in conjunction with the Eddy Dissipation Concept (EDC) model for turbulence-combustion interaction handling. In our computations, we have compared the results of five turbulence models. The geometry used is the bluff-body jet which is generally used to stabilize flames under high injection velocities. Figure 4.7 shows the Sydney bluff-body burner which is composed of a cylindrical bluff-body with a diameter D = 50 mm and placed in a coaxial oxidizer flow. On the centerline of the bluff-body, a nozzle with a 3.6 mm diameter propagates fuel into the recirculation zone immediately next to the bluff-body surface. The central jet is composed of the methane-hydrogen mixture (1:1 in volume) at a temperature of 298K. The resulting stoichiometric mixture fraction value is Zst=0.05. The burner was investigated by Masri et al. [47], and by Dally et al. [124]. The

major and minor species concentrations are measured at different radial and axial locations in the flame [125]. A detailed description of the experimental technique employed for the measurement of temperature and species concentrations has been reported in [45]. The bluff-body, coated with a ceramic layer, creates a recirculation zone which substantially improves the flame stability over an extensive range of co-flow and jet conditions. These flames have been used to validate different combustion models such as Conditional Moment Closure (CMC) [26], Probability Density Function (PDF)[126], and flamelets model[127]. The operating conditions for numerical computations are taken from experience and given in Table 4.4.

Table 4. 4: Boundary conditions for the experimental setup[47]

Case	Fuel (%) vol.	Co-flow (%) vol.	Velocity (m/s)	Re Number	Z_{st}	Tin
HMe1	CH_4=50	O_2=21	V_f=108	15800	0.05	300K
	H_2=50	N_2=79	V_{air}=35			

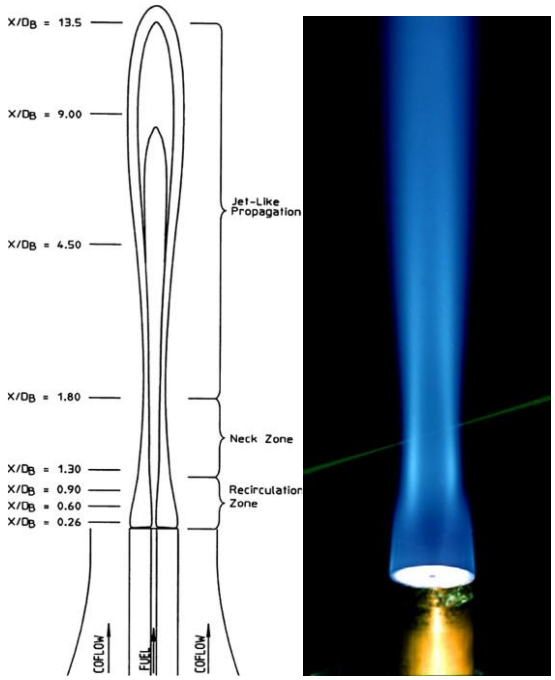

Figure 4. 7: Sydney Bluff-Body Burner

4.1.2.1 Model validation and comparison between turbulence models

Figure 4.8. shows an overall comparison between the experimental flame image of the Sydney Bluff-body flame HM1 [124] and the simulated contours of the flame temperature distribution. Both dimensions of numerical and experimental distributions of temperature matched reasonably. The temperature contour is highly relevant to the flame structure, and it will to some degree be helpful to understand the behaviors for the bluff body flame.

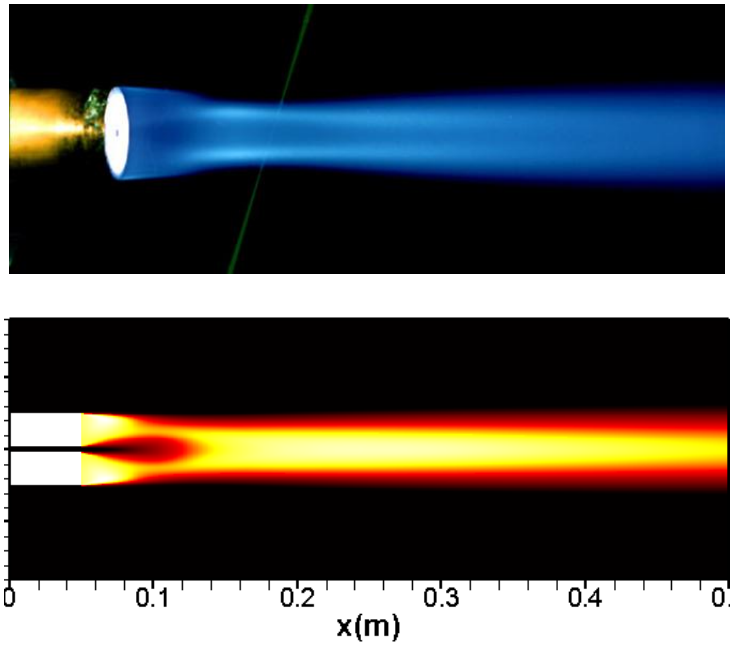

Figure 4. 8: Comparisons between Sydney Bluff Body flame images [124] and simulated flame contours.

To get more insight into the Bluff-body flame, the comparison with the experimental data focuses on the statistical data at four axial locations x/D=0.26, 0.6, 0.9, and 1.8. Five turbulence models are used, namely: standard k-ε, realizable k-ε, modified k-ε, k-ω SST and RSM models. Mean radial profiles of temperature, axial velocity, and mixture fraction were predicted. The numerical radial profiles are in accordance with experimental data at the two-station x/D=0.26 and 0.6. Nevertheless, at both locations x/D=0.9 and 1.8, the predictions are slightly overvalued, as shown in Fig. 4.9. (a). It can be seen that the k-ω SST performed a good prediction compared to the standard k-ε and realizable k -ε, Fig. 4.9. Furthermore, both modified k-ε and RSM models show a noticeable superiority in the prediction of the last station x/D=1.8. Figure 4.9 (b) shows a comparison of radial profiles of axial velocity U at four locations; despite some discrepancies, globally acceptable agreement with experimental data is noticed. The mean axial velocity at the centerline decreases more rapidly than in experimental data. Expect the RSM model, all turbulence models underpredict the axial velocity, this can be attributed to the shortcomings of RANS turbulence models, which are known to overpredict the decay rate of the round jet. To bypass this issue, Dally et al [128] suggested a modification to the standard k-ε constant model from C_{μ}=1.44 to 1.6. The latter provided a better prediction except for locations x/D=0.9, and 1.8. Figure 4.9 (c) shows the computed mean mixture fraction profiles compared with the experimental data at different axial locations. In general, the numerical results from all the turbulence models compare acceptably with data; also, the superiority of the RSM model can be seen near the axis.

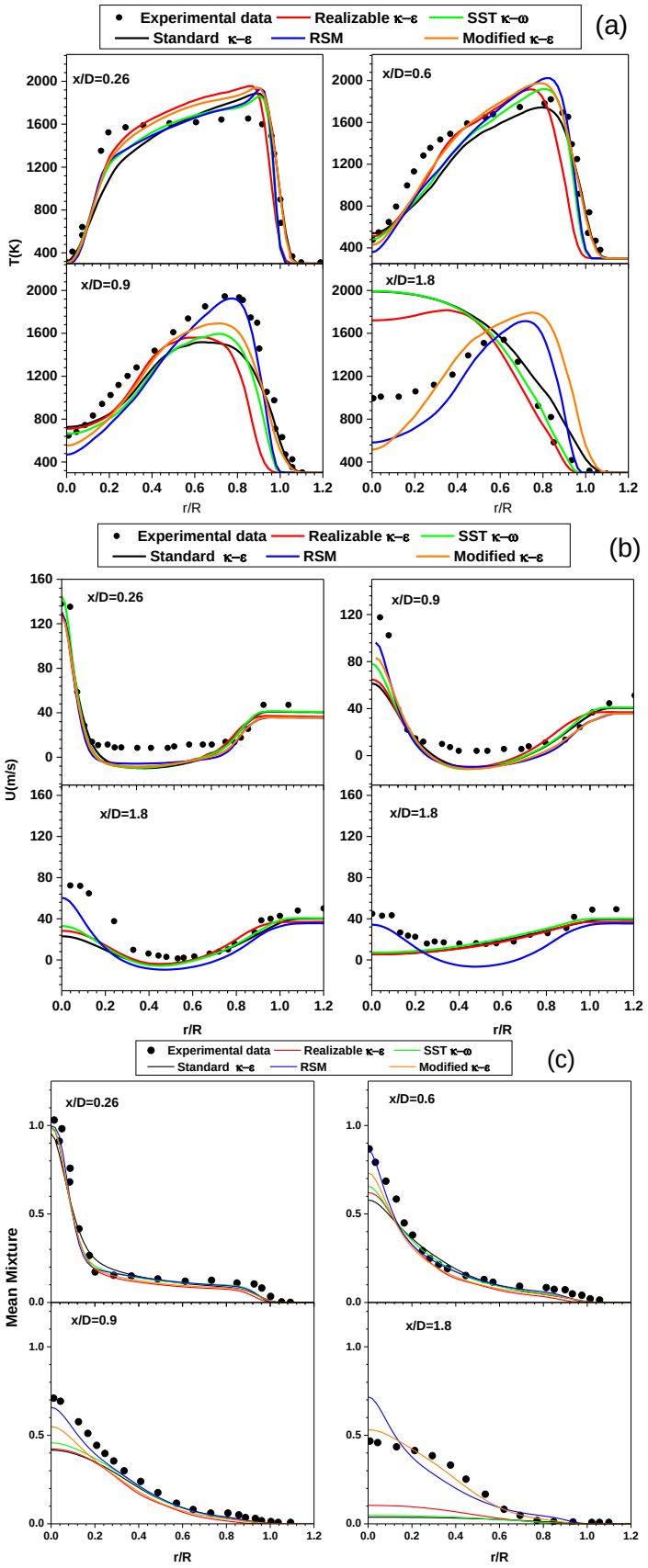

Figure 4. 9: Comparison between simulations and experiments, a) radial profiles of flame temperature, b) radial profiles of axial velocity and c) radial profiles of mean mixture fraction

4.1.3 Computation of turbulent Jet in Hot Coflow burner flames

The last configuration used to validate the numerical procedure and to perform computations is the Jet in Hot Coflow burner (JHC) of Dally et al [51], Fig. 4.10. Authors investigated MILD combustion by issuing a fuel jet into a hot co-flow. The fuel, composed of an equimolar mixture of CH_4 and H_2 (1:1 volume), is issued through a pipe of a diameter D_{jet}=2.25mm. Fuel is injected with a mass flowrate Q_{jet}=0.0045 kg/s and a Reynolds number of approximately 10000. The fuel jet is surrounded by an annular co-flow channel of a diameter D_{cf} =82 mm, which provides hot combustion products (O_2, CO_2, H_2O, and N_2), with a velocity v_{cf}=3.2m/s. Oxygen volume is varied from 3% to 9% with a constant temperature of T_{cf}=1300K. The burner is completely installed in a wind tunnel which provides a cold mixture of air (21% O_2 and 79% N_2) with a constant temperature of 305K.

Several turbulence models capabilities have been investigated, namely: Realizable k-ε [89], SST k-ω [92], and modified standard k-ε. The standard k- ε model is based on solving transport equations of turbulence kinetic energy *k* and its dissipation rate *ε*. According to the previous simulation works on the JHC for non-premixed hydrogen methane flame [52], $C_{1\varepsilon}$ in the dissipation rate equation was adjusted from 1.44 to 1.6 to improve the prediction accuracy of the standard k-ε model [129].

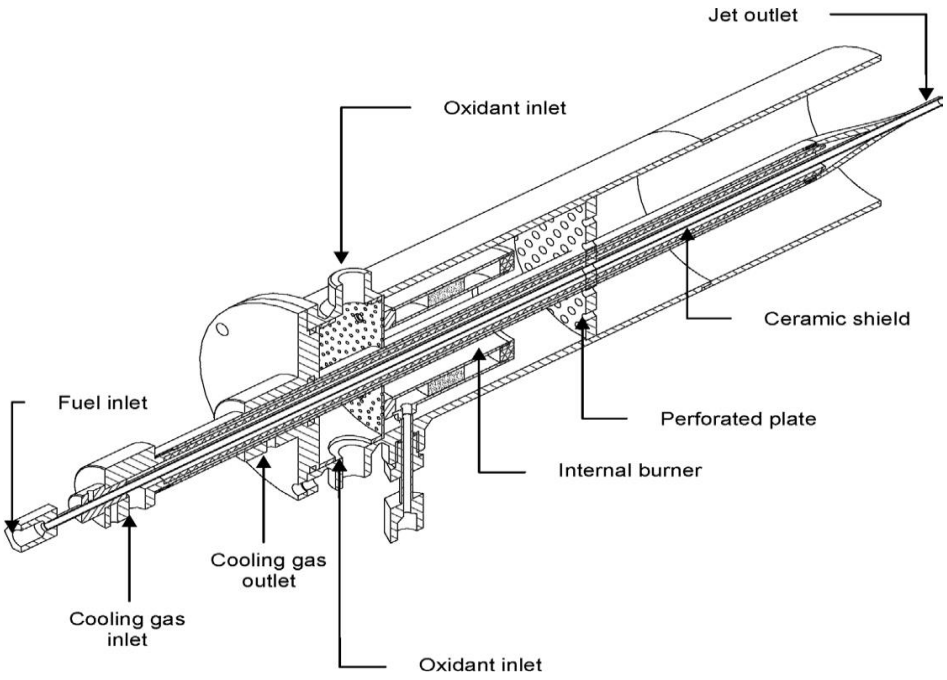

Figure 4. 10: JHC burner configuration [51]

The interaction of turbulence and combustion is a key in turbulent combustion simulation. In MILD turbulent combustion, the use of the EDC model [109], which is an enhanced version of the Eddy Break UP model EBU [130], has shown its performance. Several studies [129], [131] [132] have shown that the EDC model provides satisfactory prediction in MILD turbulent combustion.

4.1.3.1 Geometry and numerical details

The axial symmetry of the JHC geometry simplifies the problem to two-dimensional axisymmetric configuration. According to Parente et al [133] [134], a two-dimensional axisymmetric simulation could be used instead of a tridimensional one to reduce computational effort and to predict accurately as tridimensional simulation. Figure 4.11 shows the axisymmetric domain of the jet in a hot co-flow burner with a computational grid with about 25 000 cells. The solution-grid independency was verified by using three different meshes (coarse, medium, and fine). Detailed comparisons will be discussed in the next section. Numerical simulations were conducted by using the Fluent ANSYS CFD software based on the finite-volume method. The SIMPLE algorithm [135] was employed to solve the pressure-velocity coupling, the second-order upwind scheme was applied for all the governing equations. Residuals for all equations were kept less than 10^{-5} as a convergence criterion.

To have accurate predictions using the EDC model, it is crucial to tune boundary conditions, especially the mean kinetic turbulent energy [136], [137], and [52]. Consequently, the mean turbulent kinetic energy of fuel stream and hot co-flow are taken as 60 m^2/s^2 and 1.8 m^2/s^2, respectively. Moreover, according to Parente et al [134], the EDC model time scale constant $C_\tau = \left(\frac{C_{D2}}{3}\right)^{1/2}$ in Eq. (3.83) could be adjusted from 0.04082 to 0.82 to correct the overestimation in the JHC flame temperature. Lewandowski et al. [138] compared the EDC model modified constants with the original one, it was concluded that the variable reacting fraction approach gives a better estimation of the temperature field and lift-off height. In a recent paper, Lewandowski et al. [139] proposed a new method for model constants computations in the MILD regime. Making the model more general, the constants are a function of local turbulence Reynolds and Damköhler numbers. In a more recent paper, the authors Lewandowski et al. [140] applied the newly proposed model to twelve flames covering Adelaide and Delft burners in the MILD regime. A broad range of operating conditions was

covered and promoting results were obtained. Thermal radiation was neglected according to [52], it was found that thermal radiation didn't have any noticeable effect on the results.

Chemistry kinetics was described by three detailed mechanisms, namely: GRI-Mech 3.0 [141], which is composed of 53 species involving a total of 325 reversible reactions, GRI-Mech 2.11 [142], with 53 species and 277 reversible reactions and DRM-22[143], a reduced version of the full chemical mechanism GRI-Mech 1.2. According to the previous works of [137], [144], [145], [115], and [146], the GRI-Mech 3.0 overpredict NO levels comparatively to GRI-Mech 2.11.

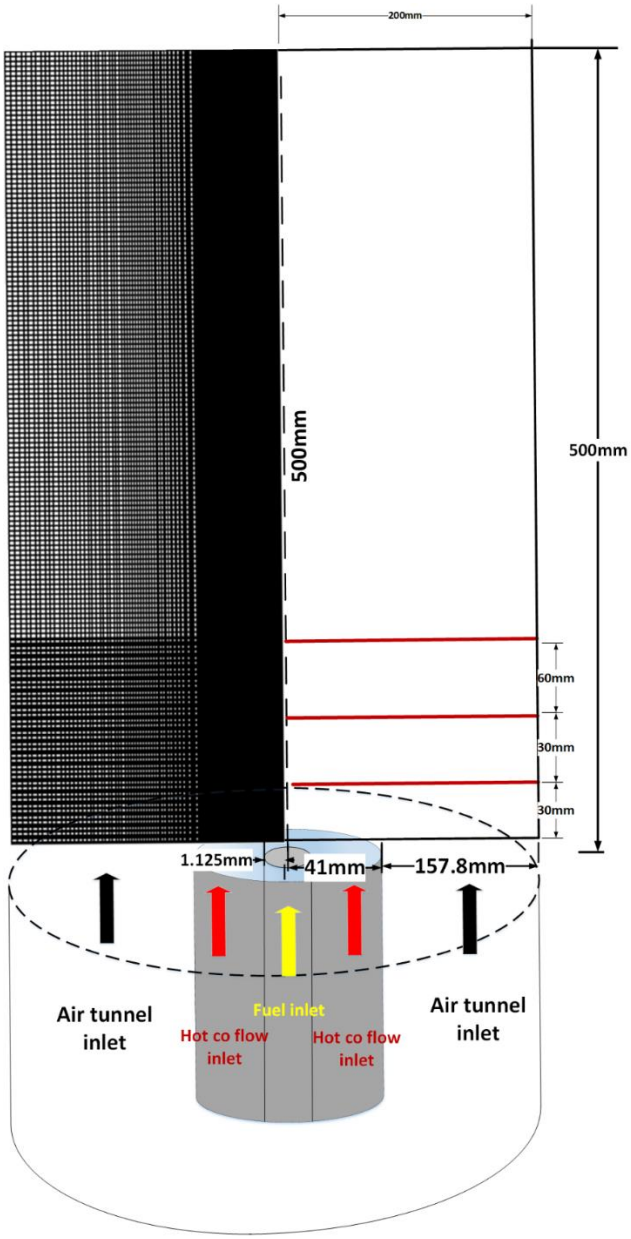

Figure 4. 11: The JHC burner and mesh of the computational domain

4.1.3.2 Solution-mesh independency

Several studies investigated the JHC burner, among them Mardani et al [54], Frassoldati et al [147], Wang et al [145], Mardani et al [24], Wang et al [136], and [148]. In these studies, it was noticed that a grid of nearly 22000 nodes was sufficient to get mesh-solution independence. In this study, the grid independency test is achieved by using several meshes and variables, three of them are presented, namely those with 9000, 36000, and 45000 nodes. The results on dynamic, thermal, and species fields were respectively represented by velocity, temperature, and mixture fraction. Figure 4.12 shows the variation of the considered parameters in both axial and radial directions (at x=60mm). Both grids of 36000 and 45000 nodes give similar results which means independency of the solution from the grid refinement. The grid of 36000 nodes was considered for computations.

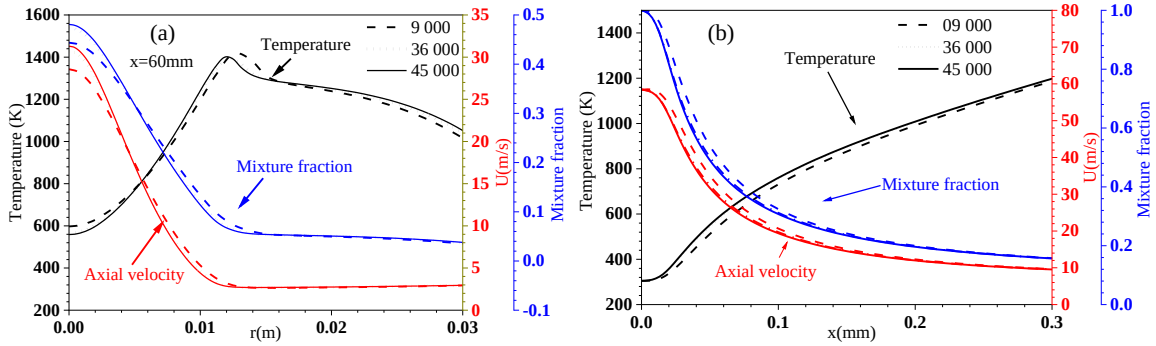

Figure 4. 12. Mesh independency for velocity, temperature, and mixture fraction.

4.1.3.3 Validation of the numerical method

Currently, there is no experimental data on the biogas-syngas mixture in turbulent flames under MILD conditions. Therefore, the experimental data of Dally et al [51] on CH_4/H_2 jet will be used for validation. Firstly, numerical simulation results are compared with experimental data in Fig 4.13 (a, b c, and d). Three cases that belong to oxygen mass fractions of 3%, 6%, and 9% (cases 1 to 3 in Table 4.5) are compared in terms of mean temperature, oxygen mass fraction, and mixture fraction. Four stations x=30mm, x=60mm, x=120mm and r=0mm (axial) were used. Generally, acceptable agreements between measurements and simulations for all test cases were observed. However, it is worth noting some disagreements in the peak and decay of the temperature profiles at the station x= 120 mm. This discrepancy is thought to be caused by the 2D axisymmetric solution and also turbulent combustion and turbulence models, as in [24], and [149]. It should be noticed that the flame above 100 mm from the nozzle is affected

by the mixing with fresh air from the wind tunnel, and thus the MILD combustion regime appears to be more pronounced below this height Dally et al. [51]. The problem of over-prediction of peak temperature could be attributed to the fact that the EDC model constants have been optimized for conditions other than the MILD regime. Previous studies adjusted the EDC model constants to improve predictions in the MILD regime. As it has been mentioned previously, the Lewandowski modification [139] was found to fit the best measurements, especially for temperature profiles peaks, Lewandowski et al. [140]. It can also be observed that accuracy of prediction, in both mean temperature and oxygen mass fraction, increases for high levels of oxygen. Therefore, an oxygen mass fraction of 9 % is selected in this study. Moreover, Fig 4.13 (b) shows that computed mixture fraction at the four stations x=30 mm, 60 mm, 120 mm and axial direction (r=0 mm) can accurately predict jet spreading and mixing. Which impacts significantly mean temperature and mass fraction results. The mean mixture fraction was calculated by Bilger's formula [102]:

$$z = \frac{\left[\frac{2(Z_C - Z_{C.ox})}{W_c} + \frac{2(Z_H - Z_{H.ox})}{2W_H} - \frac{2(Z_O - Z_{O.ox})}{W_O}\right]}{\left[\frac{2(Z_{C.fu} - Z_{C.ox})}{W_c} + \frac{2(Z_{H.fu} - Z_{H.ox})}{2W_H} - \frac{2(Z_{O.fu} - Z_{O.ox})}{W_O}\right]} \qquad (4.1)$$

Where Z_j is the mass fractions of elements (e.g. C, H, O) which can be obtained from the mass fractions of species containing these elements: $Z_j = \sum_{i=1}^{N} \frac{\Phi_{ij} W_j}{MW_i} Y_i$, where Φ_{ij} is the number of atoms *j* in species *i*. MW*i* and W*j* are the molecular weight of species *i* and the atomic weight of element *j*, respectively. The subscripts *ox* and *fu* refer to fuel and air streams, respectively. Secondly, a comparison between simulated contours of OH and experimental image of [51] for three flames HM1, HM2, and HM3 (cases 1 to 3 in Table 4.5) is shown in Fig. 4.14. It can be seen that increasing oxygen in the hot co-flow stream leads to a brighter flame. Specifically, the MILD region can be observed where the flame is not visible (x<100mm). Numerical results also showed that OH iso-lines can predict flame dimensions with good accuracy.

Table 4. 5. Validation compositions.

N°	ID	Hot oxidizer mass fraction				Chemical mechanism
		O_2	N_2	H_2O	CO_2	
1	HM1	0.03	0.85	0.065	0.055	Gri 2.11
2	HM2	0.06	0.82	0.065	0.055	Gri 2.11
3	HM3	0.09	0.79	0.065	0.055	Gri2.11, 3.0, DRM-22.

- Fuel: Y_{H2}=0.111, Y_{CH4}=0.889.
- Fuel Reynolds number: 10000

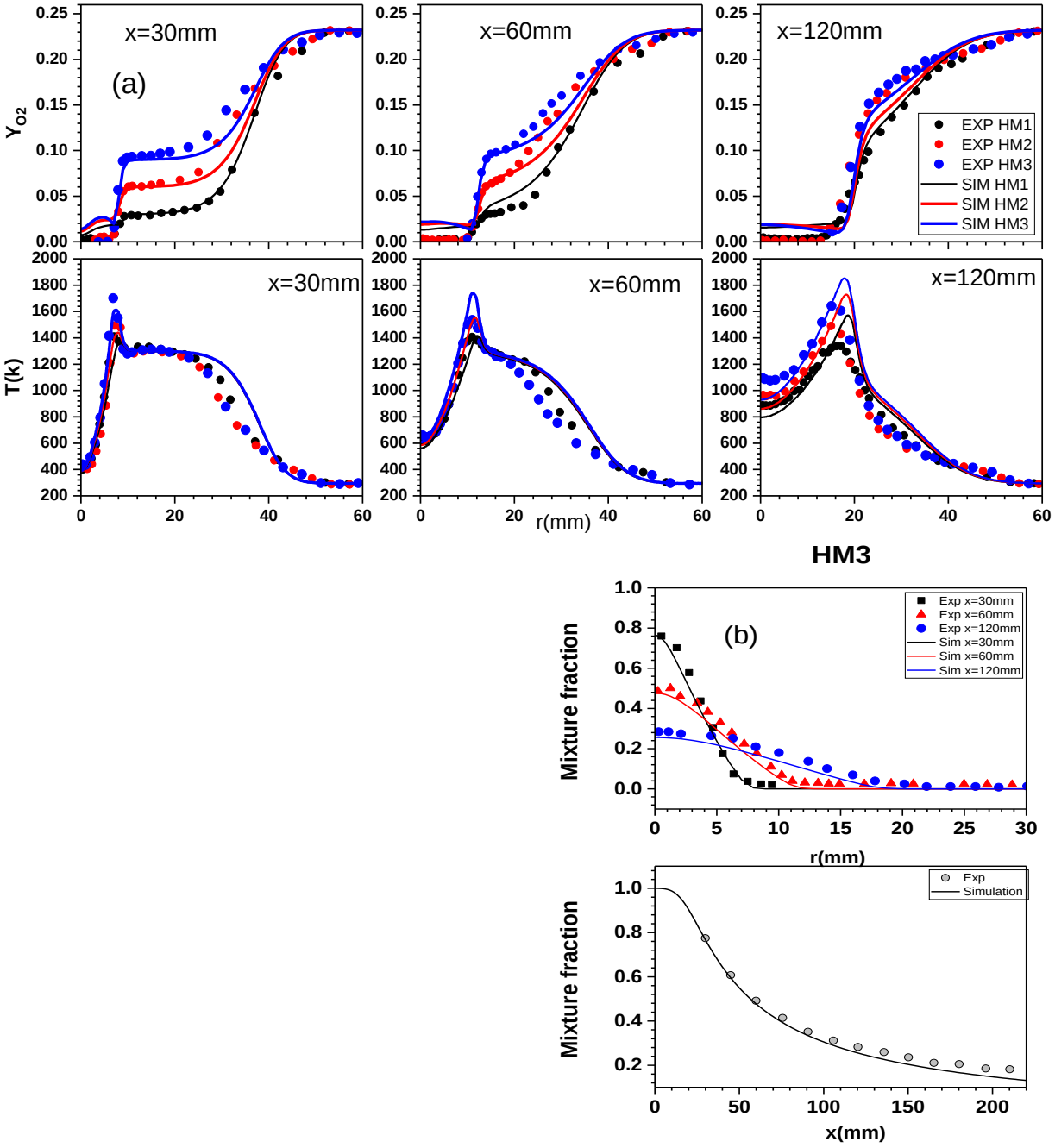

Figure 4. 13: Comparison between simulations and experiments at x = 30, 60 and 120 mm for three JHC flames of Dally et al. (a), and mixture fractions for HM3 (b).

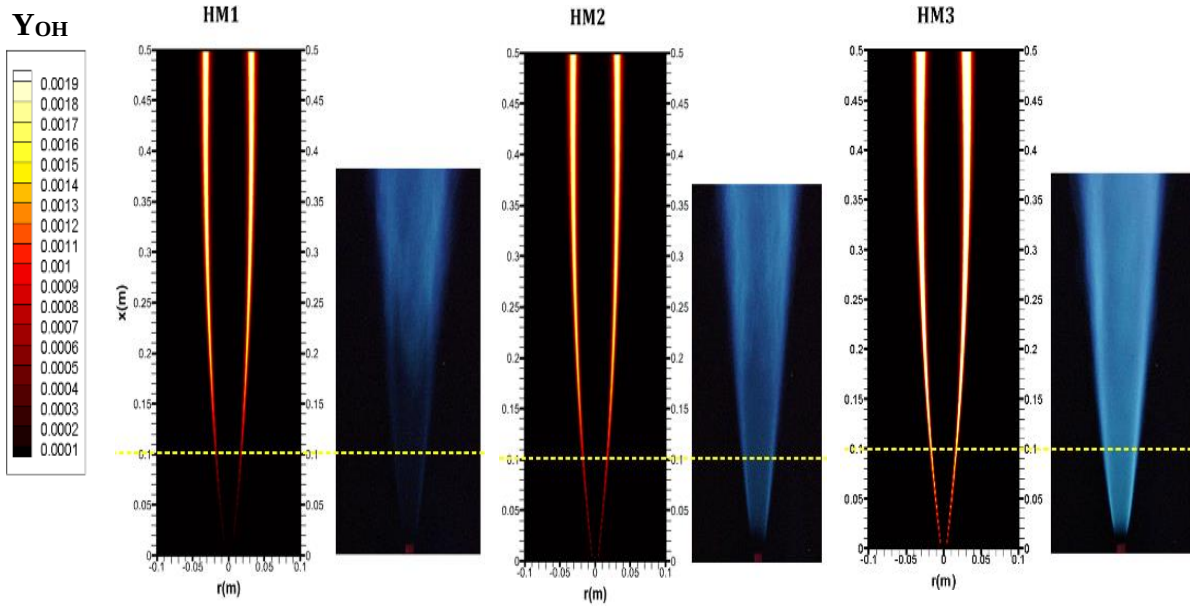

Figure 4. 14: Comparisons between JHC flame images and simulated OH molar fraction contours in the experiment of Dally et al [51].

4.2. Results and discussions

In the computations task, twenty numerical cases are studied and presented in Tables 4.6 to 4.9. The first three cases involve numerical procedure validation in H_2/CH_4 fuel mixture [51] followed by seven cases that investigate the effect of different $CH_4/CO_2/H_2/CO$ species concentrations (cases 4 to 10, Table 4.6). Then, three cases to investigate the effect of hot co-flow temperature (cases 11 to 13, Table 4.7). The simulations 14 to 16 in Table 4.8 analyze the Reynolds number of fuel inlet jet effect, and finally, cases 17 to 20 in Table 4.9 are dedicated to the effect of oxygen volume in the hot co-flow.

4.2.1 Effect of biogas-syngas mixture composition on flame structure and emissions

In this section, molar fractions of the fuel compounds (biogas-syngas) are varied according to equation (4.3). Firstly, in biogas, CO_2 is substituted by methane so that the molar fraction of methane ranges from X_{CH4}=0 to 0.5, that of carbon monoxide from X_{CO2}=0.5 to 0, and they sum to 0.5; while keeping hydrogen and CO mole fractions constant (X_{H2}=X_{CO}=0.25). Secondly, in syngas, the same procedure is repeated for hydrogen and carbon monoxide mole fractions; while keeping methane and carbon dioxide mole fractions constant (Table 4.6).

$$(0.5-\alpha)CH_4+\alpha CO_2+(0.5-\beta)H_2+\beta CO \qquad (4.2)$$

Table 4. 6: Fuel composition variation

N°	ID	Fuel composition mole fractions X_i				z_{st}
		CH_4	CO_2	H_2	CO	
4	B00S25	0.00	0.50	0.25	0.25	0.2703
5	B10S25	0.10	0.40	0.25	0.25	0.1563
6	B50S25	0.50	0.00	0.25	0.25	0.0359
7	B25S25	0.25	0.25	0.25	0.25	0.0844
8	B25S00	0.25	0.25	0.00	0.50	0.1078
9	B25S10	0.25	0.25	0.10	0.40	0.0984
10	B25S50	0.25	0.25	0.50	0.00	0.0625
Oxidizer: X_{O2}=0.09, X_{H2O}=0.065, X_{CO2}=0.055, X_{N2}=0.79. Fuel velocity: 58.75m/s.						

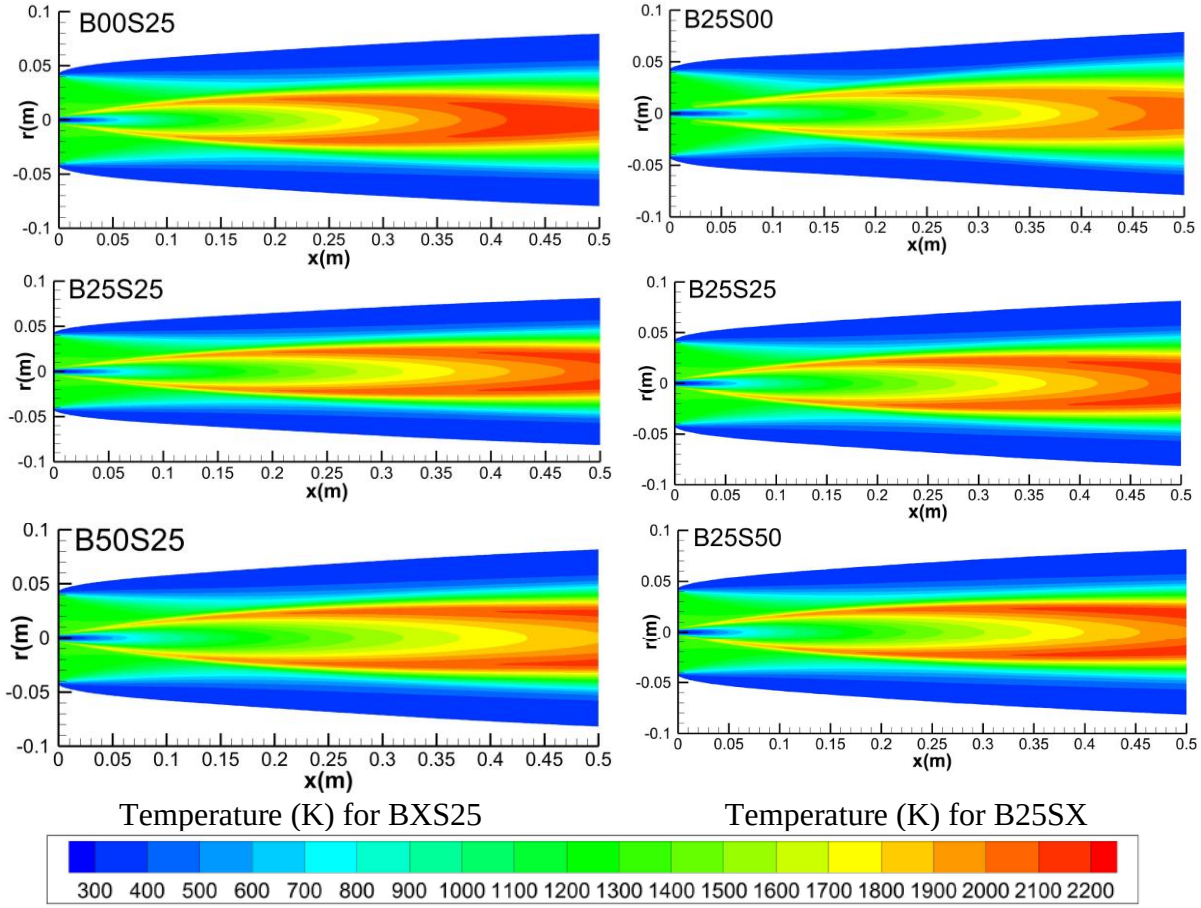

Figure 4. 15: Temperature fields for BXS25 and B25SX mixtures.

The temperature field is shown by Fig. 4.15 for both cases BXS25 and B25SX, the fuel jet is clearly visible surrounded by the hot coflow oxidizer and finally the cold tunnel air stream. While increasing methane in biogas or hydrogen in syngas, the hot zone is convected downstream the jet. Furthermore, the maximum temperature reduces from 2175 K for B00S25 to reach 2134 K for B50S25. This is probably the result of high local equivalence ratio due to the lack of oxygen in oxidizer to burn added methane. On the other hand, the temperature

increase when adding hydrogen to syngas from 2052K for B25S00 to 2163K for B25S50. This can be explained by the relatively low local equivalence ratio since hydrogen needs low quantities of oxygen to burn compared to methane. For both cases BXS25 and B25SX, it can be seen in Fig. 4.15 that small temperature increases are located near the injector which can warrants MILD regime in these regions. However, downstream the jet, the temperature is so much high and the MILD regime can't be preserved. So, globally two regimes coexist in such configurations, these remarks are also reported in many previous studies[51][24].

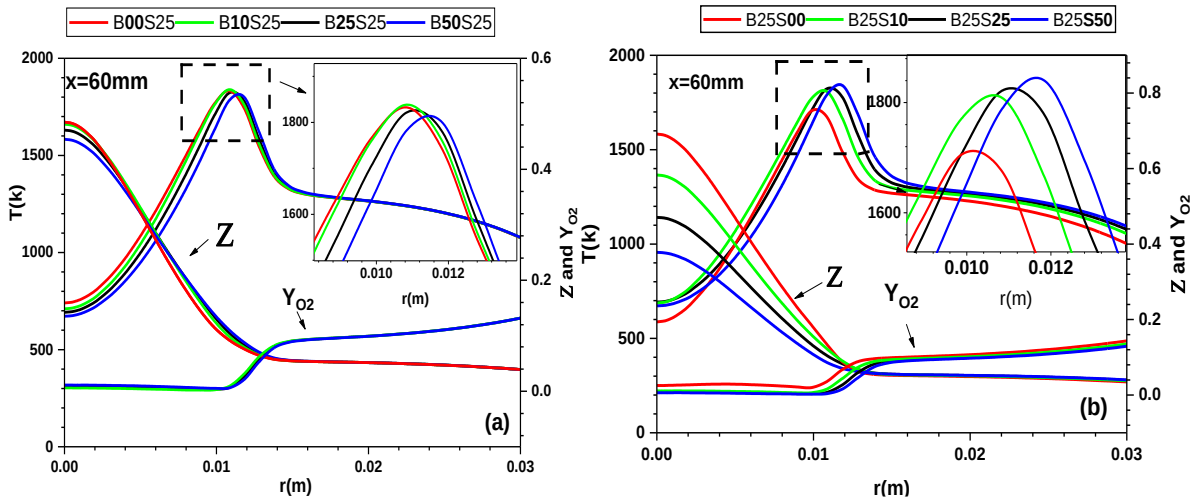

Figure 4. 16: Radial profiles of temperature, mixture fraction and Y_{O2} at x=60mm for :(a) cases 4 to 7 and (b) cases 7 to 10.

To get more insight into the MILD regime which is the subject of this part, the station x=60mm is selected since it warrants MILD regime combustion (combustion temperature increase didn't exceed mixture autoignition one which in general didn't exceed 850K). Fig. 4.16 (*a*) shows the variation of flame temperature, oxygen mass fraction, and mixture fraction *z*, which is computed by using Bilger's formula Bilger et al. [102] for different considered compositions (BXS25, X_{CH4}=0 to 0.5 and X_{CO2}=0.5 to 0). It can be observed that for all compositions, mean temperature profiles exhibit the same trends. They start from the lowest value on the axis of symmetry and increase to reach the maximum value at the mixing region between fuel and hot co-flow jet. Then they decrease to reach the temperature of hot co-flow 1300K and then the tunnel air T=300K. It has been observed that when methane mole fraction varies from 0 to 0.5, the maximum temperature slightly decreases from 1833K to 1815K (less than 1%), and its location shifts from 10.7 mm to 11.4 mm in the radial direction. This can be firstly explained by the trivial mixture fraction variations from one composition to another. Secondly, the lack of oxygen in MILD combustion makes the mixture locally rich which explains the slight decrease of temperature with methane addition. On the other hand, Fig 4.16

(b) shows that when hydrogen is added to syngas, maximum combustion temperature at this location (x=60mm) increases from 1712K for B25S00 to 1845K for B25S50 (nearly 7%). The maximum flame location shifts from 10.1 mm to 11.6mm in the radial direction. For this case, the mixture fraction varies significantly from one composition to another, this significate that mixing is enhanced since hydrogen is a very diffuse species.

The OH radical presence in the combustion pool gives indication about the combustion strength in resisting to stretch present in real combustion systems. Globally, when adding methane to biogas, the OH radical is slightly reduced. Contrariwise, if the hydrogen increases in syngas, the OH radical is nearly constant, Fig. 4. 17.

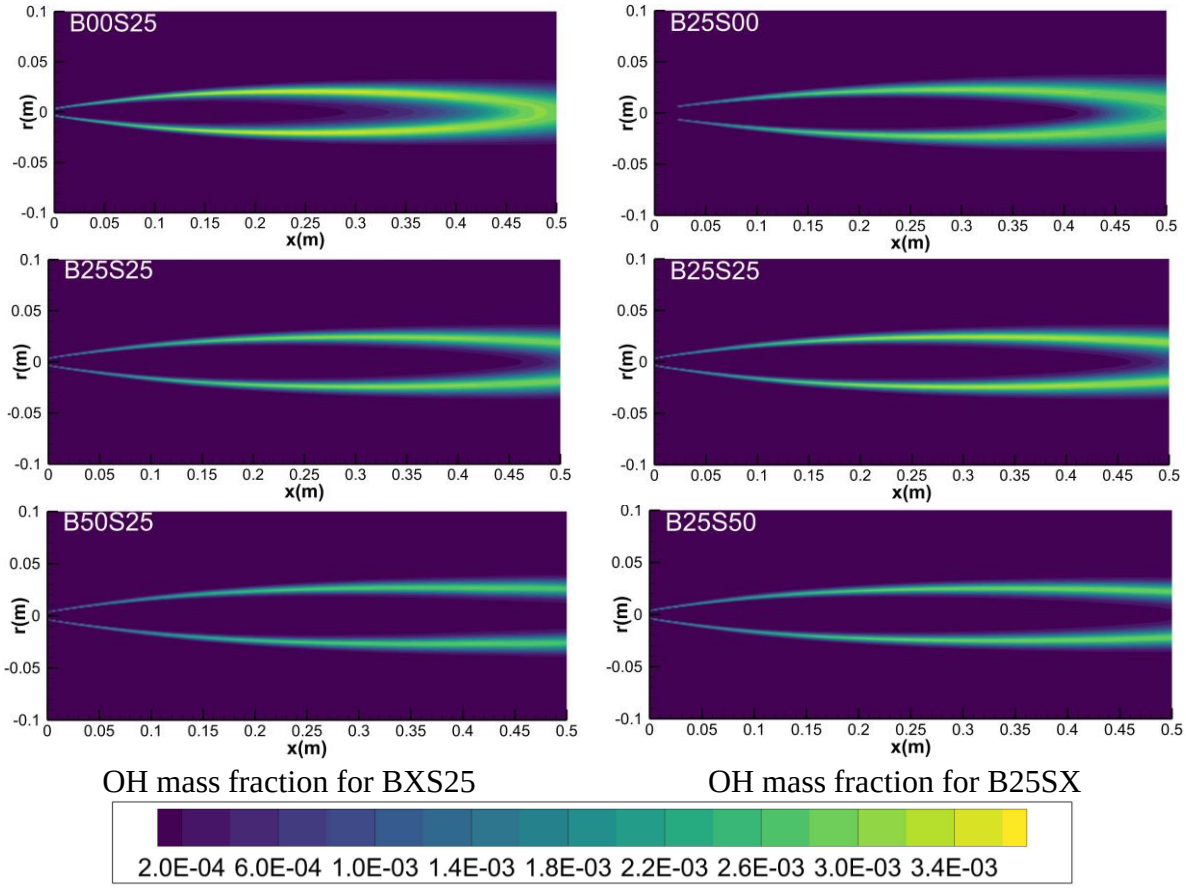

Figure 4. 17: OH radical mass fraction fields for BXS25 and B25SX mixtures.

Consumption of different fuel mixture compounds is shown by Fig 4.18 in the radial direction at station x=60 mm. Both cases of methane and hydrogen addition are respectively presented in Fig 4.18(a) and (b). Radial profiles show that consumption is enhanced by the increase of fuel compounds volume at the injection. All compounds vanish at r=12.5mm which indicates nearly the maximum flame temperature position. The exception is made for CO species which is injected and produced by CO_2 decomposition. It can be seen from CO profile

slope that CO is consumed, then produced at the flame front, and finally recombined to CO_2 after the flame front.

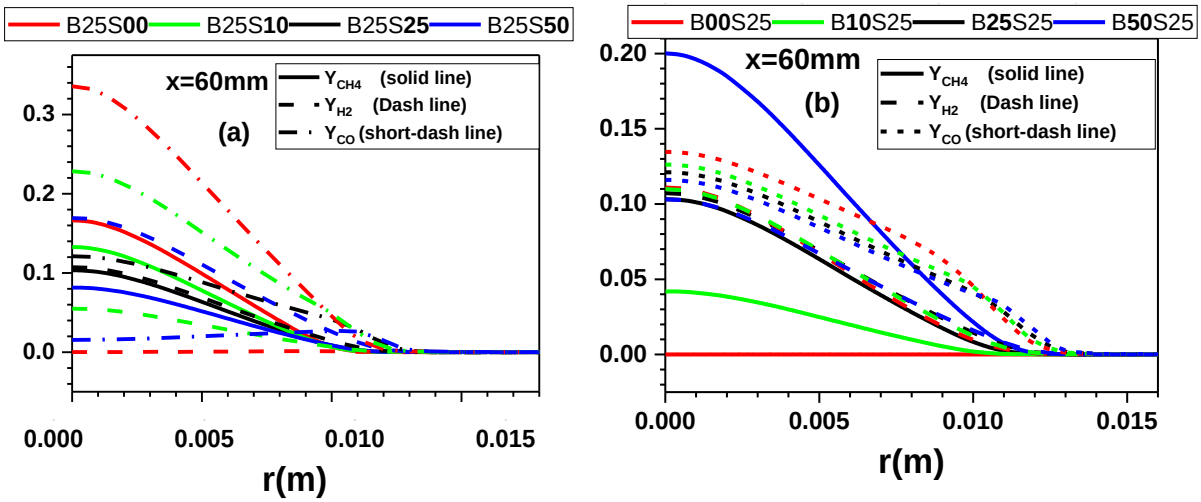

Figure 4. 18: Radial profiles of Y_{CH4}, Y_{H2} and Y_{O2} at x=60 mm for cases 4 to 10.

In Figure 4.19 methane and hydrogen effect on radial profiles (at x=60 mm) of both intermediate species OH and CH_2O mass fraction have been depicted (cases 4 to 10). The OH species is also an important indicator of heat release, fuel consumption, and mixture reactivity. It attacks methane through the reaction of $OH+CH_4 \rightleftarrows CH_3+H_2O$. In addition, CH_2O is considered an indicator of autoignition [150]. Consequently, it is important to examine these indicators to obtain a better insight into the combustion characteristics of this biofuel mixture. It can be observed in Fig 4.19 (a) that the increasing volume of methane in biogas (BXS25) is associated with a decrease in OH concentration and an increase in CH_2O concentration. Which indicates an improvement of autoignition and a lack of heat release. Here OH is mainly produced from hydrogen which is kept constant in this case (BXS25), when CH_4 increases it consumes OH for its depletion which explains the reduction of OH with augmentation of CH_4. While OH mole fraction peaks at maximum flame temperature (Fig 4.19), the CH_2O is formed from the axis and decreases since its formation completely depends on methane through the reactions $OH+CH_4 \rightleftarrows CH_3+H_2O$ and $CH_3+O \rightleftarrows CH_2O+H$. When hydrogen is increased in syngas (B25SX) Fig 4.19 (b), OH mole fraction values are very close to each other for different hydrogen volumes. In this case, methane volume is constant which explains the slight variation of OH radical with a small shift in the increasing radial direction. Regarding the radial profiles of CH_2O, it can be seen that the same behavior of Fig 4.19 (a) is conserved.

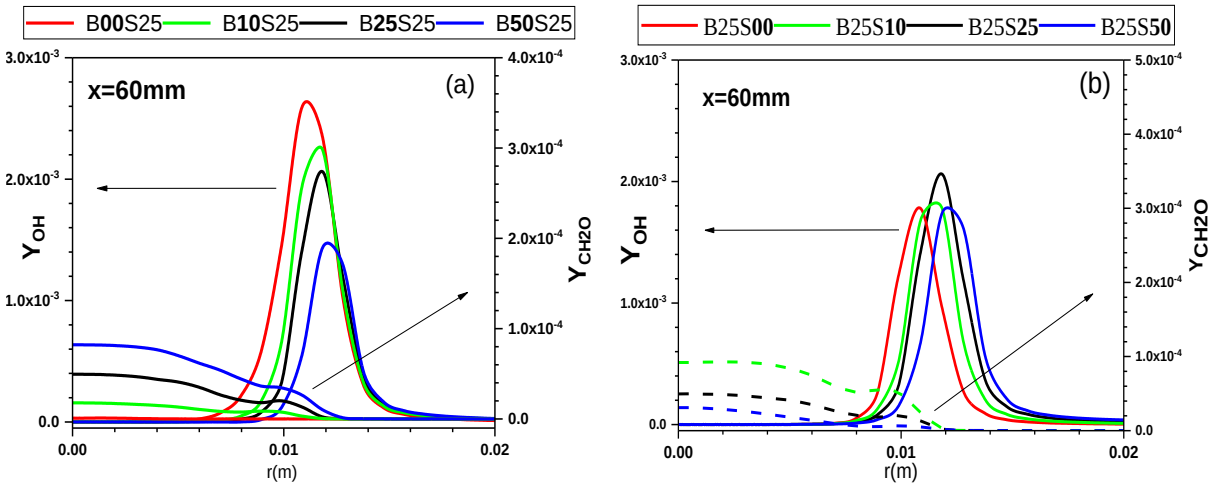

Figure 4. 19. Profiles of Y_{OH} and Y_{CH2O} in the radial direction at x = 60 mm for cases 4 to 10.

Figure 4.20 shows contours of temperature and OH mass fraction for cases 4 to 10. The upper half of the figure represents two values of iso-temperature lines namely: 1000K and 2000K, whereas, the lower half shows iso-OH mass fraction Y_{OH}=0.001. It can be noticed that when increasing methane in biogas ((BXS25), Fig 4.20(a)), the iso-temperature lines expand upstream mostly in the radial direction and flame volume is increased which can be beneficial for processes involving flame volume such as radiation. Moreover, OH isolines move away from the axis. On the other hand, when hydrogen is added to syngas (B25SX, Fig. 4.20 (b)), expansion is recorded in both directions especially for the isoline 2000K in the axial direction. This behavior gives an idea about how hydrogen addition increases mixture reactivity and fixes flame lift stabilization issues. Relatively slight variations are presented for OH isoline.

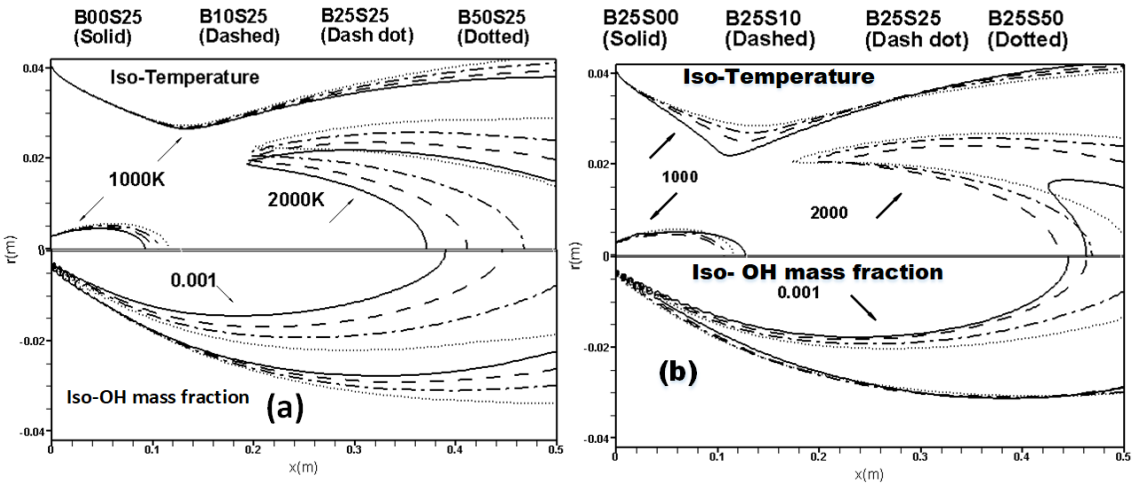

Figure 4. 20. Isolines of temperature (upper half) Y_{OH} (lower half) for: (a) cases 4 to 7 and (b) cases 7 to 10.

The NO species is a toxic emission and should be minimized, the Figure 4. 21 Shows the NO mass fraction fields for different mixtures. It can be seen that NO globally increases with increasing hydrogen and particularly methane. Furthermore, the NO is formed downstream the

jet at the high temperature regions. In the MILD region in the vicinity of the jet, it can be seen that NO production in negligeable especially for the mixture B25S00. In Fig. 4.22(a), it can be observed that the NO mass fraction production in the MILD region is very sensitive to temperature variation; since temperature exhibits a slight decrease with methane volume; then, the NO shows a reduction when methane is added to the mixture. The maximum NO mass fraction varies from 18 ppm for B00S25 to 15.3 ppm for B50S25.

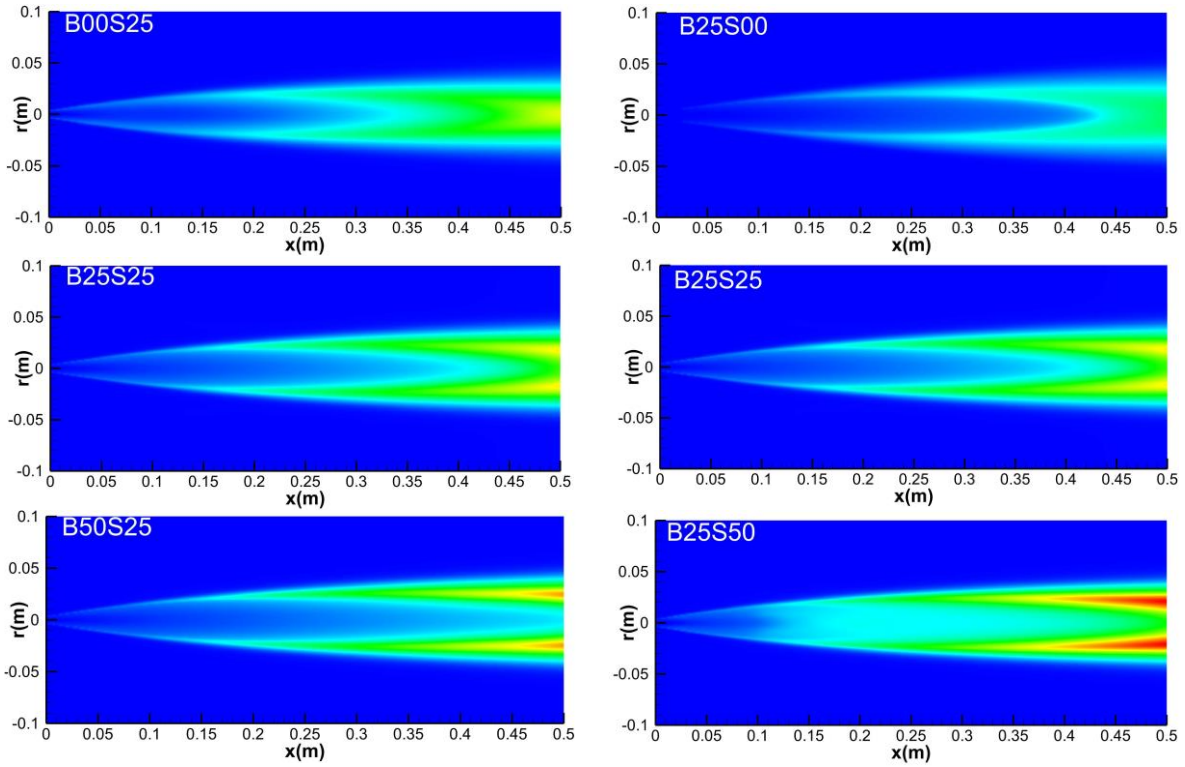

Figure 4. 21 : NO mass fraction fields for BXS25 and B25SX mixtures.

Figure 4.22 shows the mass fraction of combustion products namely: Y_{CO2}, Y_{H2O}, $Y_{CO,}$ and Y_{NO} in the radial direction at location x=60mm. It can be seen that when increasing methane volume in biogas, H_2O mass fraction decreased and shifted towards the hot oxidizer stream where it peaks after flame front position. The formation of H_2O indicates the termination of the combustion process. Moreover, it can be noticed that when methane volume augments in the mixture, CO_2 decreases slowly along the radial direction compared to CO profiles. After the flame front, shown by maximum temperature, it can be seen that CO recombines to form CO_2.

In Figure 4.22 (b), the same species (Y_{CO2}, Y_{H2O}, $Y_{CO,}$ and Y_{NO}) are presented (cases 7 to 10), when increasing hydrogen volume from 0% to 50%, H_2O mass fraction increases significantly compared to the previous case (BXS25) because its formation depends directly on

hydrogen volume. Furthermore, it can be observed that when hydrogen volume increases in the fuel mixture, CO_2 decreases slowly along the radial direction compared to CO profiles. After the flame front, shown by maximum temperature, it can be seen that CO recombines to form CO_2.

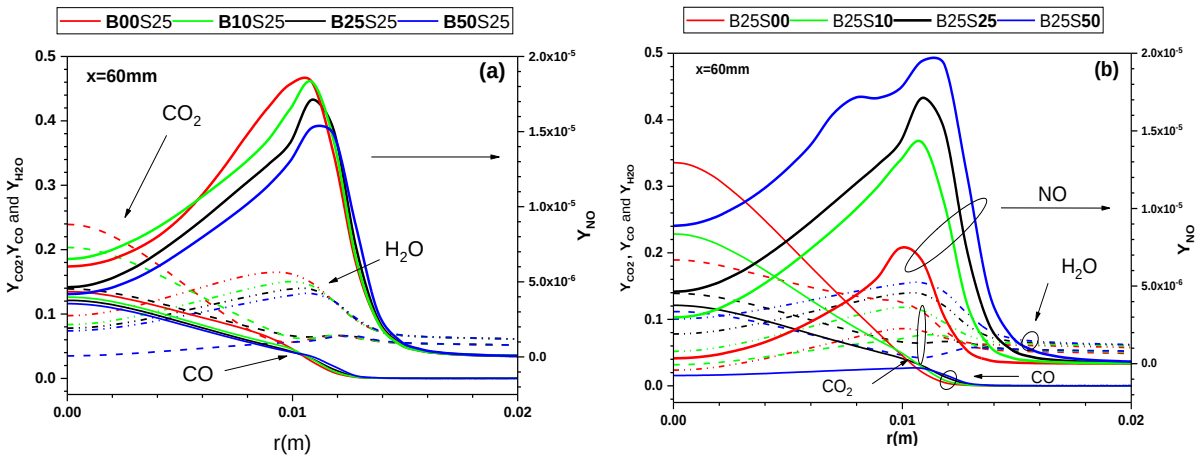

Figure 4. 22 : Profile Y_{H2O}, Y_{CO2}, $Y_{CO,}$ and Y_{NO} in the radial direction at x = 60 mm for cases 4 to 10 of Table 3.

When hydrogen increases (B25SX), the NO profiles show opposite trends comparatively to BXS25 cases. As said before, NO species is directly linked to temperature variation; consequently, when hydrogen increases in the mixture, NO species increases too. Maximum NO production is recorded for the mixture B25S50 with 19.7 ppm while the minimum value is 7.5 ppm for the B25S00 mixture.

To deeply investigate NO formation sources, the Rate of Production (ROP) of important reactions in different NO production routes are presented in Fig 4.23 (a, b, and c) for the mean composition B25S25 at section x=60 mm. Then axial NO emission index [117](EINO) is shown. Since the fuel contains a significant volume of hydrogen, it can be seen that the dominant production mechanism is NNH route followed by prompt, thermal, and N_2O intermediate one, these results are consistent with [151]. The axial variation of the EINO, Fig 4.23 (d), clearly confirms this order. From Figures 4.23 (a, b, and c), the maximum reaction rate is 42.1 10^{-5} kmol/m^{3}s for NNH, while maximums of prompt, thermal, and N_2O routes are respectively 2.34 10^{-5}, 1.57 10^{-5} and 2.34 10^{-5} kmol/m^{3}s. In summary, the most significant path is NNH through $N_2 \Rightarrow NNH \Rightarrow NO$ [152]. Despite these production paths, it can be observed that NO production is very low compared to conventional combustion Fig 4.23(d), which makes the MILD combustion of biofuels an attractive alternative. The main reactions through four NO formation routes are listed in Table 4.6

Table 4. 7: Main reactions routes of NO formation.

Route		Reaction	
Thermal	**R178 N_2+O⇄N+NO**	**R179 N+O_2⇄NO+O**	**R180 N+OH⇄NO+H**
Prompt	**R180 N+OH⇄NO+H**	**R191 N+H_2⇄NH+H**	**R220 NCO+O⇄CN+O_2**
	R222 HCO+O⇄NO+CO	**R223 NCO+Hv⇄NH+CO**	**R230 HCN+M⇄CN+H+M**
	R231 HCB+O⇄NCO+H	**R233 CN+H⇄HCN**	**R239 C+N_2⇄CN+N**
	R240 CH+N_2⇄HCN+N	**R242 CH_2+N_2⇄HCN+NH**	**R243 CH(S)+N_2⇄NH+HCN**
N_2O-intermediate	**R181 N_2+O_2⇄N_2O+O**	**R182 N_2O+O⇄2NO**	**R183 N_2+OH⇄N_2O+H**
	R184 N_2+HO_2⇄N_2O+OH	**R185 N_2+O(+M) ⇄N_2O(+M)**	**R190 NH+O⇄NO+H**
	R199 NH+NO⇄N_2O+H	**R222 NCO+O⇄NO+CO**	**R224 NO+H+CO⇄NCO+OH**
	R226 NCO+O_2⇄NO+CO_2		
NNH	**R190 NH+O⇄NO+H**	**R191 NH+H⇄N+H_2**	**R192 NH+OH⇄HNO+H**
	R193 NH+OH⇄N+H_2O	**R194 NH+O_2⇄HNO+O**	**R195 NH+O_2⇄NO+OH**
	R196 NH+N⇄N_2+H	**R197 NH+H_2O⇄HNO+O**	**R198 NH+NO⇄N_2+OH**
	R199 NH+NO⇄N_2O+H	**R204 NNH⇄N_2+H**	**R205 NNH+M⇄N_2+H+M**
	R206 NNH+O_2⇄HO_2+N_2	**R207 NNH+O⇄OH+N_2**	**R208 NNH+O⇄NH+NO**
	R209 NNH+H⇄H_2+N_2	**R210 NNH+OH⇄H_2O+N**	**R211 NNH+CH_3⇄CH_4+N_2**
	R212 H+NO+M⇄HNO+M	**R213 HNO+O⇄NO+OH**	**R214 HNO+H⇄H_2+NO**
NO-rebuming	**R183 N_2+OH⇄N_2O+H**	**R196 N_2+H⇄BH+N**	**R198 NH+NO⇄N_2+OH**
	R199 NH+NO⇄N_2O+H	**R212 H+NO+M⇄HNO+M**	**R218 CN+OH⇄NCO+H**
	R220 NCO+O⇄CN+O_2	**R223 NCO+H⇄NH+CO**	**R229 N_2+CO_2⇄NCO+NO**
	R231 NCO+H⇄HCN+O	**R232 NH+CO⇄HCN+O**	**R233 HCN+O⇄CN+OH**
	R234 HCN+OH⇄HOCN+H	**R235 HCN+OH⇄HNCO+H**	**R236 HCN+OH⇄NH_2+CO**
	R244 CN+O⇄C+NO	**R245 C+NO+CO+N**	**R246 HCN+O⇄CH+NO**
	R247 CH+NO⇄H+NCO	**R248 B+HCO⇄CH+NO**	**R249 CH_2+NO⇄H+HNCO**
	R250 CH_2+NO⇄OH+HCN	**R251 CH_2+NO⇄H+HCNO**	**R252 CH_2(S)+NO⇄H+HNCO**
	R253 CH_2(S)+NO⇄OH+HCN	**R254 CH_2(S)+NO⇄H+HCNO**	**R255 CH_3+NO⇄HCN+H_2O**
	R256 CH_3+NO⇄H_2CN+OH	**R274 HCCO+NO⇄HCNO+CO**	

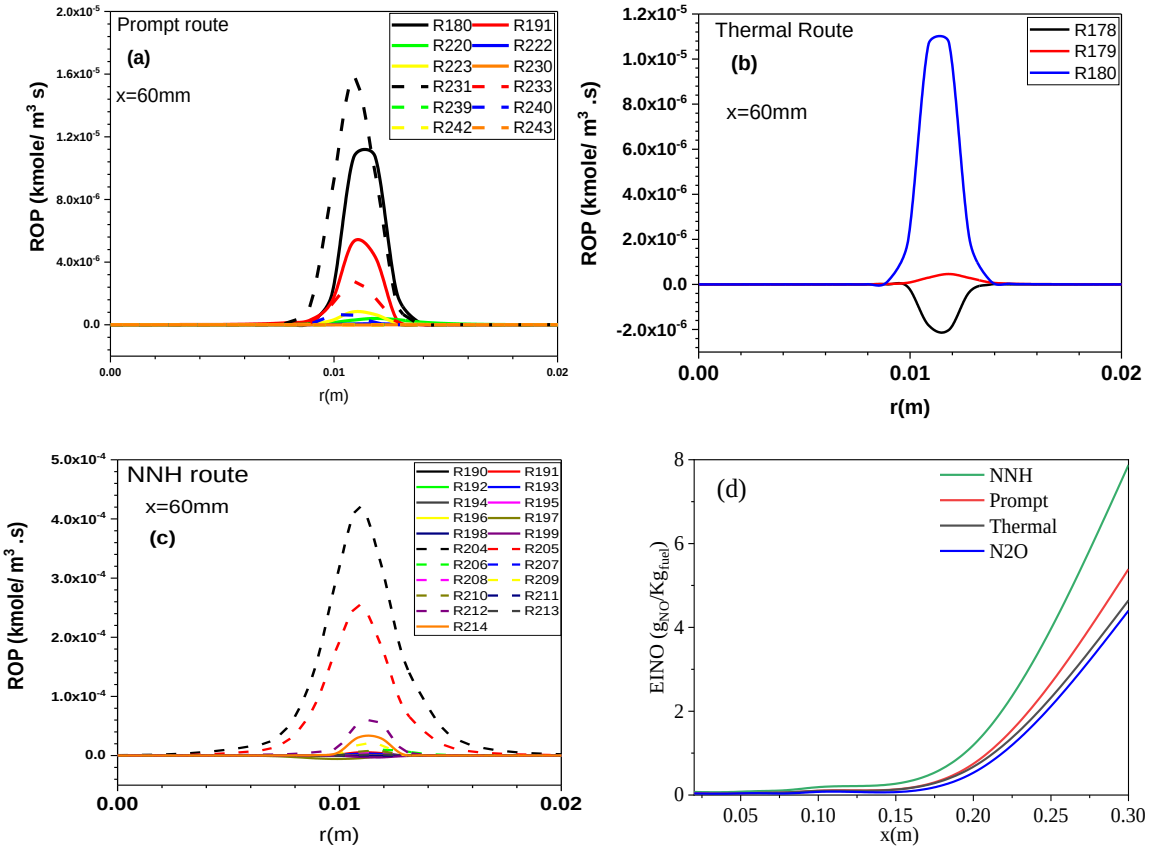

Figure 4. 23: NO production routes: a), b) and c) Radial profiles of reaction rates at x=60 mm, and d) Contribution of routes in axial EINO.

4.2.2 Effect of co-flow temperature on the flame structure

The oxidizer temperature is crucial in MILD combustion, it is a key to obtain and preserve MILD regime. Effect of co-flow temperature on the distribution of temperature, NO, H_2O, and OH mass fraction is demonstrated for four temperature values (cases 7,11,12, and 13 in Tables 4.6 and 4.7).

Table 4. 8: Oxidizer temperature variation

N°	ID	Oxidizer T(K)
11	B25S25(1500)	1500
12	B25S25(1700)	1700
13	B25S25(1900)	1900
• Oxidizer: X_{O2}=0.09, X_{H2O}=0.065, • X_{CO2}=0.055, X_{N2}=0.79. • Fuel velocity: 58.75m/s.		

The co-flow temperature effect on the combustion fields of temperature and NO mass fraction is shown by the Figure 4. 24. The mean mixture B25S25 is used, similar behaviors of temperature fields are depicted, high co-flow temperatures seem to give long flame jets. On the

other hand, elevated co-flow temperature produces more NO emission. Also, low combustion temperature which warrants MILD regime are located in the vicinity of the burner.

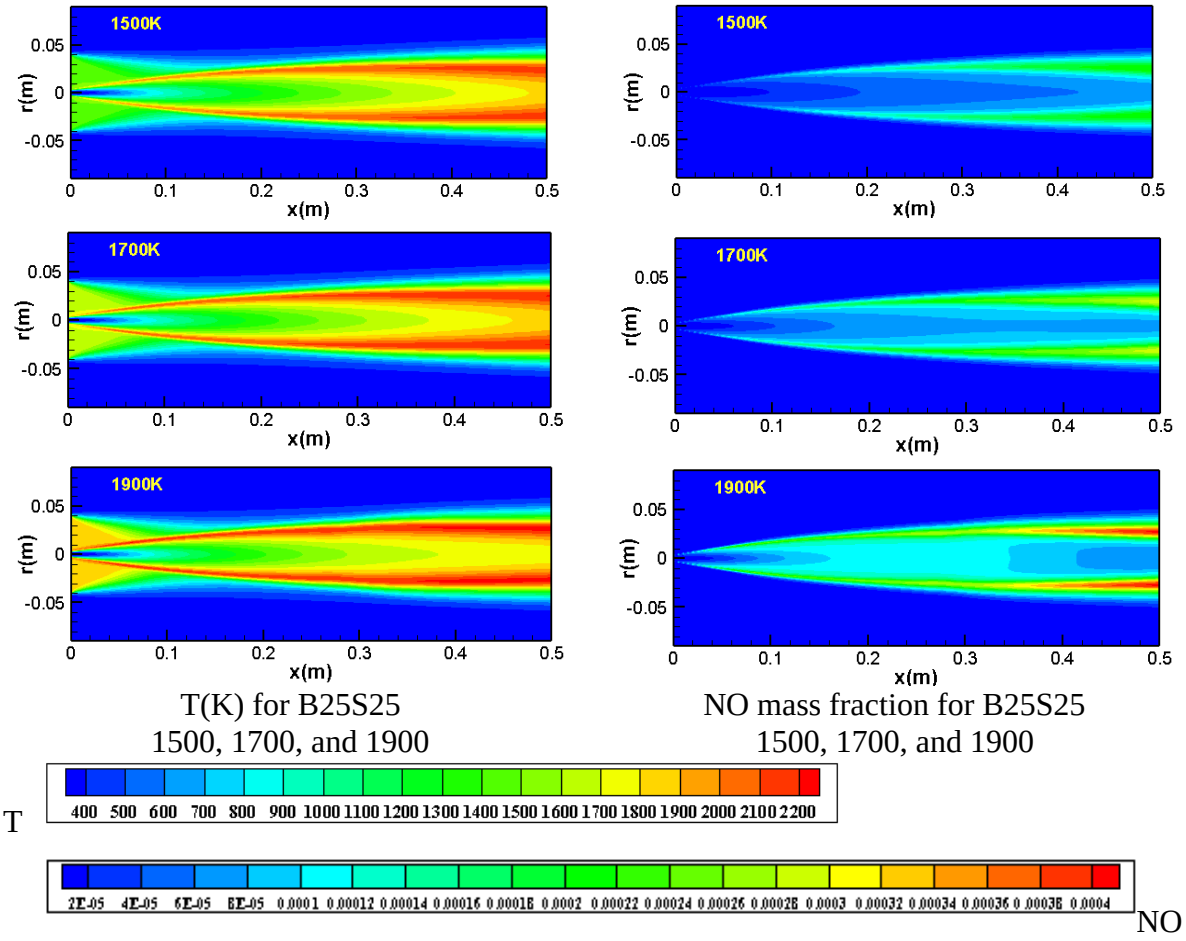

Figure 4. 24: Temperature and NO mass fraction fields for B25S25 at different co-flow temperatures.

More details about the effect of co-flow temperature are obtained from the Fig 4.25 (a) which shows radial profiles of temperature and NO concentration at both locations z=30mm and 60mm for the mixture B25S25. It can be observed that the temperature peak increases with the augmentation of co-flow temperature. The limits of co-flow injection temperatures are T_{cf}=1300K, which yields a maximum flame temperature of 1826K, and T_{cf}=1900K which gives 2246K. Both temperatures are recorded at axial location x=60mm and radial one r=0.011m. For all injection temperatures, it can be seen that the increase in temperature by combustion didn't exceed mixture autoignition temperature, this prevails the MILD combustion regime at this location.

When the co-flow temperature augments from 1300K to 1900K, the maximum NO mass fraction increases thirteen times from 17.4 ppm to 231 ppm. The trend of NO concentration is

in line with the results of [151], where they explained this increase by the enhancement in the chemical reaction that contributes to the formation of both species NNH and HCN.

Figure 4.25(b) shows both H_2O and OH species mole fraction variation along the radial direction for the mixture B25S25 at both locations x=30 and 60mm, for the different temperatures of co-flow (cases 7,11,12 and 13 of Table 4.7). Despite values, it can be seen that H_2O and OH profiles are similar for both locations and co-flow injection temperatures. The maximum value of OH is situated at the same position of temperature peak. Effect of co-flow temperature on H_2O concentration is not significant, since it is a stable species, while OH concentration doubles from 2.03 10^{-3} to 4.68 10^{-3} while T_{cf} ranges from1300K to 1900K (at location x=60mm).

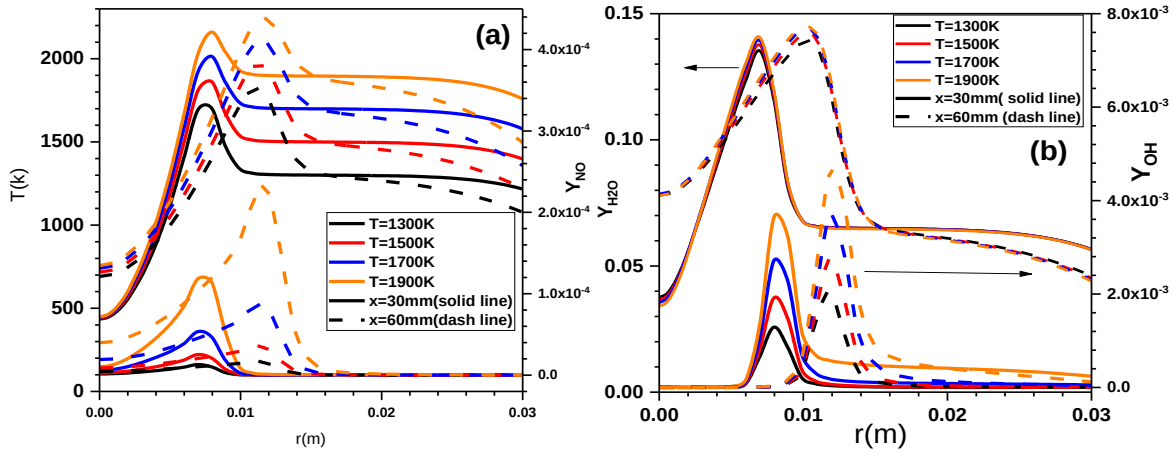

Figure 4. 25: Radial profiles of temperature, Y_{NO} $Y_{H2O,}$ and Y_{OH} at x=60mm cases 7,11,12, and 13 of Table 4.

4.2.3 Effect of fuel jet Reynolds number on the flame structure

The effect of flow field dynamics on the flame structure has been studied by changing the Reynolds number of fuel stream from 10,000 to 20,000 for mean composition B25S25.

Table 4. 9: Fuel Reynolds number variation

N°	ID	Fuel jet Re
14	B25S25(Re1)	20,000
15	B25S25(Re2)	15,000
16	B25S25(Re3)	10,000
• Oxidizer: X_{O2}=0.09, X_{H2O}=0.065, X_{CO2}=0.055, X_{N2}=0.79.		

Figure 4.26 shows radial profiles of temperature for both locations x= 30 and 60 mm for three Reynolds numbers namely: Re=10,000. 15,000 and 20,000. It can be seen that when increasing Reynolds number from 10,000 to 20,000 the temperature was not affected significantly, as the maximum reduction in temperature is ΔT =20K. This reduction is due to flow residence time which is reduced by increasing Reynolds number. Consequently, chemical time is reduced resulting in unburned species and then reduced temperature.

Figure 4.27 (a) represents the mixture fraction and NO mass fraction for both locations x=30 mm and 60 mm. The mixture fraction increases because additional fuel is injected when the fuel jet Reynolds number is increased.

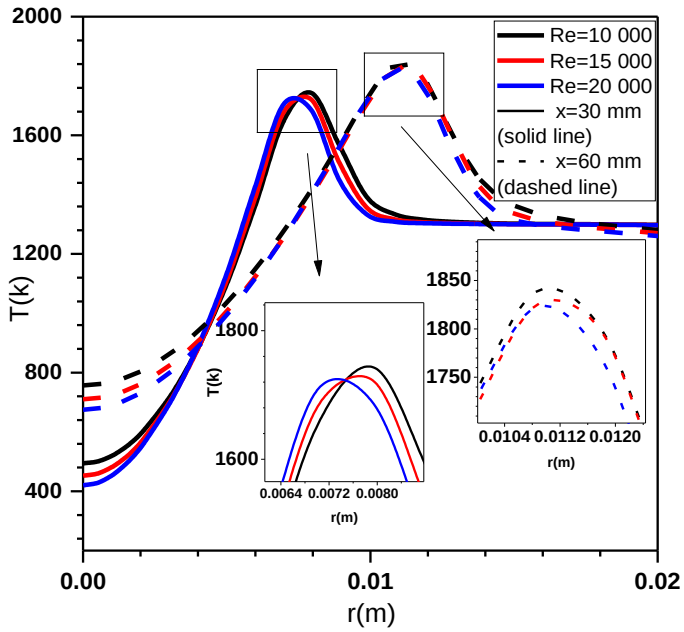

Figure 4. 26: Radial profiles of temperature at x=60mm for cases 14,15 and 16 of Table 5.

The NO species is very sensitive to temperature and hence decreased by velocity or Reynolds number augmentation. Also, stable species are reduced by incomplete combustion (which is enhanced by Reynolds number); whereas, radical or unburnt species are enhanced. This behavior can be seen in Fig. 4.27 (b) which shows radial profiles of H_2O and OH.

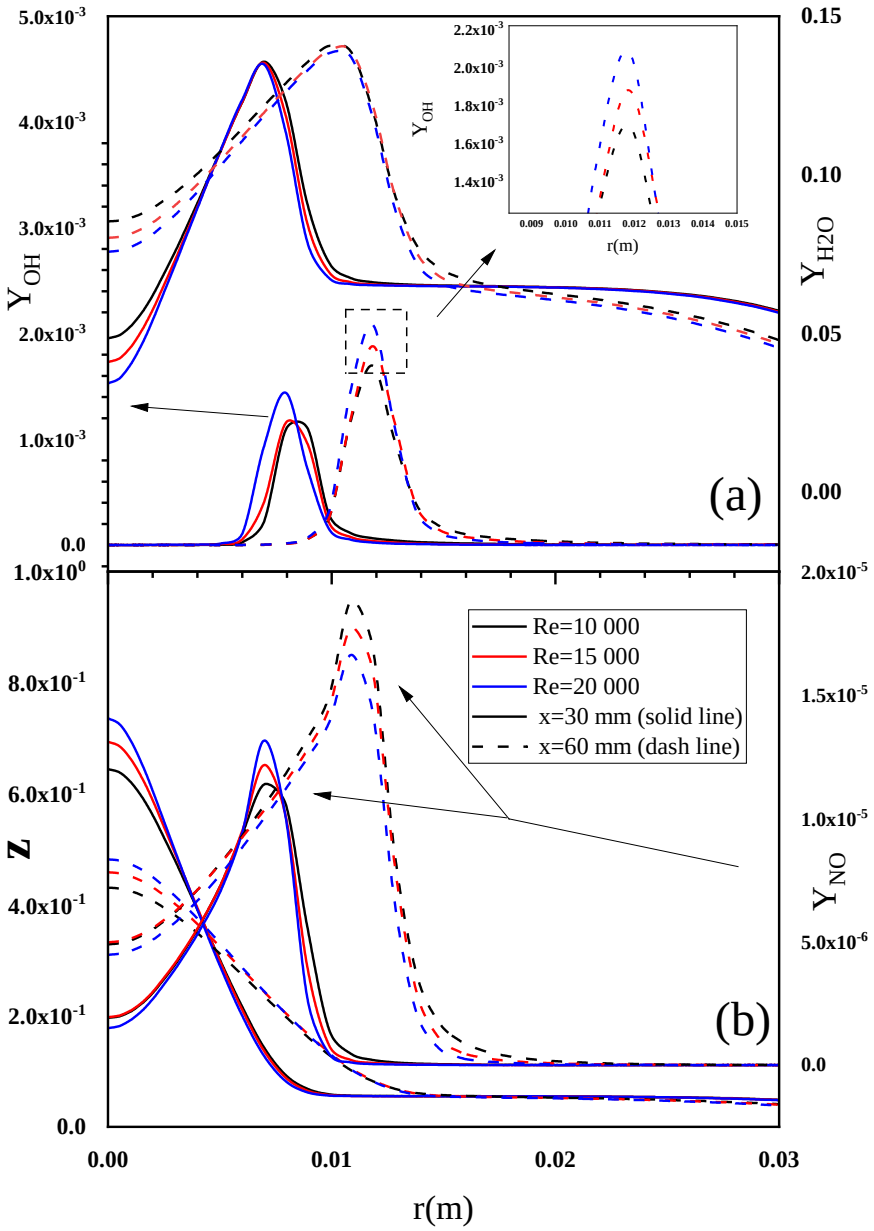

Figure 4. 27: (a) radial profiles of Y_{OH} and Y_{H2O} , (b) Radial profiles of z and YNO at x=60mm for cases 14,15, and 16 of Table 5.

4.2.4 Effect of oxygen concentration on the flame structure

Oxygen content in oxidizer is one of the two keys to sustain MILD regime. In this context, the effect of oxygen is studied for the mean mixture B25S25, four volumes of oxygen are adopted, namely: 2%, 6%, 9%, and 12%, Table 4.9.

Table 4. 10: Oxygen volume in oxidizer

N°	ID	O_2 vol.%	N_2 vol.%
17	B25S25(Ox3)	3	85
18	B25S25(Ox6)	6	82
19	B25S25(Ox9)	9	79
20	B25S25(Ox12)	12	76
• Oxidizer: X_{H2O}=0.065, X_{CO2}=0.055. • Fuel velocity: 58.75m/s.			

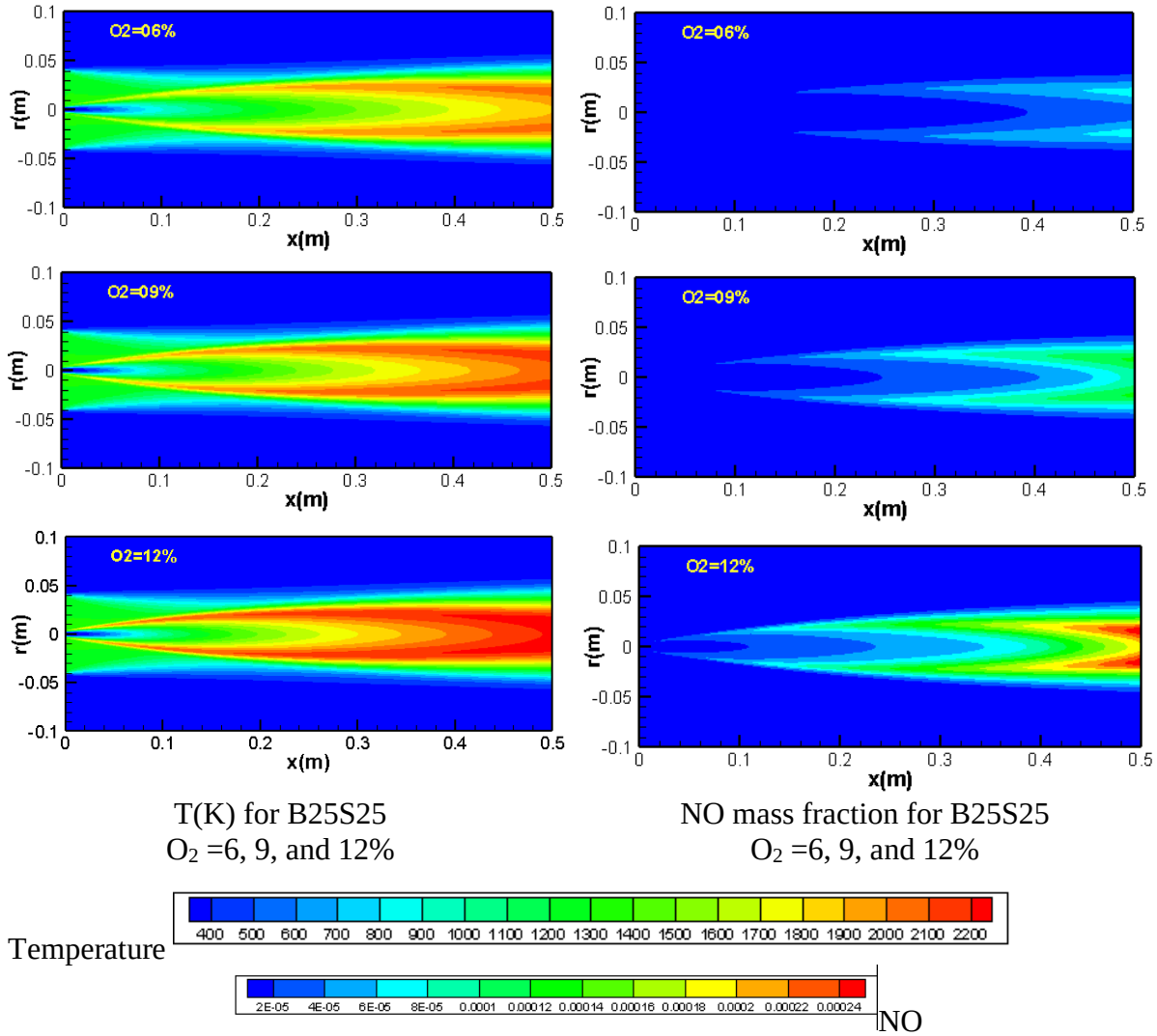

T(K) for B25S25
O_2 =6, 9, and 12%

NO mass fraction for B25S25
O_2 =6, 9, and 12%

Figure 4. 28: Temperature and NO mass fraction fields for B25S25 at different oxygen concentrations.

The Figure 4. 28 shows the effect of oxygen addition to the oxidizer on the combustion temperature and NO mass fraction fields. It can be seen that oxygen increases combustion temperature significantly since local equivalence ratio moves toward the unity. Besides, the flame shifts near the burner which shrinks the MILD combustion region. For the NO emission, it can be observed that the best oxygen content displayed is 6%, since NO concentration is nearly zero in the MILD region which is the largest.

To get more understanding in the MILD region, Figure 4.29 illustrates the effect of oxygen concentration in hot co-flow on the temperature, H_2O, OH, and NO mass fractions at both locations x=30 and 60mm for biogas-syngas mixture B25S25. The comparison among four different oxygen levels is conducted (cases 17 to 20 Table 4.9) with constant velocity u=58.75m/s and co-flow temperature of 1300K.

It can be seen from Fig 4.29 (a) that temperature and OH mass fraction is significantly increased by oxygen concentration augmentation in the oxidizer stream. For each oxygen volume, temperature and OH profiles share the same peak positions. Oxygen increase shifts slightly maximums of temperature and OH to the fuel jet side since local equivalence ratio has decreased with oxygen addition. From Fig 4.29 (b), as said before, the NO species is linked to temperature level, which explains the significant increase of NO mass fraction with oxygen. The NO mass fraction maximum increases from 8.5 ppm for 3% of oxygen in oxidizer to 40 ppm for 12% of oxygen volume. Furthermore, the H_2O mass fraction is highly increased by oxygen volume in the oxidizer stream. In MILD combustion, the lack of oxygen reduces temperature and complete combustion species; whereas, it enhances unburnt species. Oxygen addition enhances temperature and complete combustion products such as H_2O and CO_2.

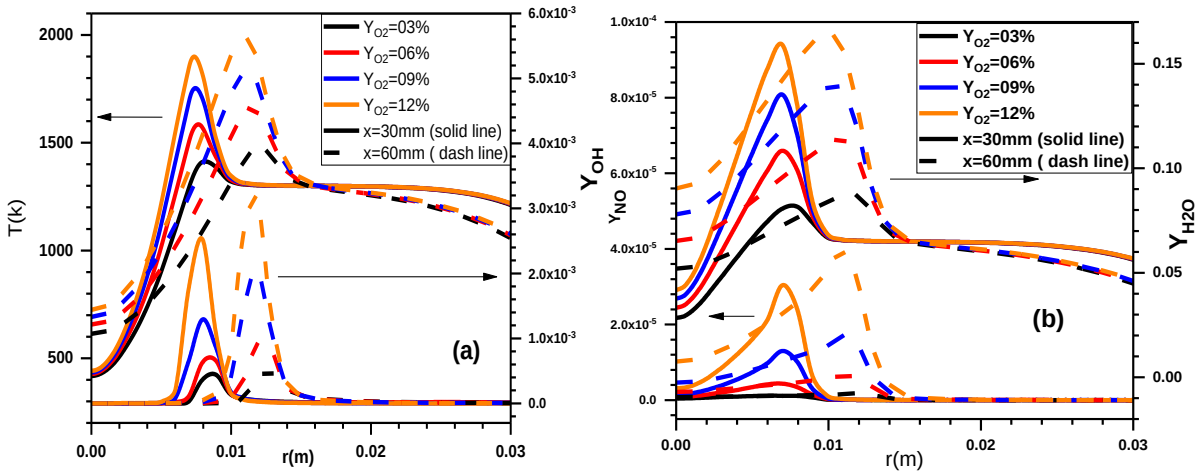

Figure 4. 29: Radial profiles of temperature, Y_{NO}, Y_{H2O} and Y_{H2O} at x=60mm for cases 17 to 20.

4.3 Conclusion

The numerical procedure was validated by three geometries, numerical data was acceptably close to the experimental one. Then, the jet in hot co-flow (JHC) burner is adopted for the analysis of the flame structure and emissions. The main results are found from the variation of several parameters in the turbulent MILD combustion of the mixture biogas-syngas ($CH_4/CO_2/H_2/CO$). Effects of mixture composition, hot co-flow temperature, fuel jet Reynolds number and oxygen concentration on flame structure and emissions were considered. The Reynolds-Averaged Navier-Stokes (RANS) and the Eddy Dissipation Concept (EDC) combustion model with detailed chemical mechanism GRI-Mech 2.11 were used for the simulation. The main conclusions that can be drawn are:

1. The temperature augmentation is more significant when hydrogen volume increases in the fuel mixture, on the other hand, methane addition has a negligible effect. Moreover, both methane and hydrogen addition improve autoignition.
2. Methane addition to the mixture increases flame volume, which can be beneficial for processes involving flame radiation. Whereas, hydrogen addition increases mixture reactivity and local flame speed which fixes flame liftoff issues.
3. Coflow temperature augmentation preserves the MILD combustion regime but produces more NO emissions. On the other hand, fuel injection Reynolds number increase reduces slightly temperature and significantly NO emissions.
4. The NO production shows a reduction when methane is added to the biogas; whereas, it increases with hydrogen augmentation in syngas.
5. The dominant NO production mechanism is NNH followed by prompt, thermal, and N_2O intermediate one. NNH and N_2O paths are enabled in a hot and less rich region whereas prompt route is activated in the relatively cold and rich zone

CONCLUSION

The main objective of this thesis is to examine the pertinency of the turbulent MILD combustion of biofuels in industrial devices, namely burners used in gas turbines combustion chambers. For this, the effect of chemical composition, injection temperatures, and dynamic field on the flame structure and emissions is studied. The used numerical procedure showed its capability to solve complicated interactions between flow dynamics, heat transfer and chemical kinetics. The calculations are based on the non-premixed turbulent MILD combustion of the biogas syngas in the Jet in Hot Co-flow burner (JHC). The biogas-syngas blend is modeled by the mixture $CH_4/CO_2/H_2/CO$, and the chemical kinetics by the detailed mechanism Gri.2.0. Interaction between turbulence and combustion is handled by the EDC model. Effects of mixture ($CH_4/CO_2/H_2/CO$) composition, hot coflow temperature, fuel jet Reynolds number and oxygen concentration on the flame structure and emissions are considered. The results showed that the temperature augmentation is more significant when hydrogen volume increases in the fuel mixture, on the other hand methane addition has a negligible effect. This means that the quality of biogas used didn't matter in contrast to that of syngas. Moreover, both methane and hydrogen addition improve autoignition of the mixture, which implies using of high-quality biogas or syngas in cases of bad ignition. Methane addition to the mixture increases flame volume, which can be beneficial for processes involving flame radiation such as burners in glass or cement plants. Whereas, hydrogen addition increases mixture reactivity and local flame speed; this can fix flame liftoff issues in high velocity burners and bypass the use of bluff-body configuration. It is observed that oxygen increase in the oxidizer increases all parameters since it enhances combustion reaction. To preserve MILD regime, it is crucial to reduce oxygen at the lower limit of the combustion stability. The increase of co-flow temperature preserves MILD combustion regime but produces more NO emissions. On the other hand, fuel injection

Reynolds number increase reduces slightly temperature and significantly NO emissions. For the NOx formation, The NO production shows a reduction when methane is added to the biogas; whereas, it increases with hydrogen augmentation in syngas. The dominant NO production mechanism is NNH followed by prompt, thermal and N_2O intermediate one. NNH and N_2O paths are enabled in a hot and less rich region whereas prompt route is activated in the relatively cold and rich zone.

Future work can be focused on the whole combustion chamber using the same modeling and introducing the flame soot issue through advanced chemical mechanisms which needs important computation means.

References

[1] Office of Energy Markets and End Use, *Annual Energy Review 2007*. 2008.

[2] Global Change Data Lap, "Our World In Data," *Life Expectancy*, 2016. https://ourworldindata.org/ (accessed Jul. 25, 2021).

[3] M. Ritchie, Hannah; Roser, "Fossil Fuels; Our world in data," *Our world in data*. p., 2018, Accessed: Sep. 19, 2021. [Online]. Available: https://ourworldindata.org/fossil-fuels.

[4] J. Song *et al.*, "Acute effects of ambient air pollution on outpatient children with respiratory diseases in Shijiazhuang, China," *BMC Pulm. Med.*, vol. 18, no. 1, pp. 1–10, 2018.

[5] H. Ritchie and M. Roser, "Air Pollution - Our World in Data," *OurWorldInData*, 2020. https://ourworldindata.org/air-pollution (accessed Sep. 19, 2021).

[6] "Fichier:Health effects of pollution.svg — Wikipédia." https://fr.m.wikipedia.org/wiki/Fichier:Health_effects_of_pollution.svg (accessed Sep. 19, 2021).

[7] J. B. Holm-Nielsen, T. Al Seadi, and P. Oleskowicz-Popiel, "The future of anaerobic digestion and biogas utilization," *Bioresour. Technol.*, vol. 100, no. 22, pp. 5478–5484, 2009.

[8] S. Daniele, P. Jansohn, J. Mantzaras, and K. Boulouchos, "Turbulent flame speed for syngas at gas turbine relevant conditions," *Proc. Combust. Inst.*, vol. 33, no. 2, pp. 2937–2944, 2011, doi: 10.1016/j.proci.2010.05.057.

[9] A. L. Boehman and O. Le Corre, "Combustion of syngas in internal combustion engines," *Combust. Sci. Technol.*, vol. 180, no. 6, pp. 1193–1206, 2008, doi: 10.1080/00102200801963417.

[10] P. Verma, Kr., L. Saxena, and R. Gupta, "Biogas : Its Application and Production," *Innov. Res. Concept*, vol. 1, no. 9, pp. 26–28, 2016.

[11] J. Park, D. Hwang, J. Choi, K. Lee, S. Keel, and S. Shim, "Chemical effects of CO2 addition to oxidizer and fuel streams on flame structure in H2–O2 counterflow diffusion flames," *Int. J. energy Res.*, vol. 27, no. 13, pp. 1205–1220, 2003.

[12] A. Mameri, F. Tabet, and A. Hadef, "MILD combustion of hydrogenated biogas under several operating conditions in an opposed jet configuration," *Int. J. Hydrogen Energy*, vol. 43, no. 6, pp. 3566–3576, 2018, doi: 10.1016/j.ijhydene.2017.04.273.

[13] T. Leung and I. Wierzba, "The effect of hydrogen addition on biogas non-premixed jet

flame stability in a co-flowing air stream," *Int. J. Hydrogen Energy*, vol. 33, no. 14, pp. 3856–3862, 2008.

[14] H. S. Zhen, C. W. Leung, and C. S. Cheung, "Effects of hydrogen addition on the characteristics of a biogas diffusion flame," *Int. J. Hydrogen Energy*, vol. 38, no. 16, pp. 6874–6881, 2013.

[15] A. Mameri, S. Boussetla, R. Belalmi, and Z. Aouachria, "Combustion characterization of the mixtures biogas-syngas, strain rate and ambient pressure effects," *Int. J. Hydrogen Energy*, vol. 44, no. 39, pp. 22478–22491, 2019, doi: 10.1016/j.ijhydene.2019.05.142.

[16] R. Zouagri, A. Mameri, F. Tabet, and A. Hadef, "Characterization of the combustion of the mixtures biogas-syngas at high strain rates," *Fuel*, vol. 271, no. February, 2020, doi: 10.1016/j.fuel.2020.117580.

[17] G. Maschio, A. Lucchesi, and G. Stoppato, "Production of syngas from biomass," *Bioresour. Technol.*, vol. 48, no. 2, pp. 119–126, 1994.

[18] J. Caudal, "Simulation numérique du reformage autothermique du méthane." 2013.

[19] A. F. Colorado, B. A. Herrera, and A. A. Amell, "Performance of a Flameless combustion furnace using biogas and natural gas," *Bioresour. Technol.*, vol. 101, no. 7, pp. 2443–2449, 2010, doi: 10.1016/j.biortech.2009.11.003.

[20] G. Sarras, Y. Mahmoudi, L. D. Arteaga Mendez, E. H. Van Veen, M. J. Tummers, and D. J. E. M. Roekaerts, "Modeling of turbulent natural gas and biogas flames of the delft jet-in-hot-coflow burner: Effects of coflow temperature, fuel temperature and fuel composition on the flame lift-off height," *Flow, Turbul. Combust.*, vol. 93, no. 4, pp. 607–635, 2014, doi: 10.1007/s10494-014-9555-3.

[21] M. Sahin, "Combustion characteristics of various biogas flames under reduced oxygen concentration conditions," *Energy Sources, Part A Recover. Util. Environ. Eff.*, vol. 41, no. 19, pp. 2415–2427, 2019, doi: 10.1080/15567036.2019.1601796.

[22] M. Huang, Z. Zhang, W. Shao, Y. Xiong, F. Lei, and Y. Xiao, "MILD combustion for hydrogen and syngas at elevated pressures," *J. Therm. Sci.*, vol. 23, no. 1, pp. 96–102, 2014, doi: 10.1007/s11630-014-0682-x.

[23] M. M. Huang *et al.*, "Effect of fuel injection velocity on MILD combustion of syngas in axially-staged combustor," *Appl. Therm. Eng.*, vol. 66, no. 1–2, pp. 485–492, 2014, doi: 10.1016/j.applthermaleng.2014.02.033.

[24] A. Mardani and H. Karimi Motaalegh Mahalegi, "Hydrogen enrichment of methane and syngas for MILD combustion," *Int. J. Hydrogen Energy*, vol. 44, no. 18, pp. 9423–

9437, 2019, doi: 10.1016/j.ijhydene.2019.02.072.

[25] A. Chinnici, G. J. Nathan, and B. B. Dally, “Experimental and numerical study of the influence of syngas composition on the performance and stability of a laboratory-scale MILD combustor,” *Exp. Therm. Fluid Sci.*, vol. 115, no. October 2019, p. 110083, 2020, doi: 10.1016/j.expthermflusci.2020.110083.

[26] M. Saha, G. Gitto, A. Chinnici, and B. B. Dally, “Comparative study of the MILD combustion characteristics of biomass and brown coal,” *Energy & Fuels*, vol. 32, no. 4, pp. 4202–4211, 2017.

[27] P. Sabia, G. Sorrentino, P. Bozza, G. Ceriello, R. Ragucci, and M. De Joannon, “Fuel and thermal load flexibility of a MILD burner,” *Proc. Combust. Inst.*, vol. 37, no. 4, pp. 4547–4554, 2019.

[28] “Anthony Marchese.” https://www.engr.colostate.edu/~marchese/abc2.html (accessed Sep. 21, 2021).

[29] K. Saeed and R. Stone, “Laminar burning velocities of propene-air mixtures at elevated temperatures and pressures,” *J. Energy Inst.*, vol. 80, no. 2, pp. 73–82, 2007, doi: 10.1179/174602207X186916.

[30] H. Amar, M. Abdelbaki, T. Fouzi, and A. Zeroual, “Effect of the addition of H2 and H2O on the polluting species in a counter-flow diffusion flame of biogas in flameless regime,” *Int. J. Hydrogen Energy*, vol. 43, no. 6, pp. 3475–3481, 2018, doi: 10.1016/j.ijhydene.2017.11.159.

[31] D. E. Giles, S. Som, and S. K. Aggarwal, “NOx emission characteristics of counterflow syngas diffusion flames with airstream dilution,” *Fuel*, vol. 85, no. 12–13, pp. 1729–1742, 2006, doi: 10.1016/j.fuel.2006.01.027.

[32] S. K. Aggarwal, D. Bongiovanni, and M. Santarelli, “Extinction of laminar diffusion flames burning the anodic syngas fuel from solid oxide fuel cell,” *Int. J. Hydrogen Energy*, vol. 40, no. 22, pp. 7214–7230, 2015, doi: 10.1016/j.ijhydene.2015.04.015.

[33] K. Safer, F. Tabet, and M. Safer, “A numerical investigation of structure and NO emissions of turbulent syngas diffusion flame in counter-flow configuration,” *Int. J. Hydrogen Energy*, vol. 41, no. 4, pp. 3208–3221, 2016, doi: 10.1016/j.ijhydene.2015.12.154.

[34] G. M. Faeth, “Swirl flows: AK Gupta, DG Lilley, and N. Syred, Abacus Press, Tunbridge Wells, England, 1984, xiii+ 475 pp, $50.00,” 1986.

[35] P. Guo, S. Zang, and B. Ge, “Technical brief: Predictions of flow field for circular-disk bluff-body stabilized flame investigated by large eddy simulation and experiments,” *J.*

Eng. gas turbines power, vol. 132, no. 5, 2010.

[36] J. P. Longwell, E. E. Frost, and M. A. Weiss, "Flame stability in bluff body recirculation zones," *Ind. Eng. Chem.*, vol. 45, no. 8, pp. 1629–1633, 1953.

[37] D. G. Lilley, "Swirl flows in combustion: a review," *AIAA J.*, vol. 15, no. 8, pp. 1063–1078, 1977.

[38] V. D. Milosavljevic, A. Taylor, and J. H. Whitelaw, "The influence of burner geometry and flow rates on the stability and symmetry of swirl-stabilized nonpremixed flames," *Combust. Flame*, vol. 80, no. 2, pp. 196–208, 1990.

[39] S. A. Beltagui and B. SA, "VANE-SWIRLED FLAMES IN FURNACES.," 1975.

[40] R. E. Charles, J. L. Emdee, L. J. Muzio, and G. S. Samuelsen, "The effect of inlet conditions on the performance and flowfield structure of a non-premixed swirl-stabilized distributed reaction," in *Symposium (International) on Combustion*, 1988, vol. 21, no. 1, pp. 1455–1461.

[41] A. K. Gupta, D. G. Lilley, and N. Syred, "Swirl flows," *Tunbridge Wells*, 1984.

[42] R.-H. Chen and J. F. Driscoll, "The role of the recirculation vortex in improving fuel-air mixing within swirling flames," in *Symposium (International) on Combustion*, 1989, vol. 22, no. 1, pp. 531–540.

[43] W. M. Roquemore, R. S. Tankin, H. H. Chiu, and S. A. Lottes, "A study of a bluff-body combustor using laser sheet lighting," *Exp. Fluids*, vol. 4, no. 4, pp. 205–213, 1986.

[44] S. Penner and F. Williams, "Recent studies on flame stabilization of premixed turbulent gases," *Appl. Mech. Rev.*, vol. 10, no. 6, pp. 229–237, 1957.

[45] B. B. Dally, A. R. Masri, R. S. Barlow, and G. J. Fiechtner, "Instantaneous and mean compositional structure of bluff-body stabilized nonpremixed flames," *Combust. Flame*, vol. 114, no. 1–2, pp. 119–148, 1998, doi: 10.1016/S0010-2180(97)00280-0.

[46] "Aerospace Mechanical and Mechatronic Engineering - The University of Sydney." https://web.aeromech.usyd.edu.au/thermofluids/bluff.php (accessed Sep. 04, 2021).

[47] B. B. Dally, D. F. Fletcher, and A. R. Masri, "Flow and mixing fields of turbulent bluff-body jets and flames," *Combust. Theory Model.*, vol. 2, no. 2, pp. 193–219, 1998, doi: 10.1088/1364-7830/2/2/006.

[48] B. Merci, E. Dick, J. Vierendeels, D. Roekaerts, and T. W. J. Peeters, "Application of a new cubic turbulence model to piloted and bluff-body diffusion flames," *Combust. Flame*, vol. 126, no. 1–2, pp. 1533–1556, 2001, doi: 10.1016/S0010-2180(01)00272-3.

[49] S. U. O. Deniz Yilmaz, "Computational modeling of hydrogen enriched non-premixed

turbulent methane air flames," *Proc. Eur. Combust. Meet.*, no. February 2015, pp. 1–6, 2005.

[50] L. Chen and F. Battaglia, "The Effects of Fuel Mixtures in Nonpremixed Combustion for a Bluff-Body Flame," *J. Energy Resour. Technol. Trans. ASME*, vol. 138, no. 2, pp. 1–9, 2016, doi: 10.1115/1.4031835.

[51] B. B. Dally, A. N. Karpetis, and R. S. Barlow, "Structure of turbulent non-premixed jet flames in a diluted hot coflow," *Proc. Combust. Inst.*, vol. 29, no. 1, pp. 1147–1154, 2002, doi: 10.1016/S1540-7489(02)80145-6.

[52] F. C. Christo and B. B. Dally, "Modeling turbulent reacting jets issuing into a hot and diluted coflow," *Combust. Flame*, vol. 142, no. 1–2, pp. 117–129, 2005, doi: 10.1016/j.combustflame.2005.03.002.

[53] J. Aminian, C. Galletti, S. Shahhosseini, and L. Tognotti, "Key modeling issues in prediction of minor species in diluted-preheated combustion conditions," *Appl. Therm. Eng.*, vol. 31, no. 16, pp. 3287–3300, 2011, doi: 10.1016/j.applthermaleng.2011.06.007.

[54] A. Mardani and S. Tabejamaat, "Effect of hydrogen on hydrogen-methane turbulent non-premixed flame under MILD condition," *Int. J. Hydrogen Energy*, vol. 35, no. 20, pp. 11324–11331, 2010, doi: 10.1016/j.ijhydene.2010.06.064.

[55] A. De, E. Oldenhof, P. Sathiah, and D. Roekaerts, "Numerical simulation of Delft-Jet-in-Hot-Coflow (DJHC) flames using the eddy dissipation concept model for turbulence-chemistry interaction," *Flow, Turbul. Combust.*, vol. 87, no. 4, pp. 537–567, 2011, doi: 10.1007/s10494-011-9337-0.

[56] S. Rahm, "Addressing Gas Turbine Fuel Flexibility Authored by :," vol. 4601, 2009.

[57] O. Sarkar, S. K. Butti, and S. V. Mohan, *Acidogenic biorefinery: Food waste valorization to biogas and platform chemicals*. Elsevier B.V., 2018.

[58] "Steam Methane Reforming - Syngas Production | Air Liquide." https://www.engineering-airliquide.com/steam-methane-reforming-syngas-production (accessed Jul. 05, 2021).

[59] D. Deublein and A. Steinhauser, *Biogas from waste and renewable resources: an introduction*. John Wiley & Sons, 2011.

[60] S. K. Khanal, *Anaerobic Biotechnology for Bioenergy Production: Principles and Applications*. 2009.

[61] Y. Sung *et al.*, "Optical non-intrusive measurements of internal recirculation zone of pulverized coal swirling flames with secondary swirl intensity," *Energy*, vol. 103, no.

x, pp. 61–74, 2016, doi: 10.1016/j.energy.2015.12.095.

[62] O. M. E. S. Khayal, “Advantages and Limitations of Biogas Technologies,” no. December, pp. 1–8, 2019, doi: 10.13140/RG.2.2.11989.58087.

[63] J. van de Loosdrecht and J. W. H. Niemantsverdriet, “5.4 synthesis gas to hydrogen, methanol, and synthetic fuels,” in *Chemical energy storage*, De Gruyter, 2012, pp. 443–458.

[64] “Steam Methane Reforming - Syngas Production | Air Liquide.” https://www.engineering-airliquide.com/steam-methane-reforming-syngas-production (accessed Sep. 21, 2021).

[65] R. Ma, B. Xu, and X. Zhang, “Catalytic partial oxidation (CPOX) of natural gas and renewable hydrocarbons/oxygenated hydrocarbons—A review,” *Catal. Today*, vol. 338, no. May, pp. 18–30, 2019, doi: 10.1016/j.cattod.2019.06.025.

[66] M. Mosinska and M. I. Szynkowska, “Oxy-Steam Reforming of Natural Gas on Ni,” 2020.

[67] C. Paper, Z. Kish, and Q. Sciencetech, “Pure Steam Reforming of Municipal Solid Waste,” no. September, 2016, doi: 10.13140/2.1.4101.8247.

[68] M. Katsuki and T. Hasegawa, “The science and technology of combustion in highly preheated air,” in *Symposium (International) on combustion*, 1998, vol. 27, no. 2, pp. 3135–3146.

[69] A. Milani and A. Saponaro, “IFRF Combustion Journal Article Number 200101, February 2001.”

[70] A. Milani and A. Saponaro, “Diluted combustion technologies,” *IFRF - Combust. J.*, vol. 19, no. 200101, pp. 391–395, 2004.

[71] V. Burkhardt, W. Roth, H. Tibbenham, and J. Wuenning, “Annealing and pickling lines : benefits from advanced combustion systems The performance of combustion equipment is a major issue in modern stainless steel strip annealing and pickling lines , not only for energy saving and abatement of nitric oxide emiss.”

[72] “Burner | NFK Holdings Co.,Ltd.” http://www.nfk-hd.co.jp/english/business/furnace/burner.html (accessed Sep. 21, 2021).

[73] J. G. Wünning, “Flox®—flameless combustion,” 2003.

[74] I. Nakamachi, “Development of FDI Low NO_X Combustion Technique,” *Ind. Heat.*, vol. 27, pp. 11–19, 1990.

[75] R. Weber, J. P. Smart, and W. vd Kamp, “On the (MILD) combustion of gaseous, liquid, and solid fuels in high temperature preheated air,” *Proc. Combust. Inst.*, vol. 30,

no. 2, pp. 2623–2629, 2005.

[76] F. J. Weinberg, “Combusllon ’emperatores: ’he FOIure?,” vol. 233, no. 0, pp. 239–241, 1971.

[77] H. Tsuji, A. K. Gupta, T. Hasegawa, M. Katsuki, K. Kishimoto, and M. Morita, *High temperature air combustion: from energy conservation to pollution reduction*. CRC press, 2002.

[78] G. M. Choi and M. Katsuki, “Advanced low NOx combustion using highly preheated air,” *Energy Convers. Manag.*, vol. 42, no. 5, pp. 639–652, 2001, doi: 10.1016/S0196-8904(00)00074-1.

[79] J. A. Wünning and J. G. Wünning, “Flameless oxidation to reduce thermal no-formation,” *Prog. Energy Combust. Sci.*, vol. 23, no. 1, pp. 81–94, 1997, doi: 10.1016/s0360-1285(97)00006-3.

[80] A. Cavaliere and M. de Joannon, “Mild combustion,” *Prog. Energy Combust. Sci.*, vol. 30, no. 4, pp. 329–366, 2004.

[81] A. Cavaliere and M. de Joannon, “Mild Combustion: Una lezione nell’atelier di un ‘nuovo’ processo di combustione,” 2005.

[82] T. Poinsot and D. Veynante, *Theoretical and numerical combustion*. RT Edwards, Inc., 2005.

[83] J. Hinze, “0., Turbulence, An Introduction to Its Mechanism and Theory.” McGraw-Hill Book Co., Inc, 1959.

[84] S. a Socolofsky and G. H. Jirka, “Mixing in Rivers: Turbulent Diffusion and Dispersion,” *Spec. Top. Mix. Transp. Process. Environ.*, pp. 52–80, 2004, [Online]. Available: https://ceprofs.civil.tamu.edu/ssocolofsky/cven489/Book/Book.htm.

[85] A. Favre, “Statistical equations of turbulent gases,” *Probl. Hydrodyn. Contin. Mech.*, pp. 231–266, 1969.

[86] J. Boussinesq, *Essai sur la théorie des eaux courantes*. Impr. nationale, 1877.

[87] D. C. Wilcox, *Turbulence modeling for CFD*, vol. 2. DCW industries La Canada, CA, 1998.

[88] A. Fluent, “Ansys fluent theory guide,” *ANSYS Inc., USA*, vol. 15317, pp. 724–746, 2011.

[89] T.-H. Shih, W. W. Liou, A. Shabbir, Z. Yang, and J. Zhu, “A new k-epsilon eddy viscosity model for high Reynolds number turbulent flows: Model development and validation,” 1994.

[90] V. Yakhot and S. A. Orszag, “Renormalization group analysis of turbulence. I. Basic

theory," *J. Sci. Comput.*, vol. 1, no. 1, pp. 3–51, 1986, doi: 10.1007/BF01061452.

[91] S. B. Pope, "Turbulent flows." IOP Publishing, 2001.

[92] F. R. Menter, "Two-equation eddy-viscosity turbulence models for engineering applications," *AIAA J.*, vol. 32, no. 8, pp. 1598–1605, 1994.

[93] W. P. Jones, "Turbulence modelling and numerical solution methods for variable density and combusting flows," *Turbul. React. flows*, no. 309–347, 1994.

[94] H. A. Wouters, "Lagrangian models for turbulent reacting flows.," 1999.

[95] D. Roekaerts, "Reacting Flows and Probability Density," *Clos. Strateg. Turbul. Transitional Flows*, p. 328, 2002.

[96] K. Hanjalić and B. E. Launder, "A Reynolds stress model of turbulence and its application to thin shear flows," *J. Fluid Mech.*, vol. 52, no. 4, pp. 609–638, 1972.

[97] G. Li, B. Naud, and D. Roekaerts, "Numerical investigation of a bluff-body stabilised nonpremixed flame with differential Reynolds-stress models," *Flow, Turbul. Combust.*, vol. 70, no. 1, pp. 211–240, 2003.

[98] B. E. Launder and N. D. Sandham, *Closure strategies for turbulent and transitional flows*. Cambridge University Press, 2002.

[99] S. L. Yang, B. D. Peschke, and K. Hanjalic, "Second-moment closure model for IC engine flow simulation using KIVA code," *J. Eng. Gas Turbines Power*, vol. 122, no. 2, pp. 355–363, 2000.

[100] R. Borghi and M. Champion, *Modélisation et théorie des flammes*. Editions Technip, 2000.

[101] S. P. Burke and T. E. W. Schumann, "Diffusion flames," *Ind. Eng. Chem.*, vol. 20, no. 10, pp. 998–1004, 1928.

[102] R. W. Bilger, "The Structure of Diffusion Flames," *Combust. Sci. Technol.*, vol. 13, no. 1–6, pp. 155–170, 1976, doi: 10.1080/00102207608946733.

[103] F. A. Williams, "Combustion Theory 2nd ed.,(1985), 434." Addison-Wesley Publishing Company.

[104] E. Effelsberg and N. Peters, "Scalar dissipation rates in turbulent jets and jet diffusion flames," in *Symposium (International) on Combustion*, 1989, vol. 22, no. 1, pp. 693–700.

[105] N. Peters, "Laminar diffusion flamelet models in non-premixed turbulent combustion," *Prog. energy Combust. Sci.*, vol. 10, no. 3, pp. 319–339, 1984.

[106] D. B. Spalding, "Mixing and chemical reaction in steady confined turbulent flames," in *Symposium (International) on combustion*, 1971, vol. 13, no. 1, pp. 649–657.

[107] I. S. Ertesvåg and B. F. Magnussen, “The eddy dissipation turbulence energy cascade model,” *Combust. Sci. Technol.*, vol. 159, no. 1, pp. 213–235, 2000.

[108] B. E. Sharma and L. and B.I., “APPLICATION OF THE ENERGY-DISSIPATION MODEL OF TURBULENCE TO THE CALCULATION OF FLOW NEAR A SPINNING DISC,” 信阳师范学院, vol. 10, no. 2, pp. 1–15, 1974.

[109] B. Magnussen, “On the structure of turbulence and a generalized eddy dissipation concept for chemical reaction in turbulent flow,” in *19th aerospace sciences meeting*, 1981, p. 42.

[110] B. F. Magnussen, “Modelling of NOx and Soot formation by the Eddy Dissipation Concept,” *International flame research foundation first topic oriented technical meeting*. pp. 1–20, 1989.

[111] B. F. Magnussen and B. H. Hjertager, “On mathematical modeling of turbulent combustion with special emphasis on soot formation and combustion,” *Symp. Combust.*, vol. 16, no. 1, pp. 719–729, 1977, doi: 10.1016/S0082-0784(77)80366-4.

[112] P. Cheng, “Two-dimensional radiating gas flow by a moment method,” *AIAA J.*, vol. 2, no. 9, pp. 1662–1664, 1964.

[113] S. R. Turns, *Introduction to combustion*, vol. 287. McGraw-Hill Companies, 1996.

[114] S. R. Shabanian, M. Derudi, M. Rahimi, A. Frassoldati, A. Cuoci, and T. Faravelli, “Experimental and numerical analysis of syngas MILD combustion,” *Conf. Poster*, vol. 3400, no. 2007, pp. 1–7, 2011, doi: 10.1007/s10494-011-9337-0.

[115] F. Wang, P. Li, J. Mi, J. Wang, and M. Xu, “Chemical kinetic effect of hydrogen addition on ethylene jet flames in a hot and diluted coflow,” *Int. J. Hydrogen Energy*, vol. 40, no. 46, pp. 16634–16648, 2015, doi: 10.1016/j.ijhydene.2015.09.047.

[116] S. Boussetla, A. Mameri, and A. Hadef, “NO emission from non-premixed MILD combustion of biogas-syngas mixtures in opposed jet configuration,” *Int. J. Hydrogen Energy*, no. xxxx, pp. 1–15, 2021, doi: 10.1016/j.ijhydene.2021.01.074.

[117] T. Takeno and M. Nishioka, “Species conservation and emission indices for flames described by similarity solutions,” *Combust. Flame*, vol. 92, no. 4, pp. 465–468, 1993, doi: 10.1016/0010-2180(93)90157-X.

[118] E. Mastorakos, A. M. K. P. Taylor, and J. H. Whitelaw, “Extinction and temperature characteristics of turbulent counterflow diffusion flames with partial premixing,” *Combust. Flame*, vol. 91, no. 1, pp. 40–54, 1992, doi: 10.1016/0010-2180(92)90125-9.

[119] E. Mastorakos, A. M. K. P. Taylor, and J. H. Whitelaw, “Scalar dissipation rate at the

extinction of turbulent counterflow nonpremixed flames," *Combust. Flame*, vol. 91, no. 1, pp. 55–64, 1992, doi: 10.1016/0010-2180(92)90126-A.

[120] F. A. Williams, *Proceedings of the Project SQUID WORKSHOP ON TURBULENT MIXING IN NONREACTIVE AND REACTIVE FLOWS*, vol. 148. .

[121] B. E. Launder, G. J. Reece, and W. Rodi, "Progress in the development of a Reynolds-stress turbulence closure," *J. Fluid Mech.*, vol. 68, no. 3, pp. 537–566, 1975.

[122] B. E. Launder, "Second-moment closure: present… and future?," *Int. J. Heat fluid flow*, vol. 10, no. 4, pp. 282–300, 1989.

[123] F. R. Menter, M. Kuntz, and R. Langtry, "Ten years of industrial experience with the SST turbulence model," *Turbul. heat mass Transf.*, vol. 4, no. 1, pp. 625–632, 2003.

[124] A. R. Masri, B. B. Dally, R. S. Barlow, and C. D. Carter, "The structure of the recirculation zone of a bluff-body combustor," *Symp. Combust.*, vol. 25, no. 1, pp. 1301–1308, 1994, doi: 10.1016/S0082-0784(06)80771-X.

[125] A. R. Masri and R. W. Bilger, "Turbulent diffusion flames of hydrocarbon fuels stabilized on a bluff body," *Symp. Combust.*, vol. 20, no. 1, pp. 319–326, 1985, doi: 10.1016/S0082-0784(85)80517-8.

[126] K. Xiao, D. Schmidt, and U. Maas, "PDF simulation of turbulent non-premixed CH4/H2-air flames using automatically reduced chemical kinetics," *Symp. Combust.*, vol. 27, no. 1, pp. 1073–1080, 1998, doi: 10.1016/S0082-0784(98)80508-0.

[127] M. Hossain, J. C. Jones, and W. Malalasekera, "Modelling of a bluff-body nonpremixed flame using a coupled radiation/flamelet combustion model," *Flow, Turbul. Combust.*, vol. 67, no. 3, pp. 217–234, 2001, doi: 10.1023/A:1015014823282.

[128] B. B. Dally, D. F. Fletcher, and A. R. Masri, "Computations of a non-reacting bluff body jet flow," in *Proceedings of the First Asian Computational Fluid Dynamics Conference*, 1995, pp. 177–182.

[129] A. Frassoldati, P. Sharma, A. Cuoci, T. Faravelli, and E. Ranzi, "Kinetic and fluid dynamics modeling of methane/hydrogen jet flames in diluted coflow," *Appl. Therm. Eng.*, vol. 30, no. 4, pp. 376–383, 2010, doi: 10.1016/j.applthermaleng.2009.10.001.

[130] D. B. Spalding, "Development of the eddy-break-up model of turbulent combustion," in *Symposium (International) on Combustion*, 1977, vol. 16, no. 1, pp. 1657–1663.

[131] C. Galletti, A. Parente, M. Derudi, R. Rota, and L. Tognotti, "Numerical and experimental analysis of NO emissions from a lab-scale burner fed with hydrogen-enriched fuels and operating in MILD combustion," *Int. J. Hydrogen Energy*, vol. 34, no. 19, pp. 8339–8351, 2009.

[132] C. Galletti, A. Parente, and L. Tognotti, “Numerical and experimental investigation of a mild combustion burner,” *Combust. Flame*, vol. 151, no. 4, pp. 649–664, 2007.

[133] A. Parente, M. R. Malik, F. Contino, A. Cuoci, and B. B. Dally, “Extension of the Eddy Dissipation Concept for turbulence/chemistry interactions to MILD combustion,” *Fuel*, vol. 163, pp. 98–111, 2016.

[134] A. Parente, M. R. Malik, F. Contino, A. Cuoci, and B. B. Dally, “Extension of the Eddy Dissipation Concept for turbulence/chemistry interactions to MILD combustion,” *Fuel*, vol. 163, pp. 98–111, 2016, doi: 10.1016/j.fuel.2015.09.020.

[135] J. F. Kaiser, “On a simple algorithm to calculate the’energy’of a signal,” in *International conference on acoustics, speech, and signal processing*, 1990, pp. 381–384.

[136] F. Wang, J. Mi, P. Li, and C. Zheng, “Diffusion flame of a CH4/H2 jet in hot low-oxygen coflow,” *Int. J. Hydrogen Energy*, vol. 36, no. 15, pp. 9267–9277, 2011, doi: 10.1016/j.ijhydene.2011.04.180.

[137] A. Mardani, S. Tabejamaat, and M. Ghamari, “Numerical study of influence of molecular diffusion in the Mild combustion regime,” *Combust. Theory Model.*, vol. 14, no. 5, pp. 747–774, 2010, doi: 10.1080/13647830.2010.512959.

[138] M. T. Lewandowski and I. S. Ertesvåg, “Analysis of the Eddy Dissipation Concept formulation for MILD combustion modelling,” *Fuel*, vol. 224, no. April 2017, pp. 687–700, 2018, doi: 10.1016/j.fuel.2018.03.110.

[139] M. T. Lewandowski, A. Parente, and J. Pozorski, “Generalised Eddy Dissipation Concept for MILD combustion regime at low local Reynolds and Damköhler numbers. Part 1: Model framework development,” *Fuel*, vol. 278, no. July 2019, p. 117743, 2020, doi: 10.1016/j.fuel.2020.117743.

[140] M. T. Lewandowski, Z. Li, A. Parente, and J. Pozorski, “Generalised Eddy Dissipation Concept for MILD combustion regime at low local Reynolds and Damköhler numbers. Part 2: Validation of the model,” *Fuel*, vol. 278, no. February, 2020, doi: 10.1016/j.fuel.2020.117773.

[141] G. P. Smith, “GRI-Mech 3.0,” *http//www. me. berkley. edu/gri_mech/*, 1999.

[142] C. T. Bowman *et al.*, “GRI-Mech 2.11, 1995,” *URL http//www. me. berkeley. edu/gri_mech*, 1995.

[143] A. Kazakov and M. Frenklach, “Reduced reaction sets based on GRI-Mech 1.2,” *Univ. Calif. Berkeley, Berkeley, CA, http//www. me. berkeley. edu/drm*, 1994.

[144] J. Zhang, J. Mi, P. Li, F. Wang, and B. B. Dally, “Moderate or intense low-oxygen

dilution combustion of methane diluted by CO2 and N2," *Energy and Fuels*, vol. 29, no. 7, pp. 4576–4585, 2015, doi: 10.1021/acs.energyfuels.5b00511.

[145] F. Wang, P. Li, J. Zhang, Z. Mei, J. Mi, and J. Wang, "Routes of formation and destruction of nitrogen oxides in CH4/H2 jet flames in a hot coflow," *Int. J. Hydrogen Energy*, vol. 40, no. 18, pp. 6228–6242, 2015, doi: 10.1016/j.ijhydene.2015.03.047.

[146] S. H. Kim, K. Y. Huh, and B. Dally, "Conditional moment closure modeling of turbulent nonpremixed combustion in diluted hot coflow," *Proc. Combust. Inst.*, vol. 30, no. 1, pp. 751–757, 2005.

[147] A. Frassoldati, P. Sharma, A. Cuoci, T. Faravelli, and E. Ranzi, "Kinetic and fluid dynamics modeling of methane/hydrogen jet flames in diluted coflow," *Appl. Therm. Eng.*, vol. 30, no. 4, pp. 376–383, 2010.

[148] C. Dai, Z. Shu, P. Li, and J. Mi, "Combustion Characteristics of a Methane Jet Flame in Hot Oxidant Coflow Diluted by H2O versus the Case by N2," *Energy and Fuels*, vol. 32, no. 1, pp. 875–888, 2018, doi: 10.1021/acs.energyfuels.7b03060.

[149] J. Aminian, C. Galletti, S. Shahhosseini, and L. Tognotti, "Numerical investigation of a MILD combustion burner: Analysis of mixing field, chemical kinetics and turbulence-chemistry interaction," *Flow, Turbul. Combust.*, vol. 88, no. 4, pp. 597–623, 2012, doi: 10.1007/s10494-012-9386-z.

[150] R. L. Gordon, A. R. Masri, and E. Mastorakos, "Heat release rate as represented by [OH] × [CH2O] and its role in autoignition," *Combust. Theory Model.*, vol. 13, no. 4, pp. 645–670, 2009, doi: 10.1080/13647830902957200.

[151] X. Gao, F. Duan, S. C. Lim, and M. S. Yip, "NOx formation in hydrogen-methane turbulent diffusion flame under the moderate or intense low-oxygen dilution conditions," *Energy*, vol. 59, pp. 559–569, 2013, doi: 10.1016/j.energy.2013.07.022.

[152] X. Jiang *et al.*, "Detailed investigation of NO mechanism in non-premixed oxy-fuel jet flames with CH4/H2 fuel blends," *Int. J. Hydrogen Energy*, vol. 43, no. 17, pp. 8534–8557, 2018, doi: 10.1016/j.ijhydene.2018.03.100.

ABSTRACT

Moderate or Intense Low–oxygen Diluted (MILD) combustion is a promising technology with important properties such as zero-emission and high efficiency. The biogas-syngas mixture is also considered as a promising new renewable biofuel with low emissions. The objective of this work is to examine the effects of several parameters on the flame structure and emissions of biogas-syngas fuel under MILD conditions in JHC (Jet in Hot Co flow) burner. The modified standard k-ε model is adopted for turbulence modeling and the Eddy Dissipation Concept (EDC) model is used with three detailed reaction mechanisms, namely: GRI-Mech 3.0, GRI-Mech 2.11, and DRM 2.11. Effects of biogas-syngas composition, temperature, and oxygen concentration in the hot coflow and Reynolds number of the fuel jet have been elucidated. Results show that flame structure is more sensitive to the increase of hydrogen in syngas than that of methane in biogas. An increase of temperature and oxygen concentration in the coflow stream leads to more NO formation whereas Reynolds number augmentation reduced them. Furthermore, NO species production is globally governed by NNH route.

الملخص

يعد الاحتراق المخفف بالأكسجين المنخفض (المعتدل أو المكثف) تقنية واعدة بخصائص مهمة مثل الانبعاث الصفري والكفاءة العالية. يعتبر خليط الغاز الحيوي والغاز التخليقي أيضًا وقودًا حيويًا متجددًا جديدًا واعدًا مع انبعاثات منخفضة. الهدف من هذا العمل هو فحص تأثيرات العديد من المعلمات على هيكل اللهب وانبعاثات وقود الغاز الحيوي في ظل ظروف MILDفي موقد JHC (تدفق الغاز الساخن). تم اعتماد نموذج k-ε القياسي المعدل لنمذجة الاضطراب ويستخدم نموذج Eddy Dissipation Concept (EDC)مع ثلاث آليات تفاعل مفصلة، وهي GRI-Mech 3.0 :و GRI-Mech 2.11و .DRM 2.11 تم توضيح تأثيرات تكوين الغاز الحيوي، ودرجة الحرارة وتركيز الأكسجين الهواء الساخن وعدد رينولدز في التدفق الخارجي لغرفة الاحتراق. أظهرت النتائج أن هيكل اللهب أكثر حساسية لزيادة الهيدروجين في الغاز التخليقي من الميثان في الغاز الحيوي. تؤدي زيادة درجة الحرارة وتركيز الأكسجين في تيار التدفق المشترك إلى المزيد من تكوين أكسيد النيتروجين بينما تؤدي زيادة عدد رينولدز إلى تقليلها. علاوة على ذلك، يخضع إنتاج NO لمسار.NNH